Self-Assembly in Mechanical Systems

James Kwiecinski
St Catherine's College
University of Oxford

A thesis submitted for the degree of
Doctor of Philosophy

Trinity 2018

For everyone who has been with me on my journey thus far,
and for those who had to leave a little early.

Acknowledgements

Despite what anyone else might tell you, undertaking a DPhil is not an easy feat. They say that it takes a village to raise a child and, luckily for me, I had many people who provided incredible support. For that, they deserve recognition, and what better place to highlight their contributions than here? The following special mentions come in some approximately chronological order, except for the last paragraph.

If I were to pin-point where my taste for research began, it would definitely be in high-school. There, I had the opportunity to participate in the CSIRO Student Research Scheme, thanks in no small part to my chemistry teacher at the time, Alexandra "Mum" Abela, and physics teacher, Rob Chapman, who nominated me for the program. It was there that I caught the research "bug". Who would have thought that it would further metastasize almost a decade later? Whilst the bug is terminal, it fortunately doesn't seem to be too deadly. Special thanks also goes to another science teacher I was lucky enough to have, Rodney "Dad" Clarke, who almost fell asleep when I was describing my DPhil research to him. Granted, he was jetlagged after making the trek to visit me from Australia, so I forgive him this time around. Thank you again for visiting whilst I was at Oxford.

My later studies at Monash University opened my eyes to the world of research that was out there. Whilst I originally intended to pursue physics (sorry Ms. Abela!), I somehow wound up with a double major in applied mathematics after my 2nd year (sorry Mr. Chapman!). To this day, I'm still unsure of how this happened; it's much like finding a $5 note in a pair of jeans and having no idea how it arrived there. Though if I were to guess, it would probably have something to do with the guidance of Michael Page. It was thanks to him that I had the opportunity to engage in research over two summers and who lit the flame in me to pursue applied mathematics further. I would also like to thank David Paganin

who was perhaps the most inspirational lecturer I ever had; he became an invaluable mentor who encouraged me to shoot for greater heights. I still try to emulate his manner of teaching whenever I'm in a lecture theater and I hope that I can be as good a mentor to a student as he was to me.

After my undergraduate studies, I was keen to pursue a PhD and, to this end, I am grateful to have been financially supported by the General Sir John Monash Foundation. Being a scholar of the foundation, I've had the opportunity to meet some incredible people, one of whom is the former CEO of the foundation Peter Binks. He is one of the most down-to-earth people I have ever met and I will never forget the power of his encouragement. Even reading an email from him gives one the motivation to take on the world! I keep a copy of one in my wallet if ever I need a pick-me-up.

During my studies at Oxford, I met some world-class researchers. Much of the way I approach research can be attributed to them and, for that, I'm thankful to have had the opportunity to collaborate with them. These people include Robert Van Gorder, who gave me many aesthetic research ideas - it is thanks to him that I am now a practiced writer of academic papers - and Jon Chapman who showed me the incredible power of asymptotic analysis in finding insight into difficult mathematical problems. I'm still not completely convinced that asymptotics isn't some form of black magic because it often works better than it has any right to. Lastly, I'd like to thank my DPhil supervisor Alain Goriely and his PA Nicola Kirkham. Nicola was instrumental in keeping my sanity and also convinced me that I still had my sense of humor even during my PhD whilst Alain was a good role model for someone who stands confidently on the border between both mathematics and science; the bonafide applied mathematician. He autographed a copy of his book for me where he wrote: "To James K. A great student who always teaches me more maths". I am not completely sure about the validity of that statement, but I hope he realizes that our relationship has gone both ways during my time as a PhD student.

Whilst the PhD was arguably the most academically challenging undertaking I've accomplished, it was also one of the most spiritually trying. To this end, I am grateful for the guidance and care shown by Sister Mary Phillipa and the Bernadine Cistercians at Brownshill Monastery

who helped me to rediscover the joys of God in everything: my life, the world around me, my work, and, dare I say, this dissertation. I also met other spiritual people who made a deep impression on me, most notably Noel Lobo, Sarah Gardner-Lobo, and Maryse L'Hoste. Noel and Sarah, the former a mathematician, and the latter an agricultural scientist working on complexity theory, called me up one day with a very unusual request: "Would you like to go on a religious pilgrimage?" A week later, I found myself in Walsingham, where Our Lady appeared, with Noel. I'm still not sure how that happened, though I will always fondly remember our discussions on mathematics as we hiked up "Pilgrim's Way" saying the rosary and I will never forget Sarah's delicious cooking. I hope in the future we can all collaborate on work *ad maiorem Dei gloriam*. I am also grateful to Maryse, my adopting Cheltenian "granny", who was kind enough to let me stay with her over Easter 2018 and who visited me in Oxford; she has great taste in whiskey! Special mention should also be given to Valerie Riches and the Riches family for providing a roof over my head during the last two years of my PhD. May our blessed God help them all in their future endeavors, especially as reward for assisting me with mine!

It goes without saying that my parents played the most important part of my upbringing, apart from the obvious matter of conception. My mother always found opportunities to further my learning, in some cases even lying about my age so that I could get into advanced classes; it led to my first identity crisis at the age of 12. My father fostered my inquisitive nature to question and tinker with everything; I'm pretty sure he's taught me things that will get me into trouble one day. It is through their love and support that I developed into the researcher and man that I am today. I had a feeling they always wanted a doctor in the family; though they never stipulated that it couldn't be a doctor of philosophy. As a bonus, my work is even loosely biomedical-related.

I don't think it's an understatement to say that, without all the aforementioned people, this dissertation wouldn't exist. Whether it was helping me come to the University of Oxford in the first place, giving me encouragement when I hit another dead-end during research, or caring for my physical, mental, or spiritual well-being, they all played an important part

in making this work possible and, for that, I am truly thankful. I hope the following dissertation exceeds all your expectations.

Abstract

Inspired by biological membrane shaping in the cell through means of curvature-inducing proteins, we investigate the interplay between membrane curvature and the distribution and movement of shape-inducing objects which are free to move as a consequence of the underlying shape. We initially study the self-assembly of a filament, taken as a proxy for the cross-section of a biomembrane, which is primarily driven by the chemical kinetics of attaching proteins and find that, under certain mechanical stiffness regimes of the attaching proteins, pattern formation occurs. Regions of high and low protein concentration form before spatially uniform filament shapes are obtained by means of protein adhesion and movement governed by diffusion and local curvature-seeking. However, noting that the curvature-mediated protein movement on membranes has been biologically observed to be long-range, we next study the self-assembly of embedded inclusions on a membrane as a result of the underlying geometry. We first derive an interaction law for the shape-mediated interaction of inclusions which break symmetry and find that there is a finite equilibrium distance to which the inclusions will aggregate. We derive corresponding equations of motion which describe this curvature-mediated aggregation mechanism and, using this framework, we investigate some of the properties of these self-assembled configurations, including their energy, stability, and their collective elastic behavior. Lastly, we consider the interaction energies of embedded inclusions on a periodic domain and determine that this mechanism may explain computational results of how proteins form rings to promote tubulation on cylindrical membranes.

Contents

List of Figures

Chapter 1

Introduction

1.1 Self-assembly and cellular membrane shaping

Self-assembly is a ubiquitous phenomenon that exists over a large range of length scales in systems both physical and biological in nature. Examples range from the astronomically large, such as the formation of galaxies and planetary systems [20], to the nano-scale, such as the technology of DNA origami [77]. In its most basic definition, such self-assembling systems are: (i) comprised of parts or components that exhibit interaction; (ii) at thermodynamic nonequilibrium initially, but tend to equilibrium; (iii) thermodynamically closed [43, 81]. Self-assembly is a process of energy minimization that ends in a final, well-defined structure that is uniquely determined by the properties of the interacting components which remain unchanged during the transition to thermodynamic equilibrium. Global order in the system is encoded in the initial set-up and the specific relationships that exist between components; no additional energy is necessary to drive the process [35].

An interesting example of self-assembly is found in the shaping of biological membranes, in particular lipid bilayers, that occur at the cellular level. Such objects are important building blocks which not only coat parts of the cell, such as the nucleus and the endoplasmic reticulum [83], but also form independent biological objects within the cell, such as vesicles and tubules which are necessary for the intra-cellular transport of wastes, nutrients, and proteins [62, 93].

The primary mechanism believed to be responsible for the highly curved geometries observed involves the recruitment of membrane-shaping proteins from the cellular fluid, such as the BAR (Bin/Amphiphysin Rvs) and ENTH (Epsin N-Terminal Homology) protein families [5, 16, 74, 108]. Such proteins bind directly onto the bilayer by means of electrostatic interactions and bend it by the insertion of amphipathic helix functional groups [33, 66], with the magnitude of the induced curvature

dependent on the depth of insertion into the lipid monolayer [44] and the number of attaching proteins [90]. Moreover, the BAR and ENTH families act as sensors of curvature [12, 72], meaning that the shape of the membrane determines the adhesion kinetics of the proteins and, once embedded, their motion within the lipid bilayer. In other words, we have a system where the curvature of the membrane regulates the distribution of attached proteins, and vice-versa, in an interacting process [84].

1.2 Previous work

1.2.1 Chemically driven self-assembling membranes

Previous investigations on protein adhesion dominated membrane remodeling have been from two perspectives; namely, computational, involving large-scale coarse-grain simulations [4, 6, 65], and theoretical, which consider the minimization of membrane free energies or electrical potentials to determine the nature of equilibrium configurations. In the former, many interesting aspects of BAR proteins have been found, including the linear aggregation of proteins, leading to membrane tubulation [86, 103], and membrane fissioning, leading to closed tubular networks [85]. From a theoretical point of view, the effects of single BAR proteins, in the context of electric fields and potentials [51], and a continuum of them attaching to the lipid bilayer have also been studied, but not to the same extent as computational models. In particular, equilibrium configurations of the self-assembled system, and the role that BAR proteins play in the stability of these final shapes, are considered. Early research on the subject studied not the formation of vesicles or other independent biological objects, but rather the oscillations that can exist on the cell-membrane known as *circular dorsal ruffles* [50, 71]. It is found that BAR proteins provide a stabilization of the geometry; a point which has been further investigated in the context of flat membrane geometries [82] and pearling instabilities in cylindrical geometries [48].

1.2.2 Global membrane-mediated interactions

Recent work has found that proteins of a particular mechanical stiffness will be recruited from the surrounding fluid to form patterns of high and low concentrations on simplified membrane geometries in order to reach a final equilibrium shape [57]. However, experimental and computational work has suggested that long-range interactions between proteins which are already attached to the membrane result in self-assembled aggregation and this phenomenon also plays a significant role in membrane-shaping

[85, 86, 88, 87, 96, 84, 10]. The nature of interactions between proteins varies from the direct and short range, whereby van Der Waals forces and hydrogen bonds dominate, to more indirect global interactions which are mediated by the underlying membrane shape [49]. The membrane-mediated interactions can be further split into forces arising from surface tension, Casimir-like thermal effects from perturbations in degrees of freedom of the membrane, such as thickness, and curvature. The present work considers this lattermost effect.

There has been substantial theoretical work describing the global interactions between inclusions embedded in a fluid membrane. In particular, it was found that perfectly circular inclusions which impose a constant opening angle will repel according to the inverse separation to the fourth power due to effects from membrane bending [41, 31]. Further work has since extended the effects of the curvature imposed by these isotropic inclusions to include spontaneous membrane mean curvature [18, 3], lateral membrane tension [101], and slightly non-circular but symmetrical geometries [30] which exhibit attraction depending on the inverse quartic of the separation depending on the inclusion orientation. Higher order expansions of these curvature interactions have been calculated [32], and effective field theories developed [104, 105, 56].

Thermal Casimir-like forces have been suggested as a mechanism for proteins to aggregate, given that attraction does occur for isotropic inclusions [76, 21] and rod-like geometries [40, 39] on the inverse quartic of separation with similar extensions to include membrane tension [61] and with mean field theories developed [27]. However, it is not clear whether this attraction is stronger than the curvature-mediated repulsion [79] that has been theoretically found. It was recently posited that this disagreement between the aggregation seen in experiment and large-scale simulation and the repulsion predicted in theory could be explained by means of inclusions having unique mechanical signatures when they are embedded in the membrane [1].

The study of inclusions which interact anisotropically with the surrounding membrane could provide explanations as to why aggregation occurs. Previous work has shown that such anisotropic inclusions will interact and aggregate [28, 29] and recent work [69] has shown that rods will interact on the inverse separation squared when the rod imposes non-zero curvature along its orientation, a similar result that was previously shown in [70] when up-down symmetry was broken between the rod inclusions.

1.2.3 Self-assembling aggregates

In recent work which minimized the energy of a fluid membrane [45] due purely to bending energies [58], an interaction law was found between rigid symmetry-breaking inclusions which predicted that curvature-mediated aggregation was possible. Inclusions would attract along a certain orientation and would do so until the effects of attraction were balanced by the repulsion from isotropic deformations, leading to a natural equilibrium distance. Furthermore, it was shown that an individual inclusion created a curvature-mediated interaction field similar to quadrupoles seen in electrostatics and magnetism [47]. A number of questions arise from these results: What aggregate shapes does the interaction law derived predict and what is their associated stability and macroscopic properties? If the inclusions are free to move, are there other configurations they may self-assemble into? The current work investigates these questions more fully.

There exist similar systems to the curvature-mediated interaction of membrane inclusions on a lipid bilayer, such as the long-range capillarity interactions between particles when their induced distortions to the fluid surface overlap [8]. For "monopole" particles which induce isotropic deformations, both attraction and repulsion is possible, depending on whether the contact angle of both inclusions have the same sign or are opposite respectively [97]. However, there are many objects which deform the fluid interface forming capillarity quadrupoles, such as rods [13], ellipsoids non-magnetized [64], and magnetic so that their anisotropic deformation can be tuned [19], and cylinders [60]. The far-field interaction of two ellipsoids on a fluid surface, which form capillarity quadrupoles, have been predicted and observed to attract for mirror-symmetric configurations on the inverse separation to the fourth power [92], with capillary torque that results in the two ellipsoids attracting end-to-end on the inverse separation to the sixth power [60]. In contrast to the curvature-mediated equilibrium distance attained by membrane inclusions, capillarity quadrupoles will attract until the two particles touch. This aspect leads to a near-field interaction regime, the analysis of which has shown that ellipsoids exhibit bistable configurations either aligning end-to-end or side-to-side, with the latter theoretically shown to be the lower energy configuration [59, 63]. Despite this result, both alignment configurations have been observed [106, 8].

Another physical system that has been studied involves the interaction of neodymium-iron-boron magnetic spheres which interact as dipoles. Recent theoretical work has studied the collective elastic properties [98, 42] of self-assembled chains that the spheres form, given that, under deformations, the shape of the chains remain largely

coherent. Further investigations have studied the elastic buckling behavior of magnetic chains under the effects of gravity [80] whilst other work has considered the macroscopic properties of magnetosomes in magnetotactic bacteria [54]. The current work draws analogies to these physical systems so that further understanding can be obtained into the mechanism of curvature-mediated attraction and the corresponding properties of the self-assembled aggregates.

1.3 Organization of thesis

We structure the thesis as follows: We derive the simplest, non-trivial system that allows us to explore the interplay between an underlying geometry and curvature-sensing proteins in Chapter 2. We focus on the shaping of a filament and derive a macroscopic model for time-dependent self-assembly using concepts from continuum and statistical mechanics. The result is a thermodynamically consistent system of equations in terms of experimental parameters that allows us to further explore the role of the filament mechanics, the adhesion kinetics of the attaching proteins, and the interactions between these components. We show that the stability of the filament's shape is completely characterized by the parameters associated with protein recruitment and establish that there exists a bistable regime. In this regime, proteins aggregate on the filament forming regions of high and low curvature and this pattern formation is followed by phase-coarsening that resolves on a time-scale dependent on protein diffusion and drift across the filament, which contend to smooth and maintain the pattern respectively.

However, the filament model inadequately describes the biological phenomenon of membrane remodeling in that it does not include the effects of global interactions between embedded proteins on a lipid bilayer, seen in experimental and computational results. To this end, Chapter 3 studies the global interactions of similar anisotropic inclusions which are mediated by the bending of a fluid membrane and we consider two methods by which these inclusions break membrane symmetry. First, we consider perfectly circular inclusions which impose a membrane contact or opening angle that is periodic as one traverses the inclusion boundary. We find that the second Fourier mode or the "quadrupole" opening angle is the dominant reflection symmetry in the interaction energy. Furthermore, the quadrupole contact angle imposed by one inclusion couples with the constant contact angle imposed by the other, and this determines the extent to which curvature-mediated attraction and repulsion on the inverse separation squared occurs. Second, we study inclusions which impose a

constant contact angle around their boundary but are now perturbed from a circular geometry. We show that such a construction results in the same interaction energy, with the previous quadrupole contact angle being a product of a coupling of the geometry deviation of the inclusion together with its constant imposed contact angle. We further show that the interaction law derived gives rise to a stable equilibrium aggregation separation whereby the attraction arising from symmetry-breaking balances with the repulsion seen in the purely isotropic case.

Although there are similarities between other aggregating and self-assembling systems with the curvature-mediated interactions of anisotropic inclusions, the underlying physics governing the phenomenon are different. Therefore, one might expect that inclusions on a fluid membrane will interact and give rise to aggregates not seen in these other physical systems as a result of mechanical arguments; a point we investigate further in Chapter 4. We apply analytical and numerical techniques to study simplified aggregate configurations, such as the line and polygon, and determine their energy densities and their stability under perturbations. We find a number of unusual results which contrast the curvature-mediated interaction of inclusions to other physical systems, such as the impossibility of finite pentagon aggregates being formed, to the aggregate requiring finite energy to stretch it to infinity.

Lastly, it has been hypothesized [84] and computationally observed [89] that proteins will form rings on cylindrical geometries, which suggests that, due to the underlying membrane geometry, embedded proteins exhibit a preferred alignment. In Chapter 5, we investigate one of the mechanisms by which this alignment occurs; namely, through periodicity on the membrane domain. We first determine the interaction energy between two symmetry-breaking inclusions on an approximately flat fluid membrane which stretches to infinity in one direction, but is periodic in the other orthogonal direction. By asymptotic matching, we find that periodicity results in the inclusion aligning itself parallel to the periodic boundary in order to be in an attracting configuration with its own images. We generalize this curvature-mediated result to consider the interaction of an arbitrary number of inclusions and derive equations of motion which are numerically solved. We observe from the simulation that the inclusions form aggregates analogous to rings, suggesting that periodicity is a viable mechanism to explain the results reported in the literature.

We conclude in Chapter 6 by summarizing the results presented in the current work and provide future directions which warrant further investigation.

Chapter 2

Self-assembly of a filament

The results of this chapter have been published in [57].

We explore a simplified macroscopic model of membrane shaping by means of curvature-sensing BAR proteins. We proceed as follows: In Section 2.1 we derive equations describing the interplay between the shape of a freely floating filament in a fluid and the adhesion kinetics of proteins using mechanical principles. In Section 2.2, we study the constant curvature solutions that arise from this system using weakly nonlinear analysis and show that there exists a bistable regime which exhibits pattern formation in the protein concentration; a result which is also verified numerically. In Section 2.3, the filament model is generalized for multiple species of BAR proteins and we show that the stability of the assembled shape is determined by a competition between proteins attaching on opposing sides. We summarize the results of the chapter in Section 2.4 and compare the predictions of the model with experimental and computational work reported in the literature.

2.1 Mathematical Model

Our mathematical model is based on the following assumptions: (i) We consider a thermodynamically closed system in 2D space which only contains the main continuum, the curvature-inducing proteins, and the interactions between these. There is no forcing or energy input from the outside environment; (ii) We take the continuum to be a 1D filament; explicitly, an elastic rod which is inextensible and unshearable with constant length L that is parameterized with an arc-length coordinate $s \in [0, L]$. This geometry is a simplification of the 2D lipid bilayer without transverse mechanical effects and area dilation, despite the membrane being able to endure strains of 2-3% [75]. The dependent variable of interest is the filament curvature $\kappa(t, s)$ at time

t; (iii) The continuum freely floats in a fluid which is populated with a single type of BAR protein modeled as a thin filament with constant curvature. The proteins induce curvature along one principal direction which is always aligned with that of the main filament and they have a thermodynamically favorable target curvature κ_t. The number of bound proteins per unit length is given by $c(t, s)$.

Additionally, we make two important thermodynamic assumptions. (iv) We suppose that protein-membrane interactions are at thermodynamic equilibrium with respect to energy exchange between these components. A number of theoretical models have made this same assumption [48, 71] as well as computational models [91]. In the latter case, results predicted by simulations have been experimentally verified [85], which suggests that this assumption is valid when studying qualitative aspects of the mathematical model.

(v) There are three stages in the protein attachment corresponding to the unbound, transition, and bound states. An unattached protein floating in the cellular fluid is assumed to have zero bending energy (unbound state), but when the protein attaches to the main filament, it deforms itself to match the curvature of the filament and acquires bending energy dictated by bending stiffness B_{BAR} (bound state). We suppose there is an intermediary step to attachment whereby the protein acquires bending energy determined by bending stiffness B_{ts}, which is not necessarily the same as B_{BAR}, and we assume that this transition state is sufficiently long-lived such that thermodynamic equilibrium is reached.

We now derive equations describing the time-evolution of $\kappa(t, s)$ and $c(t, s)$.

2.1.1 Equations for Filamentary Mechanics

We model the membrane cross-section as a Kirchhoff elastic filament whose motion is confined to a plane. The position of the filament's centerline is denoted by $\mathbf{r}(t, s)$ and the curve is geometrically described by a local director basis $\{\mathbf{d}_1, \mathbf{d}_2, \mathbf{d}_3\}$ which is right-handed and orthonormal. The vectors $\mathbf{d}_3$ and $\mathbf{d}_1$ are the tangent and normal Frenet vectors respectively, whilst $\mathbf{d}_2$ points perpendicularly outwards from the plane and is constant with respect to both t and s (see Fig. 2.1). To complete the geometric description, we introduce a strain vector $\mathbf{u} = \kappa\mathbf{d_2}$ and spin vector $\mathbf{w} = w_2\mathbf{d}_2$, with w_2 being a measure of the angular velocity of the director basis, so that we have the

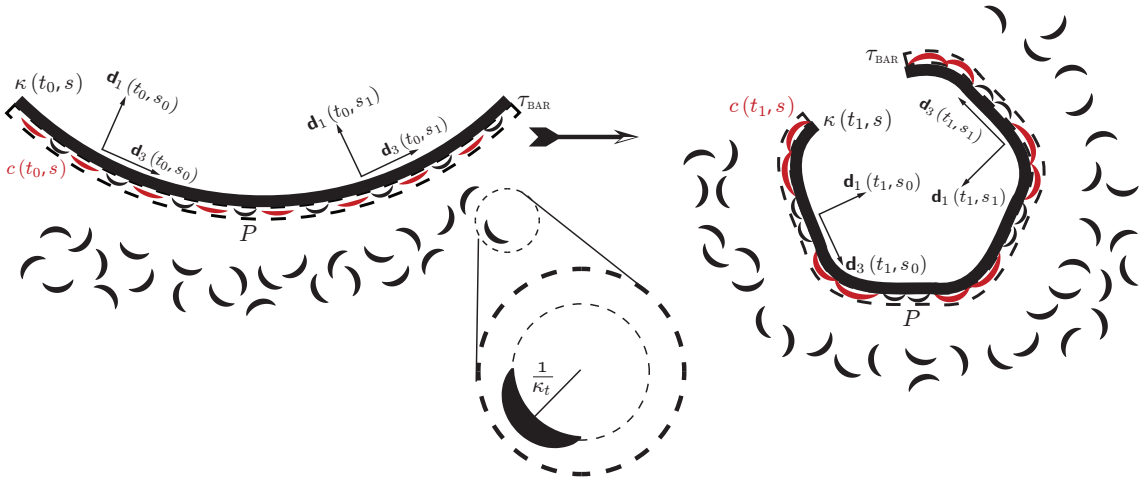

Figure 2.1: The mathematical model of 1D self-assembly as it evolves from $t = t_0$ to $t = t_1$. A filament of curvature $\kappa(t,s)$, that is described by local normal and tangential vectors $\mathbf{d}_1(t,s)$ and $\mathbf{d}_3(t,s)$, is submersed in a fluid populated with a single type of BAR protein which has constant intrinsic curvature κ_t. Unbound proteins in the layer of thickness τ_{BAR} around the filament (shown as black) have constant concentration P, and can attach onto the filament resulting in a number per unit length $c(t,s)$ (shown as red). The attached proteins give the filament an intrinsic shape that evolves in time due to thermodynamic constraints on the protein adhesion kinetics.

following kinematic relations [2]:

$$\frac{\partial \mathbf{r}}{\partial s} = \mathbf{d}_3, \tag{2.1}$$

$$\frac{\partial \mathbf{d}_i}{\partial s} = \mathbf{u} \times \mathbf{d}_i, \tag{2.2}$$

$$\frac{\partial \mathbf{d}_i}{\partial t} = \mathbf{w} \times \mathbf{d}_i. \tag{2.3}$$

Defining the velocity of the rod in the local basis $\mathbf{v} = v_1\mathbf{d}_1 + v_3\mathbf{d}_3 = \partial\mathbf{r}/\partial t$, we use (2.1)-(2.3) to obtain geometric constraints for v_1 and v_3:

$$0 = \frac{\partial v_1}{\partial s} + \kappa v_3 - w_2, \tag{2.4}$$

$$0 = \frac{\partial v_3}{\partial s} - \kappa v_1, \tag{2.5}$$

as well as a compatibility relation, given that $\partial^2\mathbf{d}_i/\partial s\partial t = \partial^2\mathbf{d}_i/\partial t\partial s$:

$$\frac{\partial \kappa}{\partial t} = \frac{\partial w_2}{\partial s}. \tag{2.6}$$

Considering the mechanics of the continuum, we suppose that the only contribution to the applied force comes from fluid drag, which is proportional to the

velocity of the filament $\mathbf{v}$. More specifically, the applied force per unit length is $\mathbf{f} = \mathbf{f}_1\mathbf{d}_1 + \mathbf{f}_3\mathbf{d}_3 = -\eta_1 v_1 \mathbf{d}_1 - \eta_3 v_3 \mathbf{d}_3$, where η_1 and η_3 are the drag coefficients per unit length in the normal and tangential directions. Given that we are interested in motions that occur at low Reynolds numbers, it is reasonable to assume that the inertial terms can be neglected so that the resulting dynamics are first order in time [38]. Furthermore, we use slender body theory to simplify the applied force so that $\eta_1 = 2\eta_3$, where $\eta_3 = 2\pi\mu/A \ln(L/r)$ for a filament of length L, cross-sectional area A, and radius $r \ll L$ which is submersed in a fluid of dynamic viscosity μ [53]. Introducing the resultant force $\mathbf{n} = n_1\mathbf{d}_1 + n_3\mathbf{d}_3$ and moment $\mathbf{m}$, we balance linear and angular momenta to obtain two equations of motion [68]:

$$\frac{\partial \mathbf{n}}{\partial s} + \mathbf{f} = \rho A \frac{\partial^2 \mathbf{r}}{\partial t^2}, \tag{2.7}$$

$$\frac{\partial \mathbf{m}}{\partial s} + \mathbf{d}_3 \times \mathbf{n} = \rho I \left(\mathbf{d}_1 \times \frac{\partial^2 \mathbf{d}_1}{\partial t^2} \right), \tag{2.8}$$

for a filament of constant density ρ and second moment of area I.

Lastly, to relate mechanical stresses to strains, we use a linear constitutive relation of the form:

$$\mathbf{m} = EI\left(\kappa - \gamma c\right)\mathbf{d}_2, \tag{2.9}$$

where E is the Young's modulus of the rod, the number of proteins per unit length c takes on a role that is analogous to the intrinsic curvature, and $\gamma > 0$ is a dimensionless measure of the curvature the proteins induce. The latter is included to account for the observation that the locally induced curvature is proportional to the number of proteins that have attached to the site [90] as well as the depth of amphipathic helix insertion [44].

Relation (2.9) is derived from an elastic energy which is quadratic in the curvature of the filament, however it has the same form as the Helfrich energy of a lipid bilayer reduced to a 1D geometry [45]. Furthermore, using (2.9) incurs an error $O(\omega^2)$ where [14]:

$$\omega = \max_{s\in[0,L]} \left\{ \left|\kappa(t,s)\right| r, \left|c(t,s)\right| r, r/L \right\}. \tag{2.10}$$

Combining (2.1)-(2.3) with (2.7)-(2.9) and the aforementioned simplifications, we include (2.4)-(2.6) so that we have the following system of 6 equations for 6 dependent

variables $\{v_1, v_3, w_2, \kappa, n_1, n_3\}$:

$$\rho A \frac{\partial v_1}{\partial t} = \frac{\partial n_1}{\partial s} + \kappa n_3 - \rho A w_2 v_3 - \eta_1 v_1, \tag{2.11}$$

$$\rho A \frac{\partial v_3}{\partial t} = \frac{\partial n_3}{\partial s} - \kappa n_1 + \rho A w_2 v_1 - \frac{\eta_1}{2} v_3, \tag{2.12}$$

$$\rho I \frac{\partial w_2}{\partial t} = EI \frac{\partial}{\partial s}(\kappa - \gamma c) + n_1, \tag{2.13}$$

$$\frac{\partial \kappa}{\partial t} = \frac{\partial w_2}{\partial s}, \tag{2.14}$$

$$0 = \frac{\partial v_1}{\partial s} + \kappa v_3 - w_2, \tag{2.15}$$

$$0 = \frac{\partial v_3}{\partial s} - \kappa v_1. \tag{2.16}$$

To close the system, we impose free-ends boundary conditions, which implies that $\mathbf{n} = \mathbf{m} = 0$ at $s = \{0, L\}$. In terms of the dependent variables, this corresponds to $n_1 = n_3 = 0$ and $\kappa = \gamma c$ applying at both ends of the filament.

2.1.2 Equation for Protein Adhesion Kinetics

We suppose there are freely floating proteins in the cellular fluid which is taken to occupy an area much larger than that of the filament. The solution is assumed to be of sufficiently high concentration and well-mixed such that the proteins are uniformly distributed. We define a region of constant width around the filament that is one BAR protein thick τ_{BAR} and presume that proteins can attach to the filament or detach from it in this region. The number of freely floating proteins per unit area of the region is P whilst the number per unit length of proteins bound to the filament is c (see Fig. 1). We summarize the kinetics as a chemical reaction of the form:

$$P \underset{K_r(\kappa)}{\overset{K_f(\kappa)\tau_{\mathrm{BAR}}}{\rightleftharpoons}} c, \tag{2.17}$$

where $K_f(\kappa)$ and $K_r(\kappa)$ are the forward (attachment) and reverse (detachment) rates of reaction, both of which depend on the curvature of the filament.

We apply the principle of mass action to (2.17) and write the time-evolution of c as:

$$\frac{\partial c}{\partial t} = K_r(\kappa) \left[\frac{K_f(\kappa)}{K_r(\kappa)} \tau_{\mathrm{BAR}} P - c \right]. \tag{2.18}$$

If the assumptions regarding the cellular fluid hold in regards to its spatial uniformity and high concentration, and we additionally suppose that τ_{BAR} is much smaller than the length of the filament L, then changes to P will be instantly replenished

by the surrounding solution. The latter assumption is biologically feasible given that $\tau_{\mathrm{BAR}} \lesssim 2 \times 10^{-9}$m, with the upper bound corresponding to the thickness of DNA [52], and $L \approx 10^{-7}$ from discussions on tube radii [11]. As such, P is effectively constant and is treated as such in the forthcoming analysis.

To find explicit expressions for the rates of reaction, we use assumption (iv) and assign a Boltzmann factor to the ratio of reaction rates:

$$\frac{K_f(\kappa)}{K_r(\kappa)} = \exp\left(-\frac{\Delta E}{k_B T}\right), \tag{2.19}$$

where k_B is Boltzmann's constant, T is the absolute temperature in the system, and ΔE is the energy difference of the protein as it transitions from the unbound to the bound state.

Since the BAR protein is modeled as a thin filament of constant curvature, it has a microscopic bending energy given by [37]:

$$\Delta E = E_b - E_u + \frac{B_{\mathrm{BAR}} L_{\mathrm{BAR}}}{2} (\kappa - \kappa_t)^2, \tag{2.20}$$

where E_u and E_b are the free energies of the protein in the unbound and bound state respectively, B_{BAR} is the bending stiffness of the protein in the bound state, L_{BAR} is the length of the protein, and κ_t is the thermodynamically favorable target curvature that is equivalent to the intrinsic curvature of the protein.

Combining (2.19) and (2.20), we have:

$$\frac{K_f(\kappa)}{K_r(\kappa)} = K_{\mathrm{eqm}} \exp\left(-\frac{\xi L_{\mathrm{BAR}}}{2} (\kappa - \kappa_t)^2\right), \tag{2.21}$$

where $\xi = B_{\mathrm{BAR}}/k_B T > 0$ is the persistence length of the protein, being a measure of its mechanical stiffness to thermal fluctuations, and $K_{\mathrm{eqm}} = \exp\left((E_u - E_b)/k_B T\right) > 0$ is a quantity that measures the extent of the attachment reaction; that is, if $K_{\mathrm{eqm}} \gg 1$, then most of the proteins will attach onto the filament, whilst if $K_{\mathrm{eqm}} \ll 1$, very few will attach.

To determine expressions for $K_f(\kappa)$ and $K_r(\kappa)$, we use assumption (v) and introduce an intermediate state so that the kinetics of (2.17) now read:

$$P \underset{K_{\mathrm{int}}}{\overset{K_f(\kappa)\tau_{\mathrm{BAR}}}{\rightleftharpoons}} c_{\mathrm{int}} \underset{K_r(\kappa)}{\overset{K_{\mathrm{int}}}{\rightleftharpoons}} c, \tag{2.22}$$

where K_{int} is the rate of the intermediate reaction and is assumed to be independent of κ, and c_{int} is the number per unit length of proteins attached to the filament that are in the transition state.

Using (2.22), we can find $K_f(\kappa)$ by assigning a Boltzmann factor in a similar manner as before, with the energy difference now being between the unbound state and the transition state of the protein [22]:

$$K_f(\kappa) = K_{f0} K_{\text{int}} \exp\left(-\frac{\xi_{\text{ts}} L_{\text{BAR}}}{2}(\kappa - \kappa_t)^2\right), \tag{2.23}$$

where $\xi_{\text{ts}} = B_{\text{ts}}/k_B T > 0$, $K_{f0} = \exp\left((E_u - E_{\text{ts}})/k_b T\right)$, and E_{ts} is the free energy of the protein in the transition state.

By considering the energy difference between the bound and the transition state, we find $K_r(\kappa)$:

$$K_r(\kappa) = K_{r0} K_{\text{int}} \exp\left(\frac{L_{\text{BAR}}}{2}(\xi - \xi_{\text{ts}})(\kappa - \kappa_t)^2\right), \tag{2.24}$$

where $K_{r0} = \exp\left((E_b - E_{\text{ts}})/k_b T\right) > 0$ and is related to K_{eqm} and K_{f0} by $K_{\text{eqm}} = K_{f0}/K_{r0}$.

Some comments regarding (2.23) and (2.24) are necessary. We note the former predicts that the highest attachment rate occurs when the curvature of the filament κ matches the target curvature of the protein κ_t. This result is expected given that the attaching protein does not need to bend to match its curvature with that of the filament, meaning no energy cost is incurred during the attachment process. Similar reasoning holds for (2.24), provided that $\xi > \xi_{\text{ts}}$, which then implies that the detachment reaction for a filament curvature $\kappa \neq \kappa_t$ occurs at a higher rate than when $\kappa = \kappa_t$ (i.e. $K_r(\kappa) > K_r(\kappa_t)$). Proteins attaching to the filament for $\kappa \neq \kappa_t$ incur an energy cost and are thermodynamically undesirable, so they do not bind to the same extent as when $\kappa = \kappa_t$.

However, there is nothing to suggest that $\xi_{\text{ts}} > \xi$ cannot also occur. In this case, the opposite holds true; namely, if the filament curvature is $\kappa \neq \kappa_t$ then the protein will detach at a lower rate than when $\kappa = \kappa_t$. This is counter-intuitive given the previous reasoning, however this is a physically realizable system in the form of a simple toy: the Chinese finger trap. The idea of the toy is simple: it is easy to insert one's fingers into the trap, but it is difficult to pull them out using force. The reason is that when the fingers are forced out, stresses are created in the system that trap the fingers. In a similar manner, stresses that are generated by the mismatch of curvatures between the filament and the protein cause the attached protein to be trapped. In either case, this mathematical model is able to emulate both physically realizable scenarios.

Lastly, we suppose that proteins that have attached onto the filament can move in two ways: the diffusion of proteins from regions of high concentration to low concentration and the drifting of proteins which seek to minimize the quantity $(\kappa - \kappa_t)^2$ for the thermodynamic reasons outlined previously. Combining the effects of protein movement with (2.18), (2.21), and (2.24), we obtain:

$$\begin{aligned}\frac{\partial c}{\partial t} = K_{r0}K_{\text{int}}\exp\left(\frac{L_{\text{BAR}}}{2}\left(\xi - \xi_{\text{ts}}\right)\left(\kappa - \kappa_t\right)^2\right) \\ \times\left\{K_{\text{eqm}}\tau_{\text{BAR}}P\exp\left(-\frac{\xi L_{\text{BAR}}}{2}\left(\kappa - \kappa_t\right)^2\right) - c\right\} \\ + D\frac{\partial^2 c}{\partial s^2} + \chi\frac{\partial}{\partial s}\left[c\frac{\partial}{\partial s}\left(\kappa - \kappa_t\right)^2\right], \quad (2.25)\end{aligned}$$

where $D > 0$ is the diffusion constant of proteins on the filament and $\chi > 0$ is the sensitivity of an individual protein to move towards regions with low $(\kappa - \kappa_t)^2$. The drift term shares a similar form to the Nernst-Planck equation for charged particles minimizing their electric potential [107] and the Keller-Segel model for the movement of bacterial populations due to gradients in chemoattractants [95].

To close (2.25), we suppose that $\partial c/\partial s = 0$ at $s = \{0, L\}$, which corresponds to attached proteins being unable to flow off the edges of the filament as a result of diffusion. However, this flux at the boundary may still be non-zero due to the effects of protein drift.

2.1.3 1D Self-Assembly Equations

Equations (2.11)-(2.16) and (2.25) form the 1D self-assembly system. We introduce the following nondimensionalizations and rescaling to simplify: $\hat{s} = s/L$, $\hat{t} = EIt/\eta_1 L^4$, $\hat{\kappa} = \kappa L$, $\hat{c} = \gamma c L$, $\hat{n}_1 = n_1 L^2/EI$, $\hat{n}_3 = n_3 L^2/EI$, $\hat{v}_1 = v_1\eta_1 L^3/EI$, $\hat{v}_3 = v_3\eta_1 L^3/EI$, $\hat{w}_2 = w_2\eta_1 L^4/EI$, $\hat{\kappa}_t = \kappa_t L$, $\hat{P} = \gamma K_{\text{eqm}}\tau_{\text{BAR}}PL$, $\hat{\xi} = \xi L_{\text{BAR}}/L^2$, $\hat{\xi}_{\text{ts}} = \xi_{\text{ts}}L_{\text{BAR}}/L^2$, $\hat{K}_{r0} = K_{r0}K_{\text{int}}\eta_1 L^4/EI$, $\hat{D} = D\eta_1 L^2/EI$, $\hat{\chi} = \chi\eta_1/EI$, so that the

equations of interest become (upon dropping the hat symbol):

$$\alpha\frac{\partial v_1}{\partial t} = \frac{\partial n_1}{\partial s} + \kappa n_3 - \alpha w_2 v_3 - v_1, \tag{2.26}$$

$$\alpha\frac{\partial v_3}{\partial t} = \frac{\partial n_3}{\partial s} - \kappa n_1 + \alpha w_2 v_1 - \frac{v_3}{2}, \tag{2.27}$$

$$\beta\frac{\partial w_2}{\partial t} = \frac{\partial}{\partial s}(\kappa - c) + n_1, \tag{2.28}$$

$$\frac{\partial \kappa}{\partial t} = \frac{\partial w_2}{\partial s}, \tag{2.29}$$

$$0 = \frac{\partial v_1}{\partial s} + \kappa v_3 - w_2, \tag{2.30}$$

$$0 = \frac{\partial v_3}{\partial s} - \kappa v_1, \tag{2.31}$$

where $\alpha = \rho AEI/\eta_1^2 L^4 \sim r^{10}/L^4$ and $\beta = \rho EI^2/\eta_1^2 L^6 \sim r^{12}/L^6$, both of which are small given that $r \ll L$ as seen in Section 2.1, and

$$\frac{\partial c}{\partial t} = K_{r0}\exp\left(\frac{1}{2}(\xi - \xi_{\text{ts}})(\kappa - \kappa_t)^2\right)\left\{P\exp\left(-\frac{\xi}{2}(\kappa - \kappa_t)^2\right) - c\right\} + D\frac{\partial^2 c}{\partial s^2} + \chi\frac{\partial}{\partial s}\left[c\frac{\partial}{\partial s}(\kappa - \kappa_t)^2\right], \tag{2.32}$$

with boundary conditions given by $n_1 = n_3 = 0$, $\kappa = c$, and $\partial c/\partial s = 0$ at $s = \{0, 1\}$.

For the current analysis and following numerical studies, we include estimates of some of the important quantities for a typical biological system in Table 2.1. In particular, we have used estimates for curvature based on discussions in [11], which propose the radius of remodeled tubes to be of the order $10^{-8} - 10^{-7}$m, and have assumed that the length of the filament is such that the self-assembled system forms complete constant curvature solutions with little to no overlap. We estimate $\eta_1 \approx 10^{13} - 10^{14}$, taking the dynamic viscosity of fluid to be approximately that of water $\mu \approx 10^{-4}\text{m}^2\text{s}^{-1}$ and the radius of the filament $r \approx 10^{-9}$m to coincide with the thickness of a lipid bilayer. We consider the bilayer to be made of packed hydrocarbon chains and use a Young's modulus of $E \approx 10^7 - 10^8\text{Nm}^{-2}$, which provides a reasonably good estimate of the material properties of a biological membrane according to [25], and take the density of the filament to be $\rho \approx 10^3\text{kg.m}^{-3}$ to approximate the fluid nature of the bilayer. Furthermore, we estimate the protein persistence length to be $\xi \approx 10^{-12} - 10^{-8}$m, with the larger bound coinciding with that of DNA [67], and the diffusion of proteins on the filament to be $D \approx 10^{-12} - 10^{-11}\text{m}^2\text{s}^{-1}$, according to studies of membrane protein movement on lipid bilayers found in [102]. Lastly, we assume K_{r0} varies substantially based upon chemical triggers which can affect protein adhesion.

Quantity	Estimated Value
κ, κ_t, c, P	$1 - 10$
ξ, ξ_{ts}	$10^{-3} - 10$
K_{r0}	$10^{-12} - 10^{12}$
D, χ	$10^{10} - 10^{12}$
α, β	$10^{-57} - 10^{-45}$

Table 2.1: Estimates of important variables and quantities that appear in (2.26)-(2.32).

Given the small estimated values of α and β, we consider the limit $\alpha, \beta \to 0^+$ in the forthcoming analysis.

2.2 Stability Analysis of Constant Curvature Solutions

2.2.1 Steady States

To determine the time-independent solutions of (2.26)-(2.32), we first consider when such solutions occur in the mechanics of the filament. We denote the steady state of a variable by $(\,)^\star$. Given that $v_1^\star = v_3^\star = 0$, (2.7) reduces to $\partial \mathbf{n}^\star / \partial s = \mathbf{0}$ since the only applied force comes from fluid drag, which implies that $\mathbf{n}^\star = \mathbf{0}$ over the entire filament from the free-ends boundary conditions. Similarly from (2.8), $\partial \mathbf{m}^\star / \partial s = \mathbf{0}$, which implies $\mathbf{m}^\star = \mathbf{0}$ for all s using the same reasoning. In terms of dependent variables, steady states occur when $v_1^\star = v_3^\star = w_2^\star = n_1^\star = n_3^\star = 0$ and $\kappa^\star = c^\star$ throughout the filament.

However, the adhesion kinetics of the proteins specifies that only certain solutions for $c^\star$ will be allowed due to thermodynamic constraints, the form of which are determined by solving (2.32) for $\partial c^\star / \partial t = 0$. For the present analysis however, we focus on steady solutions which are spatially uniform. This simplification gives the following criterion for time-independent states using the result $\kappa^\star = c^\star$:

$$f(\kappa^\star) = P \exp\left(-\frac{\xi}{2}\left(\kappa^\star - \kappa_t\right)^2\right) - \kappa^\star = 0, \tag{2.33}$$

which can have 1, 2, or 3 solutions all of which are non-zero and positive, given that $P > 0$. This latter point is illustrated by plotting $f(\kappa^\star)$ for the parameters $P = 10$ and $\kappa_t = 5.5$ with (a) $\xi = 0.05$, (b) $\xi = 0.2274$, and (c) $\xi = 0.8$ in Fig. 2.2. It is interesting to note that the possibility of up to 3 constant curvature steady states

agrees with previous work which was based on minimizing the free-energy associated with a cylindrical lipid bilayer tube [48].

We note that if $\xi \gg 1$, corresponding to low temperature environments or proteins with large bending stiffness, then (2.33) suggests that $\kappa^\star \to \left\{0^+, \kappa_t^-, \kappa_t^+\right\}$ depending on the extent of protein attachment and the concentration of proteins in the surrounding region, both of which are encoded in P. If P is sufficiently large, then proteins can be thermodynamically forced to attach and, given that the bending stiffness of the proteins is very large, the curvature of the filament is largely determined by the intrinsic curvature of the protein which attaches and acts as a scaffold when uniformly distributed along the rod, leading to $\kappa^\star \to \left\{\kappa_t^-, \kappa_t^+\right\}$. If P is not sufficiently large, then it is thermodynamically undesirable for any proteins to attach to the filament given the large amount of energy necessary to bend the proteins so that they match the filament shape, so $\kappa^\star \to 0^+$.

2.2.2 Linear Stability Analysis

We now study the stability of the spatially uniform steady states subject to imposed perturbations. We linearize around the equilibrium solutions of (2.26)-(2.32) for $\alpha, \beta \to 0^+$ by introducing the ansatz $h = h^\star + \delta_h \exp\left(iks + \sigma t\right)$ for $h = \{v_1, v_3, w_2, \kappa, n_1, n_3, c\}$, where $h^\star$ satisfies the time-independent constant curvature solutions discussed in Section 2.2.1 and it is assumed that $\delta_h \ll 1$. The real part of the parameter σ determines whether a perturbation with wavenumber k will grow or decay in time. The goal is to find a dispersion relation connecting σ and k.

We first apply the ansatz to the mechanics of the filament (i.e. (2.26)-(2.31)) and find that all δ_j for $j = \{v_1, v_3, w_2, n_1, n_3\}$ can be expressed in terms of δ_κ and δ_c to linear order. Eliminating these δ_j gives the following relation between δ_κ and δ_c:

$$\sigma \delta_\kappa = H\left(\delta_c - \delta_\kappa\right), \tag{2.34}$$

where $H = 2k^2\left(k^2 - \kappa^{\star 2}\right)^2 / \left(2k^2 + \kappa^{\star 2}\right)$.

Applying the ansatz to protein adhesion (i.e. (2.32)), we can use Taylor expansions around $\delta_\kappa = 0$ to approximate the exponentials and neglect $\delta_\kappa \delta_c$ and δ_k^2 terms to derive the relation:

$$\sigma \delta_c = F \delta_\kappa - G \delta_c, \tag{2.35}$$

where:

$$F = AB\xi P\left(\kappa_t - \kappa^\star\right) - 2\chi\kappa^\star\left(\kappa^\star - \kappa_t\right)k^2, \tag{2.36}$$

$$G = A + Dk^2, \tag{2.37}$$

$$A = K_{r0}\exp\left(\frac{1}{2}\left(\xi - \xi_{\text{ts}}\right)\left(\kappa^\star - \kappa_t\right)^2\right) > 0, \tag{2.38}$$

$$B = \exp\left(-\frac{\xi}{2}\left(\kappa^\star - \kappa_t\right)^2\right) > 0. \tag{2.39}$$

We express (2.34)-(2.35) in matrix form:

$$\sigma\begin{bmatrix}\delta_\kappa \\ \delta_c\end{bmatrix} = \begin{bmatrix}-H & H \\ F & -G\end{bmatrix}\begin{bmatrix}\delta_\kappa \\ \delta_c\end{bmatrix} = M\begin{bmatrix}\delta_\kappa \\ \delta_c\end{bmatrix}, \tag{2.40}$$

so that σ is an eigenvalue of M. The characteristic polynomial for σ is:

$$0 = \sigma^2 + \left(G + H\right)\sigma + H\left(G - F\right), \tag{2.41}$$

which has real solutions except if the system is dominated by protein drift (i.e. $\chi \gg D, K_{r0}$).

This is the dispersion relation which determines σ as a function of k. In the short wave limit (i.e. $k \to \infty$), we have:

$$\sigma_1 = -k^4 + O\left(k^2\right), \tag{2.42}$$

$$\sigma_2 = -D_{\text{eff}}k^2 + O\left(1\right), \tag{2.43}$$

whilst in the long wave limit (i.e. $k \to 0^+$):

$$\sigma_1 = \frac{2\kappa^{\star 2}}{A}\left(F_0 - A\right)k^2 + O\left(k^4\right), \tag{2.44}$$

$$\sigma_2 = -A + O\left(k^2\right), \tag{2.45}$$

where $D_{\text{eff}} = D + 2\chi\kappa^\star\left(\kappa^\star - \kappa_t\right)$ is the effective diffusion of proteins on the filament with the inclusion of drift effects and $F_0 = \lim_{\chi\to 0} F$.

Some comments regarding (2.42)-(2.45) are in order. First, (2.42) and (2.43) suggest that $\sigma \leq 0$ for $k \to \infty$, provided $D_{\text{eff}} \geq 0$, which implies that the 1D self-assembly system is well-posed. However, since $D, \chi, \kappa^\star > 0$, D_{eff} can become negative when the curvature of the filament is less than the target curvature of the protein $\kappa^\star < \kappa_t$ and protein movement is drift dominated, $\chi \gg D$. For the forthcoming analysis, we only consider well-posed systems where $D > \chi$.

Second, (2.44) shows that the stability of the time-independent constant curvature solutions is determined by $F_0 - A$, which only depends on the shape of the filament and the nature of the protein adhesion kinetics. The process of protein attachment can both stabilize and destabilize the curvature of the filament. Instabilities arise when $F_0 - A > 0$, provided $D_{\text{eff}} > 0$, which reduces to the criterion $\kappa_t - \kappa^\star > 1/B\xi P$. Given that $B, \xi, P > 0$, unstable solutions only exist for filament curvatures less than the target protein curvature $\kappa^\star < \kappa_t$. Additionally, the magnitude of the instability is directly proportional to the degree of protein recruitment K_{r0} and the extent of protein attachment to the filament together with the concentration of proteins in the surrounding region P.

To summarize, we generate a bifurcation diagram of the constant curvature steady states as a function of ξ for $P = 10$ and $\kappa_t = 5.5$ in Fig. 2.2. We note that upon initially increasing the persistence length from 0, there is only one spatially uniform and globally stable solution until $\xi = \xi_{\text{crit}} \approx 0.2274$, such that $F_0 - A = 0$. A saddle-node bifurcation appears which splits into two other possible solutions, one being linearly stable and of low curvature and the other being linearly unstable. As ξ increases even further, the unstable and highly curved stable solution asymptotically approach $\kappa_t = 5.5$ as $\xi \to \infty$, given the thermodynamic forcing from P.

We also create phase diagrams of P/κ_t vs. $\xi\kappa_t^2$ to show the linearly stable and unstable regions for $\kappa^\star = \{2.6996 \times 10^{-6}, 4.1790, 6.4384\}$ (shown in Fig. 2.3(a), (b), and (c) respectively) with $\kappa_t = 5.5$ in the regime of biologically realistic parameters, according to Table 1. We observe that when increasing ξ/κ_t^2 from 0 whilst keeping $\kappa^\star$ constant, the low and high curvature solutions remain linearly stable whilst the middle solution transitions from stable to unstable at a critical value of $\xi_{\text{crit}}\kappa_t^2 \approx 5.4796$. When $\xi\kappa_t^2 > \xi_{\text{crit}}\kappa_t^2$, the system features a bistable regime which is divided by the linearly unstable middle curvature solution.

2.2.3 Weakly Nonlinear Analysis for $k \to 0^+$

For $\xi > \xi_{\text{crit}}$, the self-assembly system has bistable high and low curvature solutions that are separated by an unstable branch. To determine the form of the resulting solution when the unstable curvature is perturbed, we study the immediate region around the bifurcation by introducing $F_0 - A = \epsilon$ for $\epsilon \ll 1$. In this case, the nonlinearities are weak and the unstable modes grow slowly such that a functional form for the solution can be found by rescaling time and space [15].

At the bifurcation, $\sigma = 0$ which suggests $\delta_\kappa = \delta_c$ and $\delta_{v_1} = \delta_{v_3} = \delta_{w_2} = \delta_{n_1} = \delta_{n_3} = 0$ for $k \to 0^+$ from the linear analysis. By using balancing arguments, we find

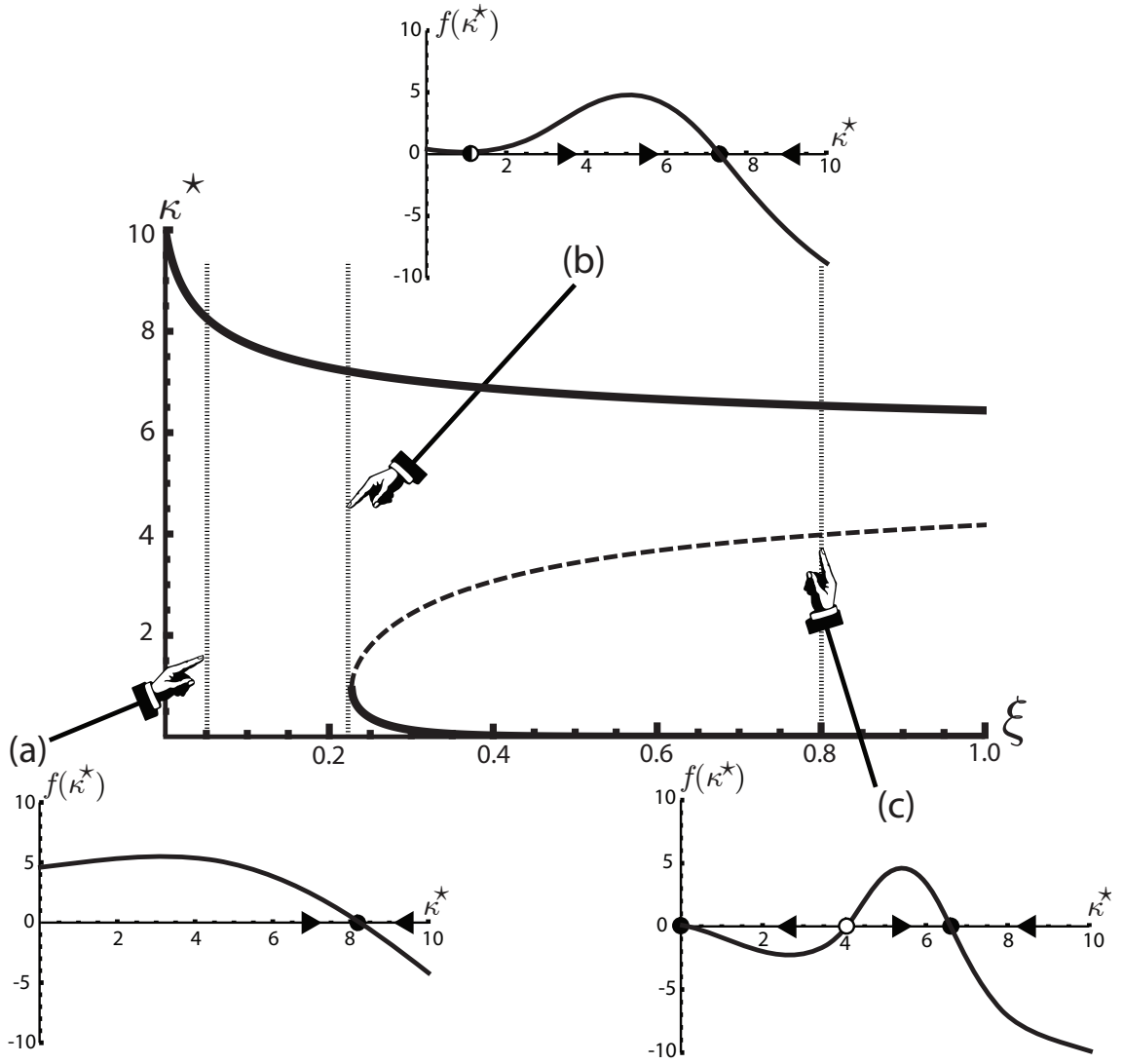

Figure 2.2: Bifurcation diagram of the spatially uniform steady states $\kappa^\star$ as a function of the protein persistence length ξ and plots of $f(\kappa^\star)$, as defined in (2.33), with (a) $\xi = 0.05 < \xi_{\text{crit}}$, (b) $\xi = 0.2274 \approx \xi_{\text{crit}}$, and (c) $\xi = 0.8 > \xi_{\text{crit}}$. The other parameters are $P = 10$ and $\kappa_t = 5.5$. As ξ increases, there is one globally stable solution (denoted by a solid line) until $\xi = \xi_{\text{crit}} \approx 0.2274$, whereby a saddle-node bifurcation appears and introduces two new solutions; one which is linearly stable whilst the other is unstable (denoted by a dashed line).

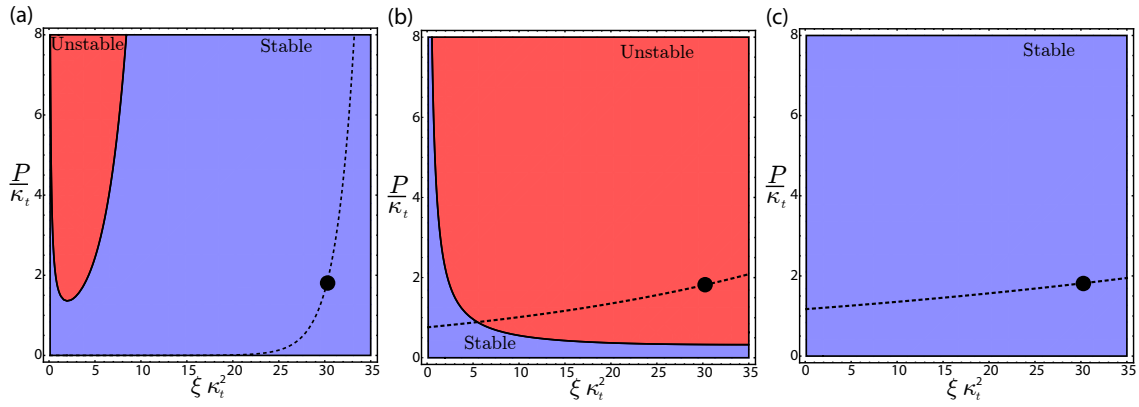

Figure 2.3: Phase diagrams of P/κ_t vs. $\xi\kappa_t^2$ for $\kappa_t = 5.5$ with (a) $\kappa^\star = 2.6996 \times 10^{-6}$, (b) $\kappa^\star = 4.1790$, and (c) $\kappa^\star = 6.4384$. Blue and red zones correspond to linearly stable and unstable regions respectively, according to (2.44). $\kappa^\star$ is constant along the dashed line whilst the black dot corresponds to $\xi = 1$ and $P = 10$ used to generate Fig. 2.5 and 2.6.

the correct scaling is (see Appendix A for details):

$$\kappa = \kappa^\star + \epsilon\delta^{(0)}(t_1, s_1) + \epsilon^2\delta_\kappa^{(1)}(t_1, s_1) + O\left(\epsilon^3\right), \tag{2.46}$$

$$c = \kappa^\star + \epsilon\delta^{(0)}(t_1, s_1) + \epsilon^2\delta_c^{(1)}(t_1, s_1) + O\left(\epsilon^3\right), \tag{2.47}$$

$$v_1 = \epsilon^3\delta_{v_1}^{(1)}(t_1, s_1) + O\left(\epsilon^4\right), \tag{2.48}$$

$$v_3 = \epsilon^{5/2}\delta_{v_3}^{(1)}(t_1, s_1) + O\left(\epsilon^{7/2}\right), \tag{2.49}$$

$$w_2 = \epsilon^{5/2}\delta_{w_2}^{(1)}(t_1, s_1) + O\left(\epsilon^{7/2}\right), \tag{2.50}$$

$$n_1 = \epsilon^{5/2}\delta_{n_1}^{(1)}(t_1, s_1) + O\left(\epsilon^{7/2}\right), \tag{2.51}$$

$$n_3 = \epsilon^3\delta_{n_3}^{(1)}(t_1, s_1) + O\left(\epsilon^4\right), \tag{2.52}$$

for slow time scale $t_1 = \epsilon^2 t$ and rescaled space $s_1 = \epsilon^{1/2}s$.

We divide the system into the contributions of the filament mechanics and the protein adhesion kinetics and consider each part separately. As before, we can express $\delta^{(0)}$, $\delta_\kappa^{(1)}$, and $\delta_c^{(1)}$ in terms of $\delta_j^{(1)}$ for $j = \{v_1, v_3, w_2, n_1, n_3\}$ and find the contribution from the filament mechanics (i.e. (2.26)-(2.31)) reduces to:

$$\frac{\partial\delta^{(0)}}{\partial t_1} = 2\kappa^{\star 2}\frac{\partial^2}{\partial s_1^2}\left(\delta_\kappa^{(1)} - \delta_c^{(1)}\right). \tag{2.53}$$

Applying a similar treatment to (2.32), we use Taylor expansions around $\epsilon = 0$ to obtain:

$$\delta_\kappa^{(1)} - \delta_c^{(1)} = -\frac{1}{A}\left(\delta^{(0)} - \nu\left(\delta^{(0)}\right)^2 + D_{\text{eff}}\frac{\partial^2\delta^{(0)}}{\partial s_1^2}\right), \tag{2.54}$$

where $\nu = AB\xi P/2 - (\xi - \xi_{\rm ts})(\kappa^\star - \kappa_t)(F_0 - A) \geq 0$, given that $\kappa_t > \kappa^\star$, $F_0 - A = \epsilon > 0$ and the estimated values of $\xi, \xi_{\rm ts} \leq 10$.

We combine (2.53) and (2.54) to obtain a reduced equation that describes the time-evolution of long-wave perturbations to the unstable constant curvature solutions of κ and c. We introduce the rescaling $\hat{\delta}^{(0)} = \nu\delta^{(0)}$, $\hat{s}_1 = s_1/L_1$, $\hat{t}_1 = 2D_{\rm eff}\kappa^{\star 2}t_1/L_1^4 A$, and $\hat{L}_1 = L_1/D_{\rm eff}^{1/2}$, where $L_1 = \epsilon^{1/2}$ is the rescaled length of the filament, so that the equation becomes (upon dropping the hat symbol):

$$\mu = -L_1^2\delta^{(0)} + L_1^2\left(\delta^{(0)}\right)^2 - \frac{\partial^2\delta^{(0)}}{\partial s_1^2}, \tag{2.55}$$

$$\frac{\partial\delta^{(0)}}{\partial t_1} = \frac{\partial^2\mu}{\partial s_1^2}, \tag{2.56}$$

with boundary conditions given by $\partial\delta^{(0)}/\partial s_1 = 0$, from $\partial c/\partial s = 0$, and $\mu = 0$, from $\kappa = c$ using (2.54), applicable at $s_1 = \{0, 1\}$. We comment that the rescaling of space leads to an exact spatial correspondence between the solutions predicted by (2.55) and (2.56) and (2.26)-(2.32). Therefore, the sizes of patterns that appear in the reduced system governing $\delta^{(0)}$ should be the same for the evolution of κ and c in the larger self-assembly system.

Equations (2.55)-(2.56) form a Cahn-Hilliard type system which is the prototypical model for phase-separation between multiple stable states and subsequent phase coarsening, whereby the areas of a particular state diffuse and merge together forming larger and more homogeneous regions as time evolves. Such systems can be derived from a global energy functional [36] which, for the current system, is written as:

$$\varepsilon = \int_0^1 \frac{L_1^2}{3}\left(\delta^{(0)}\right)^3 - \frac{L_1^2}{2}\left(\delta^{(0)}\right)^2 + \frac{1}{2}\left(\frac{\partial\delta^{(0)}}{\partial s_1}\right)^2 {\rm d}s_1. \tag{2.57}$$

Note, however, that unlike the usual Cahn-Hilliard system, this energy is not bounded below. This functional density has a cubic potential with an unstable state $\delta^{(0)} = 0$ and two stable states $\delta^{(0)} = \{-\infty, 1\}$.

Using the boundary conditions on $\delta^{(0)}$ and μ, we have:

$$\frac{{\rm d}\varepsilon}{{\rm d}t_1} = -\int_0^1 \left(\frac{\partial\mu}{\partial s_1}\right)^2 {\rm d}s_1 \leq 0, \tag{2.58}$$

so that the energy is decreasing for all time. Defining the mass as $\phi = \int_0^1 \delta^{(0)}{\rm d}s_1$, we find that:

$$\frac{{\rm d}\phi}{{\rm d}t_1} = \left[\frac{\partial\mu}{\partial s_1}\right]_0^1 \neq 0, \tag{2.59}$$

which implies that mass is not conserved, unlike the standard Cahn-Hilliard system, due to the given boundary conditions on μ. Note that ϕ is physically related to the mass of attached proteins on the filament. However, given that the number of attached proteins can change due to the thermodynamic constraints on protein recruitment, it is not necessary that ϕ is conserved.

Result (2.59), coupled with the fact that the system energy decreases (i.e. (2.58)) and that $\delta^{(0)} = -\infty$ is a stable solution, might seem alarming in that it could result in unbounded solutions to (2.26)-(2.32) in the bistable regime. However, this aspect would not appear in the full self-assembly system because of the asymmetry that is built into the protein recruitment term derived in (2.18); namely, that $c \in [0, P]$. The concentration of attached proteins cannot be negative. Given that c is bounded from below and that the perturbations to c and κ are the same to $O(\epsilon)$ in the long-wave regime, the curvature of the filament is finite too. In short, ansatzes (2.46)-(2.52) cease to be valid as the solution of the full self-assembly system reaches equilibrium far from the uniform unstable state.

The time-evolution of perturbations to the unstable curvature can be described in the framework of the Cahn-Hilliard system: For a given initial condition $\delta^{(0)}(0, s)$, the long wave perturbations will locally converge to the states $\delta^{(0)} = \{-\infty, 1\}$ forming patterns. These patterns will interact and merge to form more homogeneous regions of a particular stable state until the solution for $\delta^{(0)}$ is spatially uniform for all s_1. It should be noted that the phase-coarsening occurs on a time-scale that depends on the factor $AL_1^4/2D_{\text{eff}}\kappa^{\star 2}$, which means that for smaller effective protein movement D_{eff}, the resolution to a constant solution takes considerably longer. For instance, if D_{eff} is vanishingly small, the patterns locally converge to the bistable solutions and uniformly resolve as $t \to \infty$. Diffusion and drift compete to smooth and preserve the pattern formation respectively for $\kappa^\star < \kappa_t$, given that $D_{\text{eff}} = D + 2\chi\kappa^\star(\kappa^\star - \kappa_t)$ increases for increasing D and decreasing χ.

If $\delta^{(0)}(t_1 = 0, s_1) = 0$ is perturbed by a constant offset, we would expect that it resolves in a spatially uniform manner, however L_1 plays a role in (2.55)-(2.56). To illustrate this length dependence, we numerically solve (2.55)-(2.56), using a second order time-differencing method incorporating Newton-Raphson iteration, with initial condition $\delta^{(0)}(0, s) = 10^{-9}$ for $L_1 = 2\pi$, $L_1 = 4\pi$, and $L_1 = 6\pi$ (shown in Fig. 2.4(a), (b), and (c) respectively), which corresponds to decreasing D_{eff} in the full system. For small L_1, $\delta^{(0)}$ converges to the spatially uniform $\delta^{(0)} = 1$ solution, however as L_1 increases, the resolution is spatially inhomogeneous and is driven by the boundary terms, with the initial pattern formation becoming more oscillatory and occurring in

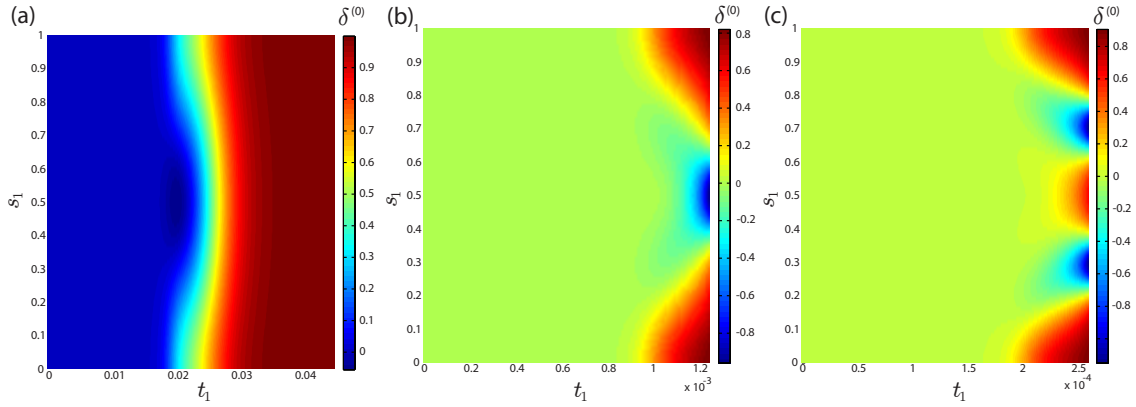

Figure 2.4: Numerical solutions to the reduced perturbation system (2.55)-(2.56) for $\delta^{(0)}(0, s_1) = 10^{-9}$ using a second order time-averaging method and second order spatial finite differences with a Newton-Raphson iterative scheme. In particular: (a) $L_1 = 2\pi$ for final time $t_f = 4.5 \times 10^{-2}$ and time step $\Delta t_1 = 10^{-4}$; (b) $L_1 = 4\pi$ for $t_f = 1.25 \times 10^{-3}$ and $\Delta t_1 = 10^{-5}$; (c) $L_1 = 6\pi$ for $t_f = 2.6 \times 10^{-4}$ and $\Delta t_1 = 10^{-6}$. The discretized spatial grid has spacing given by $\Delta s_1 = 10^{-2}$. The final times have been chosen to show the initial pattern formation, given that $\delta^{(0)}$ is unbounded from below and will approach $-\infty$.

shorter times for increasing L_1. Indeed, if we consider the condition $\mu = 0$, then as L_1 is made larger and $\delta^{(0)} \neq 0$, the only way in which the boundary condition can be satisfied is if $\partial^2\delta^{(0)}/\partial s_1^2$ balances $-L_1^2\delta^{(0)} + L_1^2\left(\delta^{(0)}\right)^2$. In other words, a non-zero second order derivative is introduced at the boundary, the magnitude of which is directly related to L_1, and drives the dynamics of the system so that the solution locally converges to $\delta^{(0)} = \{-\infty, 1\}$.

2.2.4 Pattern Formation and Phase-Coarsening in Protein Concentration

To verify the results predicted by system (2.55)-(2.56), we numerically solve (2.26)-(2.32), using a first order implicit time-differencing method and second-order spatial finite differencing, for κ in the region of the linearly unstable solution shown in Fig. 2.2. The numerical scheme is as follows:

(i) We start the system with an initial condition that satisfies the steady state of the filament, but not the adhesion kinetics of the protein; that is, $\kappa^\dagger = c^\dagger$, $n_1^\dagger = n_3^\dagger = v_1^\dagger = v_3^\dagger = w_2^\dagger = 0$, but $\kappa^\dagger$ does not satisfy (2.33). This requirement bypasses the need for the shooting method often necessary for boundary value problems relating to the Kirchhoff rod, given that all dependent variables associated with the mechanics are known throughout the filament *a priori*.

(ii) We determine the protein adhesion in the new time-step by solving (2.32) for c, enforcing $\partial c/\partial s = 0$ at the ends of the domain. This step does not require a Newton-Raphson iteration method because (2.32) is linear in c.

(iii) Using the updated value for c, we determine the new shape of the filament by solving (2.26)-(2.31) with Newton-Raphson iterations, enforcing the boundary conditions $n_1 = n_3 = 0$ and $\kappa = c$. Steps (ii) and (iii) are repeated until the desired time is reached.

We recreate the pattern formation previously seen in Fig. 2.4 for the full-system by imposing a constant offset to the linearly unstable solution and solving (2.26)-(2.32) with the method outlined above for $\alpha = 10^{-12}$, $\beta = 10^{-12}$, $K_{r0} = 10^3$, $\xi = 1$, $\xi_{\text{ts}} = 1$, $\kappa_t = 5.5$, $P = 10$ and $\chi = 10^{10}$ which are the same parameters that generated Fig. 2.2. Note that α and β were chosen as such to circumvent issues regarding numerical stiffness; namely, allowing for practical spacings in the discretized spatio-temporal grid. Reducing α and β further does not change the plots so we conclude that the numerical solutions have converged and that α and β are still sufficiently small such that the additional filamentary mechanical contributions in the form of dampened oscillations around the bistable solutions, arising from weaker fluid drag, are not included in the computations.

For the listed parameters, $\kappa^\star \approx \{2.6996 \times 10^{-6}, 4.1790, 6.4384\}$ by (33), so we set the initial condition $\kappa(0, s) = c(0, s) = 4.1791$, perturbing the unstable steady state by 10^{-4}, and produce numerical solutions for $\kappa(t, s)$ with $D - \chi = \{50, 5, 0.5\}$, shown in Fig. 2.5(a), (b), and (c) respectively. There are a number of important aspects from Fig. 2.5 to comment on. First, κ locally converges to the linearly stable states $\kappa^\star = \{2.6696 \times 10^{-6}, 6.4384\}$, as is evident in Fig. 2.5(b) and 2.5(c), meaning that κ is bounded from below and remains finite for all time. Second, for $D - \chi = 50$, κ resolves to the spatially uniform stable solution, but as $D - \chi$ decreases to 5 and 0.5, the shape of the filament and the protein concentration is dominated by pattern formation that resolves on longer time scales. Third, decreasing $D - \chi$ results in increasingly oscillatory patterns in κ that occur in shorter times from the initial perturbation; patterns which share similarities in shape and size with the solutions predicted by weakly nonlinear analysis (see Fig. 2.4). We noted previously that this result was due to boundary driven effects given by the condition $\mu = 0$, which derives from the enforcement of zero moments acting at the ends of the filament $\kappa = c$. Indeed, from (2.28), this condition implies that all derivatives of n_1 vanish which suggests that all derivatives of v_1 vanish too from (2.26), given that $n_3 = 0$ is another boundary condition. From a combination of (2.29)-(2.31), this consequence implies

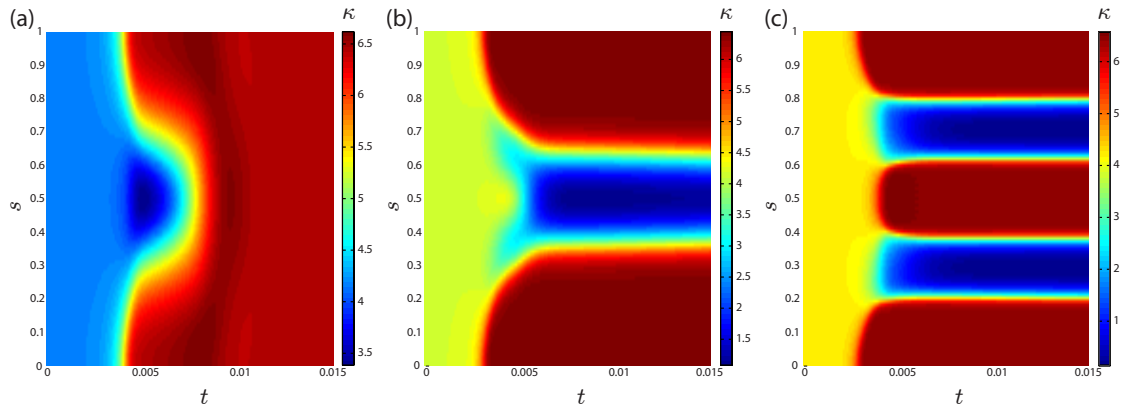

Figure 2.5: Numerical solutions of (2.26)-(2.32) showing $\kappa(t,s)$. An implicit time-differencing method with time-step $\Delta t = 10^{-4}$ to final time $t_f = 0.015$ and second order spatial differencing with grid spacing $\Delta s = 10^{-2}$ was used for $\alpha = 10^{-12}$, $\beta = 10^{-12}$, $K_{r0} = 10^3$, $\xi = 1$, $\xi_{\text{ts}} = 1$, $\kappa_t = 5.5$, $P = 10$, $\chi = 10^{10}$ and (a) $D - \chi = 50$, (b) $D - \chi = 5$, and (c) $D - \chi = 0.5$. The initial conditions are $\kappa(0,s) = c(0,s) = 4.1791$ and $n_1(0,s) = n_3(0,s) = v_1(0,s) = v_3(0,s) = w_2(0,s) = 0$.

that $w_2 = 0$ so that $\partial\kappa/\partial t = 0$. Given that $\kappa = c$, the left hand side of (2.32) is zero so that, in a similar manner as (2.55), the second derivative of c is non-zero, for small $D - \chi$, in order for this boundary condition to be satisfied. All of these aspects were predicted in the weakly nonlinear analysis of Section 2.2.3.

As a final illustrative example showing the full resolution of the bistable system, from initial pattern formation to phase-coarsening, we solve (2.26)-(2.32) for the same parameters as per Fig. 2.5 with $D - \chi = 1$ and impose random initial data with amplitude 10^{-4} around the unstable curvature $\kappa^\star = 4.1790$; that is, $\kappa(0,s) = c(0,s) \in [4.1789, 4.1791]$. A realization of the resultant κ and the corresponding shape of the filament in 2D space, obtained by solving the Frenet-Serret equations, are shown in Fig. 2.6. The results illustrate the pattern formation, resulting from local convergence of κ and c to the stable steady states $\{2.6696 \times 10^{-6}, 6.4384\}$, which physically corresponds to proteins aggregating to form regions of high and low curvature, and slow spatially uniform resolution to the highly curved steady state due to a combination of protein recruitment and protein movement along the filament.

2.3 Competing Protein Processes

As mentioned previously, there is an in-built asymmetry in the 1D self-assembly system due to the protein recruitment term that was derived; namely, that $c \in [0, P]$ so that negative filament curvatures could never be possible. It was also implied that

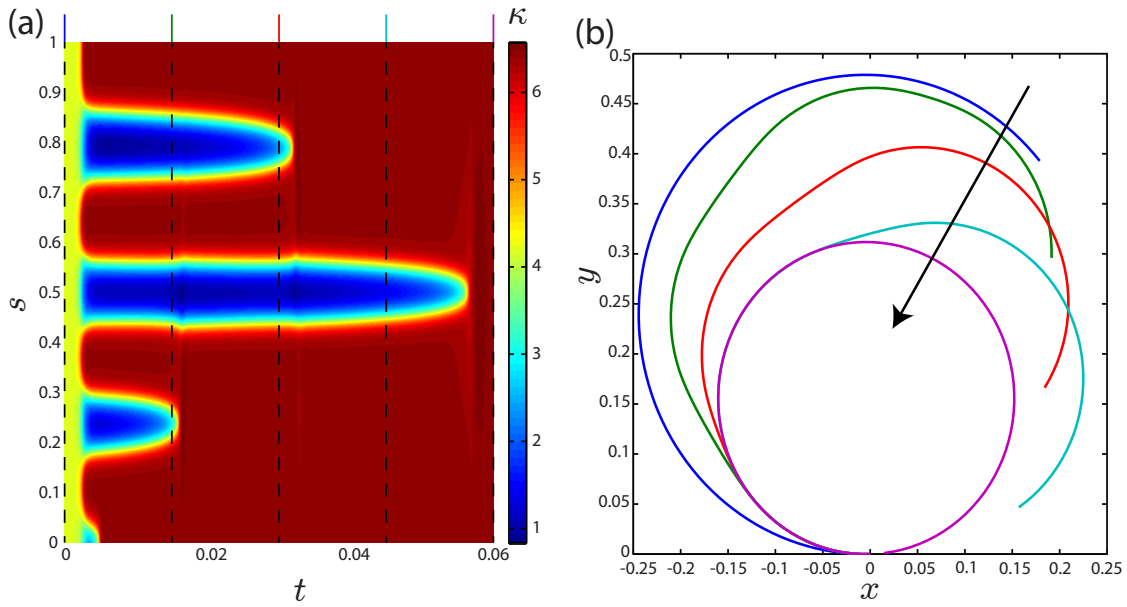

Figure 2.6: Time-evolution of the curvature profile $\kappa(t,s)$ (shown in (a)) and the corresponding shape of the filament in 2D space at $t = \{0, 0.015, 0.03, 0.045, 0.06\}$ (shown in (b)), resulting from the numerical solutions of (2.26)-(2.32) with time-step $\Delta t = 5 \times 10^{-5}$ to final time $t_f = 0.06$ and grid spacing $\Delta s = 10^{-2}$. In particular, the parameters $\alpha = 10^{-12}$, $\beta = 10^{-12}$, $K_{r0} = 10^3$, $\xi = 1$, $\xi_{\text{ts}} = 1$, $\kappa_t = 5.5$, $P = 10$, $\chi = 10^{10}$, and $D - \chi = 1$ were used, together with random initial data $\kappa(0,s) = c(0,s) \in [4.1789, 4.1791]$ and $n_1(0,s) = n_3(0,s) = v_1(0,s) = v_3(0,s) = w_2(0,s) = 0$. Arrow corresponds to increasing time.

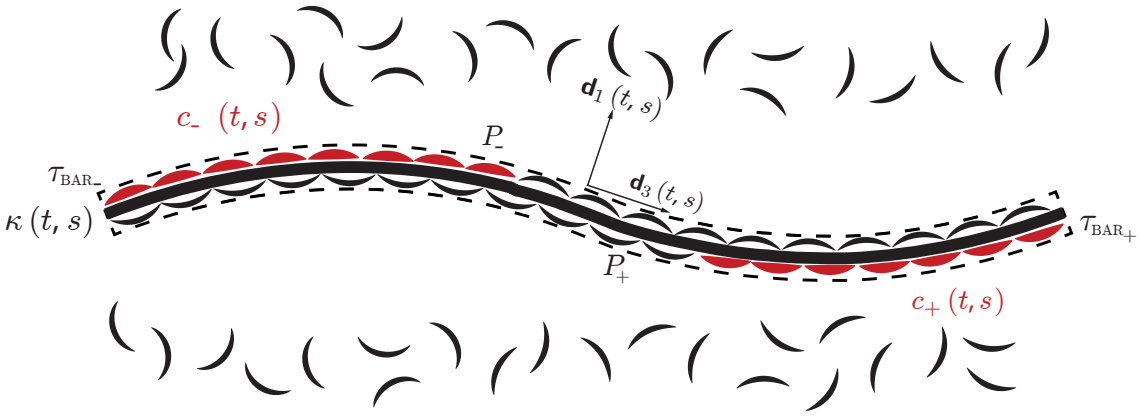

Figure 2.7: The extended 1D self-assembly model. Proteins are recruited to the positive side, as with the single protein case, but also on the opposite side, which is denoted as being negative. The associated characteristic protein parameters for a particular species have $(_+)$ or $(_-)$ subscripts depending on the side to which they attach.

proteins only attach onto one side of the filament and cause its intrinsic curvature to change due to the presence of c in (2.28). There is no reason to suggest that proteins cannot also attach onto the opposite side of the filament. We extend the formalism presented in Section 2.1.1 and 2.1.2 to include the effects of multiple BAR protein types attaching and inducing curvature on both sides of the filament and study the constant curvature solutions that arise from this system.

2.3.1 Inclusion of Multiple Proteins

We suppose the filament now divides the cellular fluid into two sections and label a positive $(+)$ and negative $(-)$ side of the filament where BAR proteins of a particular type only occupy. It is assumed that no protein mixing occurs at the boundary between the positive and negative regions of the fluid. We only consider proteins which induce positive curvature upon attaching to the positive side of the filament and negative curvature attaching to the negative side, and not the presence of inverse proteins, such as the I-BAR, which induce curvature in an opposite manner [34], though such proteins can be included in the model. Proteins attaching onto the positive side of the filament see the curvature as being κ whilst those attaching onto the negative side see the curvature $-\kappa$. Lastly, we assume that the movement of a particular species along the filament occurs independently of all other attached BAR protein types; any interaction between proteins is mediated through κ.

Suppose that we have N_+ different types of proteins attaching to the positive side

and N_- types attaching to the opposing negative side. The number of proteins per unit length of the i^{th} type on the positive side is c_i^+ while the associated characteristic protein parameters (i.e. its target curvature, persistence length, etc.) are generally given with the superscript and subscript
Ω_i^+ for $\Omega = \{\gamma, \tau_{\text{BAR}}, K_{r0}, K_{\text{eqm}}, K_{\text{int}}, \xi, \xi_{\text{ts}}, \kappa_t, P, D, \chi\}$. Similarly, the concentration of the j^{th} type of proteins on the negative side is c_j^- with characteristic protein parameters Ω_j^- (see Fig. 2.7). For the forthcoming analysis, all variables will be taken to be nondimensionalized in the same manner as in Section 2.1.3.

Since the sign of the resulting curvature the proteins induce on the filament depends on the side to which they have attached, the equations describing the mechanics of the filament in (2.26)-(2.27) and (2.29)-(2.31) remain the same except for (2.28), which becomes:

$$\beta \frac{\partial w_2}{\partial t} = \frac{\partial}{\partial s}\left(\kappa - \sum_{i=1}^{N_+} c_i^+ + \sum_{j=1}^{N_-} c_j^-\right) + n_1, \tag{2.60}$$

with free-ends boundary conditions given by $n_1 = n_3 = 0$ and:

$$\kappa = \sum_{i=1}^{N_+} c_i^+ - \sum_{j=1}^{N_-} c_j^-, \tag{2.61}$$

applicable at $s = \{0, 1\}$.

The effect of an inverse protein, which induces negative curvature upon attaching onto the positive side of the filament, is equivalent to a non-inverse protein that induces negative curvature by attaching to the negative side of the filament. As such, including the effects of proteins like the I-BAR is a matter of changing the sign of its induced curvature and attaching it to the opposite side of the filament, which can be encoded in (2.60).

The equation describing the attachment and movement of a particular protein species on the positive side of the filament is the same as for the single protein type:

$$\frac{\partial c_i^+}{\partial t} = K_{r0_i}^+ \exp\left(\frac{1}{2}\left(\xi_i^+ - \xi_{\text{ts}_i}^+\right)\left(\kappa - \kappa_{t_i}^+\right)^2\right)\left\{P_i^+ \exp\left(-\frac{\xi_i^+}{2}\left(\kappa - \kappa_{t_i}^+\right)^2\right) - c_i^+\right\} + D_i^+ \frac{\partial^2 c_i^+}{\partial s^2} + \chi_i^+ \frac{\partial}{\partial s}\left[c_i^+ \frac{\partial}{\partial s}\left(\kappa - \kappa_{t_i}^+\right)^2\right], \tag{2.62}$$

with the boundary condition $\partial c_i^+ / \partial s = 0$ at $s = \{0, 1\}$ corresponding to no flux as a result of diffusion. However, for the negative side of the filament, attaching proteins

would see the opposite sign of filament curvature $-\kappa$, so that:

$$\frac{\partial c_j^-}{\partial t} = K_{r0_j}^- \exp\left(\frac{1}{2}\left(\xi_j^- - \xi_{\mathrm{ts}_j}^-\right)\left(-\kappa - \kappa_{t_j}^-\right)^2\right)\left\{P_j^- \exp\left(-\frac{\xi_j^-}{2}\left(-\kappa - \kappa_{t_j}^-\right)^2\right) - c_j^-\right\} + D_j^- \frac{\partial^2 c_j^-}{\partial s^2} + \chi_j^- \frac{\partial}{\partial s}\left[c_j^- \frac{\partial}{\partial s}\left(-\kappa - \kappa_{t_j}^-\right)^2\right], \quad (2.63)$$

with $\partial c_j^- / \partial s = 0$ at $s = \{0, 1\}$.

With the addition of multiple protein processes, the self-assembly model now becomes a system of $N_+ + N_- + 6$ coupled partial differential equations with equations for added proteins being derived by using either (2.62) or (2.63) with the characteristic protein parameters $\{\gamma, \tau_{\mathrm{BAR}}, K_{r0}, K_{\mathrm{int}}, K_{\mathrm{eqm}}, \xi, \xi_{\mathrm{ts}}, \kappa_t, P, D, \chi\}$.

The criterion for time-independent solutions now becomes more complex. As before, the steady state of the filament mechanics occurs for $v_1^\star = v_3^\star = w_2^\star = n_1^\star = n_3^\star = 0$ and:

$$\kappa^\star = \sum_{i=1}^{N_+} \left(c_i^+\right)^\star - \sum_{j=1}^{N_-} \left(c_j^-\right)^\star, \quad (2.64)$$

for all s. However, from the protein adhesion kinetics, the steady state is given by the solution of a coupled set of ordinary differential equations. In the spatially uniform case, the time-independent concentration of proteins on the positive side is:

$$\left(c_i^+\right)^\star = P_i^+ \exp\left(-\frac{\xi_i^+}{2}\left(\kappa^\star - \kappa_{t_i}^+\right)^2\right), \quad (2.65)$$

and for the negative side:

$$\left(c_j^-\right)^\star = P_j^- \exp\left(-\frac{\xi_j^-}{2}\left(-\kappa^\star - \kappa_{t_j}^-\right)^2\right), \quad (2.66)$$

which means that finding the thermodynamically consistent steady states becomes a matter of solving the algebraic system of (2.64)-(2.66) for $\kappa^\star$, $\left(c_i^+\right)^\star$, and $\left(c_j^-\right)^\star$.

2.3.2 Linear Stability Analysis

As per Section 2.2.2, we linearize around the spatially uniform steady states by using the ansatz $h = h^\star + \delta_h \exp\left(iks + \sigma t\right)$ for $h = \{v_1, v_3, w_2, \kappa, n_1, n_3, c_i^+, c_j^-\}$ where the terms $\kappa^\star$, $\left(c_i^+\right)^\star$, and $\left(c_j^-\right)^\star$ satisfy (2.64)-(2.66). Upon substitution into (2.26)-(2.27), (2.60), and (2.29)-(2.32) in the limit $\alpha, \beta \to 0^+$, we again find that all δ_j for $j =$

$\{v_1, v_3, w_2, n_1, n_3\}$ can be expressed in terms of δ_κ, $\delta_{c_i^+}$, and $\delta_{c_j^-}$ to linear order, so that:

$$\sigma\delta_\kappa = -H\delta_\kappa + H\left(\sum_{i=1}^{N_+}\delta_{c_i^+} - \sum_{j=1}^{N_-}\delta_{c_j^-}\right), \tag{2.67}$$

with $H = 2k^2\left(k^2-\kappa^{\star 2}\right)^2/\left(2k^2+\kappa^{\star 2}\right)$ as before.

Applying a similar treatment to proteins attaching on the positive and negative side of the filament, we find from (2.62) and (2.63):

$$\sigma\delta_{c_i^+} = F_i^+\delta_\kappa - G_i^+\delta_{c_i^+}, \tag{2.68}$$

$$\sigma\delta_{c_j^-} = F_j^-\delta_\kappa - G_j^-\delta_{c_j^-}, \tag{2.69}$$

where:

$$F_i^+ = A_i^+B_i^+\xi_i^+P_i^+\left(\kappa_{t_i}^+ - \kappa^\star\right) - 2\chi_i^+\left(c_i^+\right)^\star\left(\kappa^\star - \kappa_{t_i}^+\right)k^2, \tag{2.70}$$

$$G_i^+ = A_i^+ + D_i^+k^2, \tag{2.71}$$

$$F_j^- = A_j^-B_j^-\xi_j^-P_j^-\left(\kappa^\star + \kappa_{t_j}^-\right) + 2\chi_j^-\left(c_j^-\right)^\star\left(\kappa^\star + \kappa_{t_j}^-\right)k^2, \tag{2.72}$$

$$G_j^- = A_j^- + D_j^-k^2, \tag{2.73}$$

with:

$$A_i^+ = K_{r0_i}^+\exp\left(\frac{1}{2}\left(\xi_i^+ - \xi_{\mathrm{ts}_i}^+\right)\left(\kappa^\star - \kappa_{t_i}^+\right)^2\right) > 0, \tag{2.74}$$

$$B_i^+ = \exp\left(-\frac{\xi_i^+}{2}\left(\kappa^\star - \kappa_{t_i}^+\right)^2\right) > 0, \tag{2.75}$$

$$A_j^- = K_{r0_j}^-\exp\left(\frac{1}{2}\left(\xi_j^- - \xi_{\mathrm{ts}_j}^-\right)\left(-\kappa^\star - \kappa_{t_j}^-\right)^2\right) > 0, \tag{2.76}$$

$$B_j^- = \exp\left(-\frac{\xi_j^-}{2}\left(-\kappa^\star - \kappa_{t_j}^-\right)^2\right) > 0. \tag{2.77}$$

An equation incorporating (2.67)-(2.69) can be written so that the linear stability of the spatially homogeneous solutions is found by determining the eigenvalues of a $(N_+ + N_- + 1)\times(N_+ + N_- + 1)$ matrix:

$$\sigma\begin{bmatrix}\delta_\kappa\\ \delta_{c_1^+}\\ \vdots\\ \delta_{c_{N_+}^+}\\ \delta_{c_1^-}\\ \vdots\\ \delta_{c_{N_-}^-}\end{bmatrix} = \begin{bmatrix}-H & H & \cdots & H & -H & \cdots & -H\\ F_1^+ & -G_1^+ & 0 & \cdots & \cdots & \cdots & 0\\ \vdots & 0 & \ddots & \ddots & \ddots & \ddots & \vdots\\ F_{N_+}^+ & \vdots & \ddots & -G_{N_+}^+ & \ddots & \ddots & \vdots\\ F_1^- & \vdots & \ddots & \ddots & -G_1^- & \ddots & 0\\ \vdots & \vdots & \ddots & \ddots & \ddots & \ddots & 0\\ F_{N_-}^- & 0 & \cdots & \cdots & 0 & 0 & -G_{N_-}^-\end{bmatrix}\begin{bmatrix}\delta_\kappa\\ \delta_{c_1^+}\\ \vdots\\ \delta_{c_{N_+}^+}\\ \delta_{c_1^-}\\ \vdots\\ \delta_{c_{N_-}^-}\end{bmatrix}. \tag{2.78}$$

We can solve (2.78) analytically for the case $G_1^+ = \cdots = G_{N_+}^+ = G_1^- = \cdots = G_{N_-}^- = G$, which corresponds to the species of proteins having the same chemical and diffusion characteristics but being introduced around the filament with different concentrations P. We define the difference of protein adhesion contributions on the positive and negative side of the filament:

$$F_{\text{diff}} = \sum_{i=1}^{N_+} F_i^+ - \sum_{j=1}^{N_-} F_j^-. \tag{2.79}$$

In this instance, the characteristic polynomial for σ becomes:

$$0 = (\sigma + G)^{(N_+ + N_- - 1)} \left[\sigma^2 + (G + H)\,\sigma + H\,(G - F_{\text{diff}})\right]. \tag{2.80}$$

We note that (2.80) has the same form as (2.41) such that, in the limit of $k \to 0^+$, instabilities would also arise. Indeed, the instability criterion shares a similar form as for single protein species driven assembly:

$$F_{\text{diff}}^0 - A > 0, \tag{2.81}$$

where $F_{\text{diff}}^0 = \lim_{\chi_i^+, \chi_j^- \to 0} F_{\text{diff}}$ and A is defined in (2.38) and is the same for the case of chemically similar proteins.

Equation (2.81) can be interpreted physically. In Section 2.2.2, we found that the adhesion kinetics of one protein species was the driving process of instabilities for filament curvatures less than the protein target curvature. Criterion (2.81) suggests that when multiple proteins are introduced, it is the combined contributions of the adhesion kinetics on both sides of the filament that determine whether a particular solution is unstable. For positive $\kappa^\star$ that is unstable, proteins recruited on the positive side of the filament act as a means of destabilization, whilst those attaching to the negative side stabilize. The opposite applies for negative $\kappa^\star$, given the $-\kappa^\star$ factor in F_j^-. In other words, the competition of stabilizing and destabilizing proteins on opposing sides of the filament determines the overall stability of the filament's shape.

For protein species with different values of G, the eigenvalues of the matrix in (2.78) do not allow for a simple form of solution due to coupling between G_i^+ and G_j^- terms; the adhesion interactions mediated by the curvature of the filament play a higher role in determining the stability of the final self-assembled structure and can therefore only be solved under limiting cases or numerically.

2.4 Conclusion

2.4.1 Chapter summary

In the present work, we derived a model for the self-assembly of a 1D continuum by means of curvature inducing BAR proteins in order to determine the role that interactions between the filamentary mechanics and the protein adhesion kinetics plays in the resultant shapes. In particular, we considered an inextensible, unshearable planar Kirchhoff rod that was freely floating in a fluid and coupled its intrinsic curvature to the number of proteins attached to it. We then derived a time-evolution equation for protein recruitment, that was consistent with the microscopic bending energy of an individual protein, and considered the effects of thermal diffusion and drift to minimize the protein bending energy.

We studied the conditions under which time-independent solutions arose, focusing primarily on those which were spatially uniform. In this instance, the filament mechanics was not sufficient to determine the steady state of the self-assembled system; the thermodynamics of protein adhesion constrained the solutions according to the characteristic parameters of the protein. Furthermore, we established that these same parameters completely defined the corresponding linear stability under long and short wave perturbations. Proteins could act as a means of destabilizing the shape of the filament. For increasing persistence lengths of the attaching proteins, which corresponds to lower temperature environments or proteins with greater mechanical stiffness, there was a single globally stable high curvature solution up until a critical persistence length, whereby a saddle-node bifurcation appeared introducing bistable high and low curvature solutions and a middle unstable solution.

Using weakly nonlinear analysis in the long wave limit, we demonstrated that perturbing the unstable curvature resembled a Cahn-Hilliard type problem; proteins would aggregate to form regions of high and low curvature which interacted and merged to form a stable spatially uniform filament shape. The time-scale in which this coarsening occurred was inversely dependent on the effective motion of proteins, with thermal diffusion acting as a means of smoothing the pattern and drift serving to maintain it. However, we showed that even perturbing the unstable state with a constant offset could result in pattern formation in the protein concentration due to the boundary conditions imposed on the filament; namely, that there were no applied moments at its ends.

We extended the self-assembly model to study the effects of multiple protein types attaching to both sides of the filament. The criterion of time-independent solutions in

this instance was more complicated due to the additional thermodynamic inclusions from protein recruitment, all of which was mediated through the curvature of the filament. A means of determining the linear stability of spatially uniform solutions was outlined and analytically solved for the case of chemically similar protein species with the same diffusion constants being introduced around the filament with different maximum concentrations. Each individual protein type contributed to the stability of the final filament shape. Whereas in the single protein species case whereby proteins could act as a means of destabilization, we established that protein types attaching to the opposite side of the filament stabilized the shape. Proteins on opposing ends competed to determine the overall stability of the filament curvature.

2.4.2 Inadequacy of a filament model

We make some criticisms of the self-assembling filament model. First, the filament was taken to be inextensible, however, as noted in Section 2.1, lipid bilayers have been experimentally shown to be nearly inextensible, being able to withstand strains of $2-3\%$ before rupturing. One can readily include this detail into the aforementioned framework by considering an additional constitutive relation connecting the forces along the tangent of the rod n_3 to the rod's elastic stretch; the latter being a measure of the arclength dilation along the continuum [68].

A second criticism stems from the suggestion that the shaping effects of proteins attached to the filament and the interactions between them are purely local in nature. The constitutive relation (2.9) implies that curvature is only induced at a point whilst the diffusion and drift terms in (2.32) suppose that the proteins only see the concentration of proteins and the shape of the underlying filament that is in the proteins' immediate neighborhood. These aspects of the model are at ends with an increasing amount of both experimental and computational work [85, 87, 96] which suggest that the curvature induced by proteins is global and the membrane-mediated interaction between proteins is indirect and long-range. The filament model with free-ends cannot reproduce this phenomenon. To see why this is the case, consider a filament with two curvature-inducing proteins that are spaced a non-zero arclength apart and suppose there is no chemical kinetics (see Fig. 2.8). The resulting shape of the filament, which satisfies (2.11)-(2.16) with free ends boundary conditions, features straight sections from its free ends as well as the connection between the proteins. The only curved sections occur where the proteins are embedded. As a consequence, the proteins do not drift towards or away from each other as a result of imposing

Figure 2.8: Two proteins (shown as crescents) embedded on a filament (shown as black line) with a non-zero separation in arclength. This shape satisfies the kinematic and mechanical filament relations (2.11)-(2.16) with free ends boundary conditions. The proteins do not interact as a result of the underlying filament shape, given that the terms that govern their movement are purely local.

curvature on the filament and there is no global interactions as a result of the underlying filament curvature. Self-assembly of the filament was driven by the adhesion kinetics of the proteins, as opposed to their interactions after being embedded on the filament. The latter has been observed to play a non-trivial role in the biology of the problem, therefore, we investigate membrane-mediated long range interactions in Chapter 3.

2.5 Appendix A: Balancing for weakly nonlinear analysis

We provide a more detailed explanation for the balancing of the dependent variables at the beginning of Section 2.2.3. Given the results of the linear stability analysis of Section 2.2.2, which suggested that, at the bifurcation $\sigma = 0$, $\delta_\kappa = \delta_c$ and $\delta_{v_1} = \delta_{v_3} = \delta_{w_2} = \delta_{n_1} = \delta_{n_3}$ (see (2.35) and (2.34) respectively) to first order, this result implies

the following general balancing:

$$\kappa = \kappa^\star + \epsilon^\gamma \left(\delta^{(0)}\left(t_1, s_1\right) + \epsilon\delta_\kappa^{(1)}\left(t_1, s_1\right)\right) + O\left(\epsilon^{\gamma+2}\right), \tag{2.82}$$

$$c = \kappa^\star + \epsilon^\gamma \left(\delta^{(0)}\left(t_1, s_1\right) + \epsilon\delta_c^{(1)}\left(t_1, s_1\right)\right) + O\left(\epsilon^{\gamma+2}\right), \tag{2.83}$$

$$n_1 = \epsilon^a \delta_{n_1}^{(1)} + O\left(\epsilon^{a+1}\right), \tag{2.84}$$

$$n_3 = \epsilon^b \delta_{n_3}^{(1)} + O\left(\epsilon^{b+1}\right), \tag{2.85}$$

$$v_1 = \epsilon^c \delta_{v_1}^{(1)} + O\left(\epsilon^{c+1}\right), \tag{2.86}$$

$$v_3 = \epsilon^d \delta_{v_3}^{(1)} + O\left(\epsilon^{d+1}\right), \tag{2.87}$$

$$w_2 = \epsilon^f \delta_{w_2}^{(1)} + O\left(\epsilon^{f+1}\right), \tag{2.88}$$

with the general rescaling of time $t_1 = \epsilon^\alpha t$ and space $s_1 = \epsilon^\beta s$.

Substituting these into (2.32) and expanding around $\epsilon = 0$, we find:

$$\epsilon^{\gamma+\alpha}\frac{\partial\delta^{(0)}}{\partial t_1} = -\epsilon^{\gamma+1}\delta^{(0)} + \epsilon^{2\gamma}\nu\left(\delta^{(0)}\right) - A\epsilon^{\gamma+1}\left(\delta_\kappa^{(1)} - \delta_c^{(1)}\right) + \epsilon^{\gamma+2\beta}D_{\text{eff}}\frac{\partial^2\delta^{(0)}}{\partial s_1^2}, \tag{2.89}$$

given that the zeroth order terms vanish as they satisfy the steady state equation (2.33), whilst the linear term $\delta^{(0)}$ appears at $O\left(\epsilon^{\alpha+1}\right)$ since its coefficient is $F_0 - A = \epsilon$. This result implies that, to balance the nonlinear terms, $\gamma + 1 = 2\gamma$ leading to $\gamma = 1$, whilst balancing with the spatial derivative gives $2 = \gamma + 2\beta$ so that $\beta = 1/2$.

Before considering the scaling for time, we consider the general balancing of the dependent variables in (2.26)-(2.31):

$$0 = \epsilon^{a+\frac{1}{2}}\frac{\partial\delta_{n_1}^{(1)}}{\partial s_1} + \epsilon^b\kappa^\star\delta_{n_3}^{(1)} - \epsilon^c\delta_{v_1}^{(1)}, \tag{2.90}$$

$$0 = \epsilon^{b+\frac{1}{2}}\frac{\partial\delta_{n_3}^{(1)}}{\partial s_1} - \epsilon^a\kappa^\star\delta_{n_1}^{(1)} - \frac{\epsilon^d}{2}\delta_{v_3}^{(1)}, \tag{2.91}$$

$$0 = \epsilon^{\frac{5}{2}}\frac{\partial}{\partial s_1}\left(\delta_\kappa^{(1)} - \delta_c^{(1)}\right) + \epsilon^a\delta_{n_1}^{(1)}, \tag{2.92}$$

$$\epsilon^{\alpha+1}\frac{\partial\delta^{(0)}}{\partial t_1} = \epsilon^{f+\frac{1}{2}}\frac{\partial\delta_{w_2}^{(1)}}{\partial s_1}, \tag{2.93}$$

$$0 = \epsilon^{c+\frac{1}{2}}\frac{\partial\delta_{v_1}^{(1)}}{\partial s_1} + \epsilon^d\kappa^\star\delta_{v_3}^{(1)} - \epsilon^f\delta_{w_2}^{(1)}, \tag{2.94}$$

$$0 = \epsilon^{d+\frac{1}{2}}\frac{\partial\delta_{v_3}^{(1)}}{\partial s_1} - \epsilon^c\kappa^\star\delta_{v_1}^{(1)}, \tag{2.95}$$

which implies that $a = 5/2$ from (2.92), $a + 1/2 = b = c$ from (2.90) so that $b = c = 3$, $a = d = 5/2$ from (2.91) and $d = f = 5/2$ from (2.94). The balancing of the dependent variables therefore result in the rescaling of time $\alpha = 2$ from (2.93).

Therefore, from the weakly nonlinear balancing of the filament mechanics, we find to lowest order:

$$0 = \frac{\partial \delta_{n_1}^{(1)}}{\partial s_1} + \kappa^\star \delta_{n_3}^{(1)} - \delta_{v_1}^{(1)}, \tag{2.96}$$

$$0 = \kappa^\star \delta_{n_1}^{(1)} + \frac{1}{2}\delta_{v_3}^{(1)}, \tag{2.97}$$

$$0 = \frac{\partial}{\partial s_1}\left(\delta_{\kappa}^{(1)} - \delta_{c}^{(1)}\right) + \delta_{n_1}^{(1)}, \tag{2.98}$$

$$\frac{\partial \delta^{(0)}}{\partial t_1} = \frac{\partial \delta_{w_2}^{(1)}}{\partial s_1}, \tag{2.99}$$

$$0 = \kappa^\star \delta_{v_3}^{(1)} - \delta_{w_2}^{(1)}, \tag{2.100}$$

$$0 = \frac{\partial \delta_{v_3}^{(1)}}{\partial s_1} - \kappa^\star \delta_{v_1}^{(1)}, \tag{2.101}$$

and, by expressing $\delta_{n_1}^{(1)}$ in terms of $\delta_{v_3}^{(1)}$ using (2.97), rewriting this expression further as $\delta_{w_2}^{(1)}$ using (2.100) and incorporating (2.98) and (2.99), one arrives at (2.53), whilst (2.54) is obtained directly from the balancing arguments previously outlined.

Chapter 3

Curvature-mediated interactions on flat membranes

We study the long-range curvature-mediated interactions between membrane inclusions which break symmetry on a fluid membrane. Chapter 3 proceeds as follows: In Section 3.1, we derive the equilibrium shape equation describing undulations of an approximately flat membrane and outline the necessary boundary conditions needed to determine the interaction energies between two symmetry-breaking membrane inclusions. In Sections 3.2 and 3.3, we derive the interaction laws associated with inclusions which break symmetry in the contact angle that it makes with the surrounding fluid membrane and the geometry of the inclusion boundary respectively. In Section 3.4 we discuss important aspects of this interaction law, such as its implications for the phenomenon of self-assembling aggregation and the associated curvature-mediated interaction field of an individual inclusion, before concluding in Section 3.5.

3.1 Preliminaries

3.1.1 Shape equation

We begin with the Helfrich Hamiltonian which describes the deformation energy of an infinitesimally thin fluid membrane. For such a membrane with mean curvature H, intrinsic mean curvature H_0, and Gaussian curvature K_G, the energy E of deformation is given by [45]:

$$E = \int_{\Omega} \frac{\kappa}{2} \left(H - H_0\right)^2 + \bar{\kappa} K_G \mathrm{d}A, \tag{3.1}$$

where κ is the bending stiffness of the membrane, $\bar{\kappa}$ is its saddle-splay modulus, which is a measure of the membrane's resistance to changes in Gaussian curvature, and the integral is taken over the entire surface of the lipid bilayer Ω.

We consider deformations to an infinite and approximately flat membrane in the Monge parametrization; namely, that the surface extends infinitely in the x-y plane and has an associated height function $\xi h(x,y)$, where $\xi \ll 1$ is a small parameter. We further assume that the height of the membrane does not exhibit larger than logarithmic growth. The distortions of the membrane are described by the position vector:

$$\boldsymbol{r} = (x, y, \xi h(x,y)) . \tag{3.2}$$

We note that the intrinsic mean curvature is $H_0 = 0$ given that, in the absence of deformations, the membrane will be flat, and we calculate the associated mean curvature H. Note that we do not consider the Gaussian curvature term because the corresponding energy contribution will not change if the topology of the surface or its boundary are fixed [7], both of which are the focus of the current analysis.

Determining the tangent vectors in the x and y directions, we find:

$$\frac{\partial \boldsymbol{r}}{\partial x} = \left(1, 0, \xi \frac{\partial h}{\partial x}\right), \tag{3.3}$$

$$\frac{\partial \boldsymbol{r}}{\partial y} = \left(0, 1, \xi \frac{\partial h}{\partial y}\right), \tag{3.4}$$

respectively, so that the first fundamental form G is:

$$G = \begin{bmatrix} 1 & 0 \\ 0 & 1 \end{bmatrix} + O\left(\xi^2\right). \tag{3.5}$$

We calculate the double derivatives of (3.2) and the unit normal $\hat{\boldsymbol{n}}$ to obtain:

$$\frac{\partial^2 \boldsymbol{r}}{\partial x^2} = \left(0, 0, \xi \frac{\partial^2 h}{\partial x^2}\right), \tag{3.6}$$

$$\frac{\partial^2 \boldsymbol{r}}{\partial x \partial y} = \left(0, 0, \xi \frac{\partial^2 h}{\partial x \partial y}\right), \tag{3.7}$$

$$\frac{\partial^2 \boldsymbol{r}}{\partial y^2} = \left(0, 0, \xi \frac{\partial^2 h}{\partial y^2}\right), \tag{3.8}$$

$$\hat{\boldsymbol{n}} = \left(-\xi \frac{\partial h}{\partial x}, -\xi \frac{\partial h}{\partial y}, 1\right) + O\left(\xi^2\right), \tag{3.9}$$

leading to the second fundamental form:

$$F = \xi \begin{bmatrix} \frac{\partial^2 h}{\partial x^2} & \frac{\partial^2 h}{\partial x \partial y} \\ \frac{\partial^2 h}{\partial x \partial y} & \frac{\partial^2 h}{\partial y^2} \end{bmatrix} + O\left(\xi^3\right). \tag{3.10}$$

We find the shape operator, $S = G^{-1}F = F + O(\xi^3)$, so that the mean curvature, obtained by finding the trace of S, is:

$$H = \xi \nabla^2 h + O\left(\xi^2\right). \tag{3.11}$$

Therefore, in the regime whereby only bending energies are considered, we find that (3.1) reduces to:

$$E[h] = \int_{\Omega} \frac{\kappa}{2} \left(\nabla^2 h\right)^2 \mathrm{d}A, \tag{3.12}$$

where the energy has been rescaled as $E/\xi^2 \to E$.

By first variation in $h(x, y)$, we find the associated shape equation:

$$\nabla^4 h = 0, \tag{3.13}$$

with the natural boundary condition:

$$0 = \oint_{\partial\Omega} \left(\delta h \frac{\partial}{\partial \hat{\boldsymbol{n}}} \left(\nabla^2 h\right) - \nabla^2 h \frac{\partial \delta h}{\partial \hat{\boldsymbol{n}}} \right) \cdot \mathrm{d}\boldsymbol{S}, \tag{3.14}$$

evaluated at the boundary of the membrane $\partial\Omega$ and where $\partial/\partial\hat{\boldsymbol{n}}$ is the right-hand orientated normal derivative with respect to this boundary and δh is the first variation of the height function.

3.1.2 Inclusion boundary conditions

We now consider a perfectly rigid inclusion whose center is located at (x_i, y_i). We suppose that it has a vertical degree of freedom in the z direction, described by the parameter γ_i. The position vector for the inclusion is given by:

$$\boldsymbol{r}_{\mathrm{inc}} = (x - x_i, y - y_i, \xi\gamma_i). \tag{3.15}$$

We further suppose that the inclusion has two rotational degrees of freedom around the y and x axes, given by $\beta_i^{(1)}$ and $\beta_i^{(2)}$ respectively with $\beta_i^{(j)} \ll 1$ for $j \in \{1, 2\}$ (see Fig. 3.1). To find the new position vector $\boldsymbol{r}_{\mathrm{n}}$ after rotating the original vector $\boldsymbol{r}_{\mathrm{o}}$ around a rotation axis $\boldsymbol{r}_{\mathrm{rot}}$ by an angle η we use the Rodrigues rotation formula, given by [55]:

$$\boldsymbol{r}_n = \boldsymbol{r}_o \cos\eta + (\boldsymbol{r}_{\mathrm{rot}} \times \boldsymbol{r}_o) \sin\eta + \boldsymbol{r}_{\mathrm{rot}} (\boldsymbol{r}_{\mathrm{rot}} \cdot \boldsymbol{r}_o)(1 - \cos\eta). \tag{3.16}$$

We first rotate the inclusion, whose position is described by (3.15), by an angle of $-\xi\beta_i^{(1)}$ around the y-axis $(0, 1, 0)$. According to (3.16), the new position vector $\boldsymbol{r}_{\mathrm{roty}}$ is:

$$\boldsymbol{r}_{\mathrm{roty}} = \Big((x - x_i)\cos\xi\beta_i^{(1)} - \xi\gamma\sin\xi\beta_i^{(1)}, y - y_i, \\ \xi\gamma\cos\xi\beta_i^{(1)} + (x - x_i)\sin\xi\beta_i^{(1)} \Big). \tag{3.17}$$

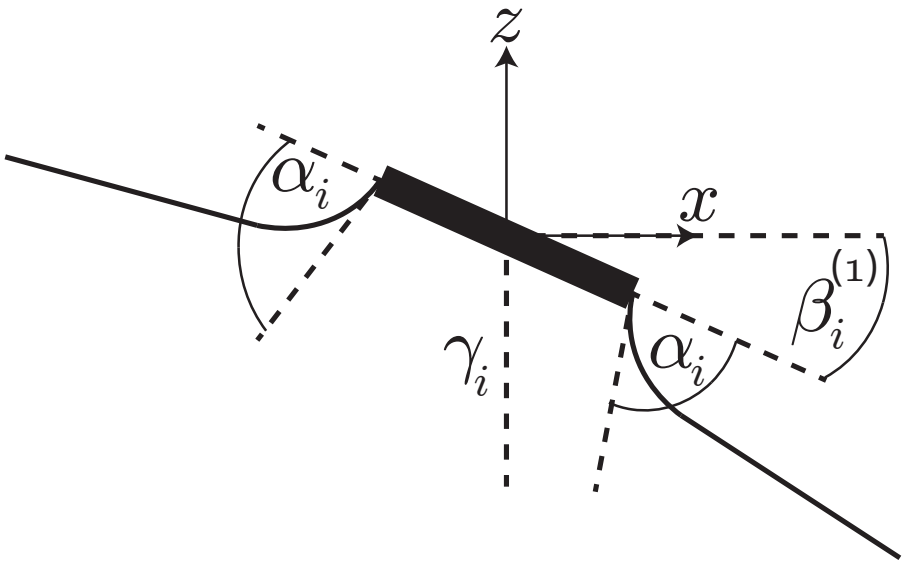

Figure 3.1: A schematic diagram of the boundary conditions (i.e. (3.19) and (3.20)) applicable at the membrane inclusion (denoted by the thick black disk) in the x-z axis. In particular, the inclusion is taken to have a translational degree of freedom along the z-axis, γ_i, and rotational degrees of freedom around the y-axis, $\beta_i^{(1)}$, and the x-axis, $\beta_i^{(2)}$, (latter not shown). Furthermore, the inclusion imposes a contact angle α_i with the surrounding membrane (denoted by the solid black line) and there are also equilibrium conditions on the transverse forces and torques at the boundary (i.e. (3.23)-(3.25)).

A second rotation of $\boldsymbol{r}_{\text{roty}}$ by an angle $\xi\beta_i^{(2)}$ around the x-axis $(1,0,0)$ gives the final position vector of the inclusion:

$$\boldsymbol{r}_{\text{final}} = \Big((x-x_i)+O\left(\xi^2\right),(y-y_i)+O\left(\xi^2\right), \\ \xi\gamma+\xi\beta_i^{(1)}(x-x_i)+\xi\beta_i^{(2)}(y-y_i)+O\left(\xi^3\right)\Big). \quad (3.18)$$

We demand that the height of the membrane deformation $\xi h(x,y)$ meet with the height of the inclusion in the z direction, given by the last entry of (3.18). Therefore, to first order in ξ, we find the boundary condition:

$$h|_{\partial P_i} = \gamma_i+\beta_i^{(1)}(x-x_i)+\beta_i^{(2)}(y-y_i)\Big|_{\partial P_i}, \quad (3.19)$$

where ∂P_i is the projection of the inclusion boundary in the x-y plane. Note that the order in which the rotations are calculated do not matter in the limit of $\xi\beta_i^{(j)} \ll 1$ for $j \in \{1,2\}$.

We now consider the normal derivative of the surrounding membrane with respect to the inclusion boundary in the x-y plane. We suppose that the inclusion enforces a contact angle (equivalent to considering an opening angle, see Fig. 3.1) of $\alpha(x,y)$. To find the boundary condition, we take the normal derivative $\partial/\partial\hat{\boldsymbol{n}}_i$ of (3.19) with respect to the inclusion boundary to obtain:

$$\left.\frac{\partial h}{\partial\hat{\boldsymbol{n}}_i}\right|_{\partial P_i} = \left(\alpha(x,y)+\beta_i^{(1)}\frac{\partial}{\partial\hat{\boldsymbol{n}}_i}(x-x_i)+\beta_i^{(2)}\frac{\partial}{\partial\hat{\boldsymbol{n}}_i}(y-y_i)\right)_{\partial P_i}. \quad (3.20)$$

Lastly, the remaining boundary conditions are given by the balance of transverse force and torques at the inclusion boundary. These are derived by considering the first variations of γ_i and $\beta_i^{(j)}$ in the boundary conditions (3.19) and (3.20):

$$\delta h|_{\partial P_i} = \delta\gamma_i+\delta\beta_i^{(1)}(x-x_i)+\delta\beta_i^{(2)}(y-y_i)\Big|_{\partial P_i}, \quad (3.21)$$

$$\left.\frac{\partial\delta h}{\partial\hat{\boldsymbol{n}}_i}\right|_{\partial P_i} = \delta\beta_i^{(1)}\frac{\partial}{\partial\hat{\boldsymbol{n}}_i}(x-x_i)+\delta\beta_i^{(2)}\frac{\partial}{\partial\hat{\boldsymbol{n}}_i}(y-y_i)\Big|_{\partial P_i}, \quad (3.22)$$

whereby the variation of $\alpha_i(x,y)$ vanishes given that it is a prescribed function.

We substitute (3.21) and (3.22) into the natural boundary condition (3.14) and, assuming that the variations of γ_i, $\beta_i^{(1)}$, and $\beta_i^{(2)}$ are independent of each other, we

obtain three conditions:

$$0 = \delta\gamma_i \oint_{\partial P_i} \frac{\partial}{\partial \hat{\boldsymbol{n}}} \left(\nabla^2 h\right) \cdot \mathrm{d}\boldsymbol{S}, \tag{3.23}$$

$$0 = \delta\beta_i^{(1)} \oint_{\partial P_i} \left[(x - x_i) \frac{\partial}{\partial \hat{\boldsymbol{n}}} \left(\nabla^2 h\right) - \nabla^2 h \frac{\partial}{\partial \hat{\boldsymbol{n}}} (x - x_i) \right] \cdot \mathrm{d}\boldsymbol{S}, \tag{3.24}$$

$$0 = \delta\beta_i^{(2)} \oint_{\partial P_i} \left[(y - y_i) \frac{\partial}{\partial \hat{\boldsymbol{n}}} \left(\nabla^2 h\right) - \nabla^2 h \frac{\partial}{\partial \hat{\boldsymbol{n}}} (y - y_i) \right] \cdot \mathrm{d}\boldsymbol{S}, \tag{3.25}$$

which can be interpreted as statements on the balance of forces along the z-axis and torques around the y and x axis respectively at the inclusion boundary ∂P_i. Note that we have not considered contributions from the membrane boundary because the membrane is taken to extend infinitely and remain bounded away from the inclusion.

3.2 Contact angle symmetry breaking

3.2.1 Set-up of problem

We now study the interactions between perfectly circular and rigid inclusions which break symmetry in the contact angle that they form with the surrounding membrane. In particular, suppose that there are two inclusions, denoted by subscripts 1 and 2 respectively, of radius $\varepsilon^{1/2}$ with $\varepsilon \ll 1$ whose centers are spaced a distance $R = O(1)$ apart (we take $x_1 = 0$, $y_1 = 0$, $x_2 = R$, and $y_2 = 0$ without loss of generality). We parametrize the shape of the membrane immediately around the membrane inclusion by local polar radial and angle variables, $\rho_i \in [1, \infty)$ and $\phi_i \in [0, 2\pi)$, taken from the positive x-axis. These variables are related to x and y by:

$$x - x_i = \varepsilon^{\frac{1}{2}} \rho_i \cos\phi_i, \tag{3.26}$$

$$y - y_i = \varepsilon^{\frac{1}{2}} \rho_i \sin\phi_i, \tag{3.27}$$

where (x_i, y_i) is the position of the ith inclusion's center for $i \in \{1, 2\}$ (see Fig. 3.2).

We suppose that the inclusion enforces a symmetry-breaking opening angle which is not constant, but will depend on the orientation of the inclusion, quantified as ψ_i taken from the positive x-axis. We perturb the isotropic case by expanding the contact angle $\alpha(\rho_i, \phi_i)$ as a Fourier series:

$$\alpha(\phi_i) = \alpha_i^{(0)} + \varepsilon\alpha_i^{(2)} \cos(2\phi_i - 2\psi_i), \tag{3.28}$$

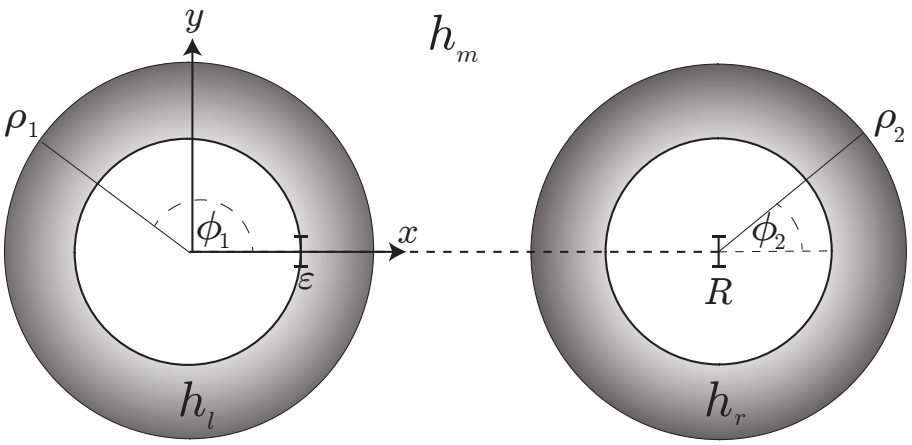

Figure 3.2: A schematic diagram of the interaction of two identical inclusions of radius $\varepsilon^{\frac{1}{2}}$ with $\varepsilon \ll 1$ on an approximately flat membrane, which break symmetry in their contact angle. The inclusions are taken to have perfectly circular boundaries with centers separated by a distance $R = O(1)$. In all, there are three regions in which the membrane shape must be determined by (3.13): The inner layer regions around the inclusions h_l^1 and h_l^2 which are parametrized by local radial-angle coordinates (ρ_i, ϕ_i) (denoted by gray region), and the outer membrane region h_m in the coordinates (x, y) (denoted by the white region). Transformations between these two regions occurs according to (3.26) and (3.27).

where $\alpha_i^{(0)}$ and $\alpha_i^{(2)}$ are $O(1)$. By analogy with electrostatics and magnetism [47], we refer to these constants as the monopole and quadrupole contact angles respectively. These constants are a measure of the opening angle enforced which is fixed and invariant under a rotation of the inclusion around the z-axis by π respectively. Note that we do not include the first Fourier mode $\cos(\phi_i - \psi_i)$ nor higher Fourier modes because these terms do not contribute to the leading order interaction energy.

For the polar parametrization defined in (3.26) and (3.27), we evaluate (3.19) and (3.20) at the inclusion radius (i.e. for $\rho_i = 1$) to obtain:

$$h\big|_{\rho_i=1} = \gamma_i + \varepsilon^{\frac{1}{2}}\beta_i^{(1)}\cos\phi_i + \varepsilon^{\frac{1}{2}}\beta_i^{(2)}\sin\phi_i, \tag{3.29}$$

$$\left.\frac{\partial h}{\partial \rho_i}\right|_{\rho_i=1} = \alpha_i^{(0)} + \varepsilon\alpha_i^{(2)}\cos(2\phi_i - 2\psi_i) + \varepsilon^{\frac{1}{2}}\beta_i^{(1)}\cos\phi_i + \varepsilon^{\frac{1}{2}}\beta_i^{(2)}\sin\phi_i, \tag{3.30}$$

where the normal derivative in (3.30) has reduced to the differential operator $\partial/\partial\rho_i$, given that the inclusion is perfectly circular, and where we have cancelled the factor of $\varepsilon^{1/2}$ from both sides.

The integrals (3.23)-(3.25) provide a further three boundary conditions, which give, for the case of an inclusion whose projection is perfectly circular in the x-y

plane:

$$0 = \int_0^{2\pi} \left[\frac{\partial}{\partial \rho_i} \left(\nabla^2 h \right) \right]_{\rho_i = 1} \mathrm{d}\phi_i, \tag{3.31}$$

$$0 = \int_0^{2\pi} \cos\phi_i \left[\frac{\partial}{\partial \rho_i} \left(\nabla^2 h \right) - \nabla^2 h \right]_{\rho_i = 1} \mathrm{d}\phi_i, \tag{3.32}$$

$$0 = \int_0^{2\pi} \sin\phi_i \left[\frac{\partial}{\partial \rho_i} \left(\nabla^2 h \right) - \nabla^2 h \right]_{\rho_i = 1} \mathrm{d}\phi_i. \tag{3.33}$$

3.2.1.1 Method of interaction energy derivation

We outline the method to determine the interaction energy between two inclusions. There are three regions of interest in which we solve (3.13) for the height function h: the two layer regions close to the inclusion, which we will denote by h_l^1 and h_l^2 respectively and the outer membrane which is far from the inclusions, denoted by h_m (see Fig. 3.2). We first solve for the shape in the layer regions using the local polar variables (ρ_i, ϕ_i) and impose the boundary conditions (3.29)-(3.33) to obtain the leading order solution. From the layer solution, we can then determine the leading order outer membrane solution in the coordinates (x, y). Expanding this outer membrane shape in terms of the local polar coordinates (ρ_i, ϕ_i) using (3.26) and (3.27), we determine the higher order corrections in the layer shape by demanding that the outer membrane and the layer solutions asymptotically match. From these results, we then explicitly compute the energy by integrating (3.12).

3.2.2 Inner layer shapes around the inclusions

We solve (3.13) in a region close to the first inclusion. We use the Fourier representation:

$$h_l^1 = \sum_{n=0}^{\infty} f_n\left(\rho_i\right) \exp\left(\mathrm{i} n \phi_i\right), \tag{3.34}$$

where $f_n\left(\rho_i\right)$ is an arbitrary function to be determined [94], and find, for each mode, the differential equation:

$$0 = \frac{\mathrm{d}^4 f_n}{\mathrm{d}\rho_1^4} + \frac{2}{\rho_1} \frac{\mathrm{d}^3 f_n}{\mathrm{d}\rho_1^3} - \frac{1}{\rho_1^2} \left(2n^2 + 1\right) \frac{\mathrm{d}^2 f_n}{\mathrm{d}\rho_1^2} + \frac{1}{\rho_1^3} \left(2n^2 + 1\right) \frac{\mathrm{d} f_n}{\mathrm{d}\rho_1} + \frac{1}{\rho_1^4} \left(n^4 - 4n^2\right) f_n. \tag{3.35}$$

This equation can be solved for the Fourier modes $n = \{0, 1, 2\}$ to give the general solution:

$$\begin{aligned} h_l^1 = b_0 + b_1 \ln\rho_1 + b_2\rho_1^2 + b_3\rho_1^2 \ln\rho_1 + b_4\rho_1\cos\phi_1 + b_{42}\rho_1\sin\phi_1 \\ + b_6\rho_1\ln\rho_1\cos\phi_1 + b_{62}\rho_1\ln\rho_1\sin\phi_1 + \frac{b_7\cos\phi_1}{\rho_1} + \frac{b_{72}\sin\phi_1}{\rho_1} \\ + b_8\rho_1^2\cos 2\phi_1 + b_{82}\rho_1^2\sin 2\phi_1 + b_{10}\cos 2\phi_1 \\ + b_{102}\sin 2\phi_1 + \frac{b_{11}\cos 2\phi_1}{\rho_1^2} + \frac{b_{112}\sin 2\phi_1}{\rho_1^2}, \end{aligned} \tag{3.36}$$

where $b_q \in \mathbb{R}$ are arbitrary constants.

We comment that, previous analyses of the isotropic problem [41, 101] make the assumption that the membrane height is invariant under the reflection $y \to -y$. This is no longer true for the case of symmetry-breaking inclusions and must be accounted for with the addition of sine Fourier terms. Furthermore, we have not included terms that grow larger than ρ_1^3 as asymptotic matching would imply that these terms are $O\left(\varepsilon^{3/2}\right)$ and higher.

Imposing the balance of force and moments (i.e. (3.31)-(3.33)), we find that $b_3 = b_6 = b_{62} = 0$. Further using (3.29) and (3.30), we obtain:

$$\begin{aligned} h_l^1 = b_0 + \left(\alpha_1^{(0)} - 2b_2\right)\ln\rho_1 + b_2\rho_1^2 + \varepsilon^{\frac{1}{2}}\beta_1^{(1)}\rho_1\cos\phi_1 \\ + \varepsilon^{\frac{1}{2}}\beta_1^{(2)}\rho_1\sin\phi_1 + b_8\rho_1^2\cos 2\phi_1 + b_{82}\rho_1^2\sin 2\phi_1 \\ - \left(2b_8 - \frac{\varepsilon\alpha_1^{(2)}}{2}\cos 2\psi_1\right)\cos 2\phi_1 - \left(2b_{82} - \frac{\varepsilon\alpha_1^{(2)}}{2}\sin 2\psi_1\right)\sin 2\phi_1 \\ + \frac{\left(2b_8 - \varepsilon\alpha_1^{(2)}\cos 2\psi_1\right)\cos 2\phi_1}{2\rho_1^2} + \frac{\left(2b_{82} - \varepsilon\alpha_1^{(2)}\sin 2\psi_1\right)\sin 2\phi_1}{2\rho_1^2}, \end{aligned} \tag{3.37}$$

with $\gamma_1 = b_0 + b_2$ and unknown constants given by b_0, b_2, b_8, b_{82}, $\beta_1^{(1)}$, and $\beta_1^{(2)}$ which will be determined by asymptotic matching with the outer solution.

Similar reasoning gives that the shape of the membrane in the local region of the second inclusion is:

$$\begin{aligned} h_l^2 = \hat{b_0} + \left(\alpha_2^{(0)} - 2\hat{b_2}\right)\ln\rho_2 + \hat{b_2}\rho_2^2 + \varepsilon^{\frac{1}{2}}\beta_2^{(1)}\rho_2\cos\phi_2 \\ + \varepsilon^{\frac{1}{2}}\beta_2^{(2)}\rho_2\sin\phi_2 + \hat{b_8}\rho_2^2\cos 2\phi_2 + \hat{b_{82}}\rho_2^2\sin 2\phi_2 \\ - \left(2\hat{b_8} - \frac{\varepsilon\alpha_2^{(2)}}{2}\cos 2\psi_2\right)\cos 2\phi_2 - \left(2\hat{b_{82}} - \frac{\varepsilon\alpha_2^{(2)}}{2}\sin 2\psi_2\right)\sin 2\phi_2 \\ + \frac{\left(2\hat{b_8} - \varepsilon\alpha_2^{(2)}\cos 2\psi_2\right)\cos 2\phi_2}{2\rho_2^2} + \frac{\left(2\hat{b_{82}} - \varepsilon\alpha_2^{(2)}\sin 2\psi_2\right)\sin 2\phi_2}{2\rho_2^2}, \end{aligned} \tag{3.38}$$

with the constants $\hat{b_q} \in \mathbb{R}$, $\gamma_2 = \hat{b_0} + \hat{b_2}$, and $\hat{b_0}$, $\hat{b_2}$, $\hat{b_8}$, $\hat{b_{82}}$, $\beta_2^{(1)}$, and $\beta_2^{(2)}$ to be determined by asymptotic matching.

3.2.3 Outer membrane shape and asymptotic matching

We note that the leading order shape in the inner region is logarithmic, originating from the center of the inclusion. This aspect, together with the assumption that the membrane height does not grow larger than a logarithm far away from the inclusions, suggests that the leading order outer membrane solution is:

$$h_m = c_0 + \frac{\alpha_1^{(0)}}{2} \ln\left(x^2 + y^2\right) + \frac{\alpha_2^{(0)}}{2} \ln\left((x-R)^2 + y^2\right), \tag{3.39}$$

where $c_0 \in \mathbb{R}$ is an arbitrary constant. Furthermore, we note that higher order corrections to the outer membrane shape are $O(\varepsilon)$ and do not contribute to the final interaction energy.

We now match the outer membrane shape (3.39) with the local shape of the first inclusion (3.37). To do so, we write the variables (x, y) in terms of the local polar variables (ρ_1, ϕ_1) according to (3.26) and (3.27) for $x_1 = y_1 = 0$. Expanding in the limit of $\varepsilon \ll 1$, we obtain:

$$h_m = c_0 + \alpha_2^{(0)} \ln R + \alpha_1^{(0)} \ln\left(\varepsilon^{\frac{1}{2}}\right) + \alpha_1^{(0)} \ln \rho_1 - \frac{\varepsilon^{\frac{1}{2}} \alpha_2^{(0)} \rho_1 \cos\phi_1}{R} - \frac{\varepsilon \alpha_2^{(0)} \rho_1^2 \cos 2\phi_1}{2R^2} + O\left(\varepsilon^{\frac{3}{2}}\right). \tag{3.40}$$

By matching this expanded outer solution with (3.37), we obtain the logarithmic term and find:

$$\gamma_1 = c_0 + \frac{1}{2}\alpha_1^{(0)} \ln\varepsilon + \alpha_2^{(0)} \ln R, \tag{3.41}$$

$$\beta_1^{(1)} = -\frac{\alpha_2^{(0)}}{R}, \tag{3.42}$$

$$b_8 = -\frac{\varepsilon \alpha_2^{(0)}}{2R^2}. \tag{3.43}$$

The remaining unknown constants b_2, b_{82}, and $\beta_1^{(2)}$ are $O\left(\varepsilon^{3/2}\right)$. Physically, (3.41) implies that the first inclusion will rise along the z-axis due to its radius and the monopole contact angle it enforces with the surrounding lipid bilayer, as well as the isotropic deformation imposed by the second inclusion and its separation from the first inclusion. Furthermore, (3.42) gives that the constant contact angle around the second membrane inclusion causes the first inclusion to rotate around the y-axis

whilst (3.43) suggests that this same contact angle results in higher order corrections to the local shape of the first inclusion in the form of $\rho_1^2 \cos 2\phi_1$.

To match the outer membrane solution with the second inclusion, we express (3.39) in the local polar variables (ρ_2, ϕ_2) using (3.26) and (3.27) for $x_2 = R$ and $y_2 = 0$ to obtain:

$$h_m = c_0 + \alpha_1^{(0)} \ln R + \alpha_2^{(0)} \ln\left(\varepsilon^{\frac{1}{2}}\right) + \alpha_2^{(0)} \ln \rho_2 + \frac{\varepsilon^{\frac{1}{2}} \alpha_1^{(0)} \rho_2 \cos\phi_2}{R} - \frac{\varepsilon \alpha_1^{(0)} \rho_2^2 \cos 2\phi_2}{2R^2} + O\left(\varepsilon^{\frac{3}{2}}\right). \quad (3.44)$$

Comparing with (3.38), we find:

$$\gamma_2 = c_0 + \frac{1}{2}\alpha_2^{(0)} \ln \varepsilon + \alpha_1^{(0)} \ln R, \quad (3.45)$$

$$\beta_2^{(1)} = \frac{\alpha_1^{(0)}}{R}, \quad (3.46)$$

$$\hat{b_8} = -\frac{\varepsilon \alpha_1^{(0)}}{2R^2}, \quad (3.47)$$

suggesting that the first inclusion results in a similar vertical lift and rotation of the second inclusion around the y-axis, albeit in the opposite direction, and higher order corrections to its layer shape. Furthermore, the unknown constants $\hat{b_2}$, $\hat{b_{82}}$, and $\beta_2^{(2)}$ are of $O\left(\varepsilon^{3/2}\right)$ and higher.

3.2.4 Interaction energy

We now have sufficient information to determine the dominant interaction energy between the two inclusions. We define the inner layer Laplacian in polar coordinates as ∇_l^2 and find that the Laplacian of the local solution of the first inclusion, using (3.37) and (3.43), is:

$$\nabla_l^2 h_l^1 = -\frac{4\alpha_2^{(0)} \cos 2\phi_1}{R^2 \rho_1^2} - \frac{2\alpha_1^{(2)} \cos\left(2\phi_1 - 2\psi_1\right)}{\rho_1^2} + O\left(\varepsilon^{\frac{1}{2}}\right). \quad (3.48)$$

Note that the factor ε^{-1} comes from the definition of transforming between (x, y) and local polar coordinates (ρ_1, ϕ_1) according to (3.26) and (3.27). Similarly, the Laplacian of the membrane shape in the layer around the second inclusion is, using (3.38) and (3.47):

$$\nabla_l^2 h_l^2 = -\frac{4\alpha_1^{(0)} \cos 2\phi_2}{R^2 \rho_2^2} - \frac{2\alpha_2^{(2)} \cos\left(2\phi_2 - 2\psi_2\right)}{\rho_2^2} + O\left(\varepsilon^{\frac{1}{2}}\right), \quad (3.49)$$

whilst the Laplacian of the outer membrane shape (3.39) vanishes at leading order (i.e. $O(1)$) and is of $O(\varepsilon)$.

We calculate the interaction energy by using the energy functional (3.12) and the Laplacians of the layer regions around the inclusions, so that:

$$V(R,\psi_1,\psi_2) = \frac{\kappa\varepsilon}{2}\left[\int_1^\infty\int_0^{2\pi}\left(\nabla_l^2 h_l^1\right)^2\rho_1 \mathrm{d}\rho_1\mathrm{d}\phi_1 + \int_1^\infty\int_0^{2\pi}\left(\nabla_l^2 h_l^2\right)^2\rho_2\mathrm{d}\rho_2\mathrm{d}\phi_2\right] + O\left(\varepsilon^2\right). \quad (3.50)$$

The additional ε factor comes from transforming the integral from (x,y) coordinates to (ρ_i,ϕ_i) according to (3.26) and (3.27). The term involving the Laplacian of the outer membrane gives negligible $O(\varepsilon^2)$ correction and therefore does not contribute to the leading order calculation of energy.

Evaluating the integral exactly, we find the interaction law:

$$V(R,\psi_1,\psi_2) = \kappa\pi\varepsilon\left[\left(\alpha_1^{(2)}\right)^2 + \left(\alpha_2^{(2)}\right)^2 + \frac{4}{R^2}\left(\alpha_1^{(2)}\alpha_2^{(0)}\cos 2\psi_1 + \alpha_2^{(2)}\alpha_1^{(0)}\cos 2\psi_2\right) + \frac{4}{R^4}\left(\left(\alpha_1^{(0)}\right)^2 + \left(\alpha_2^{(0)}\right)^2\right)\right], \quad (3.51)$$

where we have dropped terms of $O(\varepsilon^2)$.

We further discuss (3.51) in Section 5 after deriving the interaction law between two non-circular inclusions.

3.3 Geometric symmetry breaking

3.3.1 Set-up of problem

We now study the interactions between two non-circular membrane inclusions. We assume that the contact angle $\alpha_i(x,y) = \alpha_i^{(0)}$ is constant along the edge of the membrane inclusion, but the boundary of the inclusion is no longer circular. We take the inclusion to be a symmetric deformed circle with the boundary ρ_b^i given by:

$$\rho_b^i(\phi_i) = 1 - \varepsilon\omega_i\cos(2\phi_i - 2\psi_i), \quad (3.52)$$

where ψ_i is the angle of the inclusion's semi-minor axis with respect to the positive x-axis and $\omega_i = O(1)$ is a measure of the deviation from a circular geometry (see Fig.

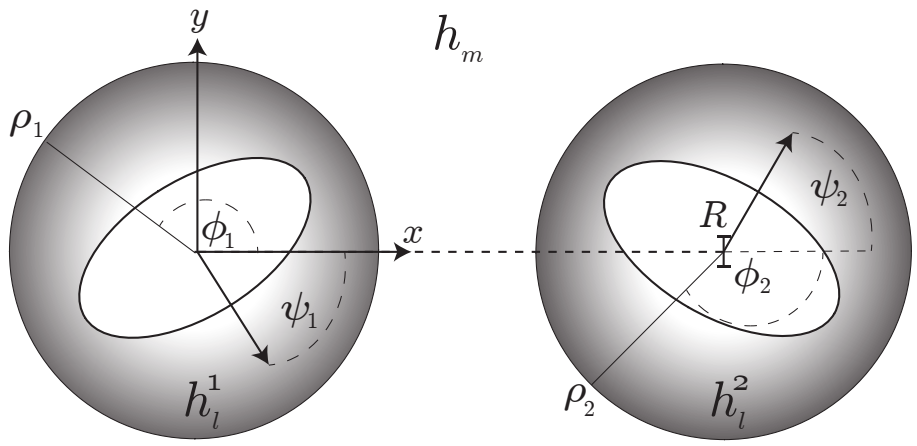

Figure 3.3: A schematic diagram of the interaction of two identical but non-circular inclusions on an approximately flat membrane. The inclusions are taken to have boundaries determined by (3.52) with centers separated by a distance $R = O(1)$ and orientations of their semi-minor axes given by an angle ψ_i with respect to the positive x-axis. As in Section 3.2, there are three regions in which the membrane shape must be determined by (3.13): The inner layer regions around the inclusions h_l^1 and h_l^2 which are parametrized by local radial-angle coordinates (ρ_i, ϕ_i) (denoted by gray region), and the outer membrane region h_m in the coordinates (x, y) (denoted by the white region).

3.3). Note that we continue to use the transformation between inner variables (ρ_i, ϕ_i) and outer variables (x, y) as specified in (3.26) and (3.27) in Section 3.2 and we still suppose that $\varepsilon \ll 1$.

To find the normal vector to the non-circular boundary, we write the boundary as the solution of $f(\rho_i, \phi_i) = 0$:

$$f(\rho_i, \phi_i) = \rho_i + \varepsilon\omega_i \cos(2\phi_i - 2\psi_i) - 1, \tag{3.53}$$

and take the gradient of this expression to find:

$$\nabla f = \left(\frac{1}{\varepsilon^{\frac{1}{2}}} \frac{\partial}{\partial \rho_i} \hat{\boldsymbol{\rho}}_i + \frac{1}{\varepsilon^{\frac{1}{2}} \rho_i} \frac{\partial}{\partial \phi_i} \hat{\boldsymbol{\phi}}_i \right) (\rho_i + \varepsilon\omega_i \cos(2\phi_i - 2\psi_i) - 1), \tag{3.54}$$

where $\hat{\boldsymbol{\rho}}_{\boldsymbol{i}}$ and $\hat{\boldsymbol{\phi}}_{\boldsymbol{i}}$ are the unit radial and polar vectors taken from the center of the ith inclusion respectively and the factor of $\varepsilon^{1/2}$ in the derivatives arises from the transformation from the outer to inner parametrization according to (3.26) and (3.27).

The unit normal $\hat{\boldsymbol{n}}$ to the boundary is then calculated by $\hat{\boldsymbol{n}} = \nabla f / |\nabla f|$:

$$\hat{\boldsymbol{n}} = \hat{\boldsymbol{\rho}}_i - 2\varepsilon\omega_i \sin(2\phi_i - 2\psi_i) \hat{\boldsymbol{\phi}}_i + O(\varepsilon^2), \tag{3.55}$$

so that the normal derivative to the inclusion boundary is then given by:

$$\frac{\partial h_l^i}{\partial \hat{\boldsymbol{n}}} = \left(\frac{1}{\varepsilon^{\frac{1}{2}}} \frac{\partial}{\partial \rho_i} \hat{\boldsymbol{\rho}}_i + \frac{1}{\varepsilon^{\frac{1}{2}} \rho_i} \frac{\partial}{\partial \phi_i} \hat{\boldsymbol{\phi}}_i \right) h_l^i \cdot \hat{\boldsymbol{n}}. \tag{3.56}$$

Therefore, the continuity conditions on the height of the membrane (3.19) and its normal derivative with respect to the inclusion boundary (3.20), evaluated at the inclusion boundary $\rho_i = \rho_b^i$ according to (3.52), become:

$$h_l^i\big|_{\rho_i=\rho_b^i} = \gamma_i + \varepsilon^{\frac{1}{2}} \beta_i^{(1)} \cos\phi_i + \varepsilon^{\frac{1}{2}} \beta_i^{(2)} \sin\phi_i + O\left(\varepsilon^{\frac{3}{2}}\right), \tag{3.57}$$

$$\left.\frac{\partial h_l^i}{\partial \hat{\boldsymbol{n}}}\right|_{\rho_i=\rho_b^i} = \frac{\alpha_i^{(0)}}{\varepsilon^{\frac{1}{2}}} + \beta_i^{(1)} \cos\phi_i + \beta_i^{(2)} \sin\phi_i + O(\varepsilon), \tag{3.58}$$

respectively. Note that we have an extra factor of $\varepsilon^{-1/2}$ on the right hand side of (3.58) given that we have not explicitly computed the derivative on the left hand side in terms of the inner variables (ρ_i, ϕ_i). As a result, the $\varepsilon^{1/2}$ factors do not cancel as they did previously in Section 3.2.

We now consider the additional boundary conditions pertaining to the balance of force and moment at the inclusion boundary (i.e. (3.23)-(3.25)). For non-circular boundaries, we must now consider an additional multiplicative factor in the integral due to the shape of the contour. To account for this factor, we denote the position vector of the boundary in the x-y plane by $\boldsymbol{p}$ and parametrize this vector in terms of the angular variable ϕ_i taken from the positive x-axis:

$$\boldsymbol{p} = \left((1 - \varepsilon\omega_i \cos(2\phi_i - 2\psi_i)) \cos\phi_i, (1 - \varepsilon\omega_i \cos(2\phi_i - 2\psi_i)) \sin\phi_i \right). \tag{3.59}$$

We calculate the derivative of the position vector $\boldsymbol{p}$ with respect to ϕ_i and find the resultant magnitude to obtain the dilation of the contour arclength:

$$\left| \frac{\partial \boldsymbol{p}}{\partial \phi_i} \right| = 1 - \varepsilon\omega_i \cos(2\phi_i - 2\psi_i) + O\left(\varepsilon^2\right). \tag{3.60}$$

Therefore, the balance of transverse forces along the z-axis, and moments around the y-axis and x-axis respectively along the inclusion boundary are given by:

$$0 = \int_0^{2\pi} \frac{\partial}{\partial \hat{\boldsymbol{n}}} \left(\nabla^2 h \right) \Big|_{\rho_i=\rho_b^i} \left| \frac{\partial \boldsymbol{p}}{\partial \phi_i} \right| \mathrm{d}\phi_i, \tag{3.61}$$

$$0 = \int_0^{2\pi} \left[\rho_i \cos\phi_i \frac{\partial}{\partial \hat{\boldsymbol{n}}} \left(\nabla^2 h \right) - \nabla^2 h \frac{\partial}{\partial \hat{\boldsymbol{n}}} \left(\rho_i \cos\phi_i \right) \right] \Big|_{\rho_i=\rho_b^i} \left| \frac{\partial \boldsymbol{p}}{\partial \phi_i} \right| \mathrm{d}\phi_i, \tag{3.62}$$

$$0 = \int_0^{2\pi} \left[\rho_i \sin\phi_i \frac{\partial}{\partial \hat{\boldsymbol{n}}} \left(\nabla^2 h \right) - \nabla^2 h \frac{\partial}{\partial \hat{\boldsymbol{n}}} \left(\rho_i \sin\phi_i \right) \right] \Big|_{\rho_i=\rho_b^i} \left| \frac{\partial \boldsymbol{p}}{\partial \phi_i} \right| \mathrm{d}\phi_i, \tag{3.63}$$

where the integrals are evaluated at the boundary ρ_b^i according to (3.52), with the normal derivative defined in (3.56), and the arclength dilation given by (3.60).

3.3.2 Derivation of interaction energy

The method to determine the interaction energy between the geometrically symmetry-breaking membrane inclusions is similar to that summarized in Section 3.1.1 and followed in Section 3.2. Therefore, we condense the forthcoming derivation and refer to details discussed in the previous section where appropriate.

We first determine the shape of the inner local solution by solving (3.13), which gives the same general solution as in (3.36). To impose the boundary conditions on the non-circular boundary and therefore determine the unknown integration constants $b_q \in \mathbb{R}$, we expand each coefficient as a perturbation series of the form:

$$b_q = b_q^{(0)} + \varepsilon^{\frac{1}{2}} b_q^{(1)} + \varepsilon b_q^{(2)} + O\left(\varepsilon^{\frac{3}{2}}\right), \tag{3.64}$$

where $b_q^{(j)} = O(1)$ for $j \in \{0, 1, 2\}$.

Enforcing (3.61)-(3.63), we find that $b_3 = b_6 = b_{62} = O(\varepsilon^2)$, whilst applying (3.57) and (3.58), with the expansion of the trigonometric terms $\cos(2\phi_1 - 2\psi_1)$ and $\sin(2\phi_1 - 2\psi_1)$ and matching the Fourier terms, we find that the layer shape close to the first inclusion is given by:

$$\begin{aligned} h_l^1 = b_0 + \left(\alpha_1^{(0)} - 2b_2\right) \ln \rho_1 + b_2 \rho_1^2 + \varepsilon^{\frac{1}{2}} \beta_1^{(1)} \rho_1 \cos\phi_1 \\ + \varepsilon^{\frac{1}{2}} \beta_1^{(2)} \rho_1 \sin\phi_1 + b_8 \rho_1^2 \cos 2\phi_1 + b_{82} \rho_1^2 \sin 2\phi_1 \\ - \left(2b_8 - 2\varepsilon\omega_1 b_2^{(0)} \cos 2\psi_1 - \frac{\varepsilon\omega_1 \alpha_1^{(0)}}{2} \cos 2\psi_1\right) \cos 2\phi_1 \\ - \left(2b_{82} - 2\varepsilon\omega_1 b_2^{(0)} \cos 2\psi_1 - \frac{\varepsilon\omega_1 \alpha_1^{(0)}}{2} \sin 2\psi_1\right) \sin 2\phi_1 \\ + \frac{\left(2b_8 - 4\varepsilon\omega_1 b_2^{(0)} \sin 2\psi_1 - \varepsilon\omega_1 \alpha_1^{(0)} \cos 2\psi_1\right) \cos 2\phi_1}{2\rho_1^2} \\ + \frac{\left(2b_{82} - 4\varepsilon\omega_1 b_2^{(0)} \sin 2\psi_1 - \varepsilon\omega_1 \alpha_1^{(0)} \sin 2\psi_1\right) \sin 2\phi_1}{2\rho_1^2}, \end{aligned} \tag{3.65}$$

where we have combined individual terms in the perturbation series of b_q to simplify the expression and $\gamma_1 = b_0 + b_2$, b_2, b_8, b_{82}, $\beta_1^{(1)}$, and $\beta_1^{(2)}$ are to be determined by asymptotic matching with the outer solution. Similar reasoning gives that the shape

close to the second inclusion is:

$$
\begin{aligned}
h_l^2 = \hat{b_0} + \left(\alpha_2^{(0)} - 2\hat{b_2}\right)\ln\rho_2 + \hat{b_2}\rho_2^2 + \varepsilon^{\frac{1}{2}}\beta_2^{(1)}\rho_2\cos\phi_2 \\
+ \varepsilon^{\frac{1}{2}}\beta_2^{(2)}\rho_2\sin\phi_2 + \hat{b_8}\rho_2^2\cos 2\phi_2 + \hat{b_{82}}\rho_2^2\sin 2\phi_2 \\
- \left(2\hat{b_8} - 2\varepsilon\omega_2\hat{b_2^{(0)}}\cos 2\psi_2 - \frac{\varepsilon\omega_2\alpha_2^{(0)}}{2}\cos 2\psi_2\right)\cos 2\phi_2 \\
- \left(2\hat{b_{82}} - 2\varepsilon\omega_2\hat{b_2^{(0)}}\cos 2\psi_2 - \frac{\varepsilon\omega_2\alpha_2^{(0)}}{2}\sin 2\psi_2\right)\sin 2\phi_2 \\
+ \frac{\left(2\hat{b_8} - 4\varepsilon\omega_2\hat{b_2^{(0)}}\sin 2\psi_2 - \varepsilon\omega_2\alpha_2^{(0)}\cos 2\psi_2\right)\cos 2\phi_2}{2\rho_2^2} \\
+ \frac{\left(2\hat{b_{82}} - 4\varepsilon\omega_2\hat{b_2^{(0)}}\sin 2\psi_2 - \varepsilon\omega_2\alpha_2^{(0)}\sin 2\psi_2\right)\sin 2\phi_2}{2\rho_2^2},
\end{aligned}
\tag{3.66}
$$

where the unknown constants are $\gamma_2 = \hat{b_0} + \hat{b_2}$, and $\hat{b_0}$, $\hat{b_2}$, $\hat{b_8}$, $\hat{b_{82}}$, $\beta_2^{(1)}$, and $\beta_2^{(2)}$.

Given that the leading order layer solutions (3.65) and (3.66) are logarithmic, the leading order outer membrane solution h_m is (3.39). Therefore, the asymptotic matching would yield the same results for the unknown coefficients; the most relevant of these being (3.43) and (3.47) and that $b_2 = \hat{b_2} = O\left(\varepsilon^{\frac{3}{2}}\right)$.

We can now calculate the interaction energy between the two non-circular inclusions. We determine the Laplacians of the inner layer solutions using (3.65) and (3.66) and our results from asymptotic matching to find:

$$
\nabla_l^2 h_l^1 = -\frac{4\alpha_2^{(0)}\cos 2\phi_1}{R^2\rho_1^2} - \frac{2\omega_1\alpha_1^{(0)}\cos\left(2\phi_1 - 2\psi_1\right)}{\rho_1^2} + O\left(\varepsilon^{\frac{1}{2}}\right), \tag{3.67}
$$

$$
\nabla_l^2 h_l^2 = -\frac{4\alpha_1^{(0)}\cos 2\phi_2}{R^2\rho_2^2} - \frac{2\omega_2\alpha_2^{(0)}\cos\left(2\phi_2 - 2\psi_2\right)}{\rho_2^2} + O\left(\varepsilon^{\frac{1}{2}}\right), \tag{3.68}
$$

where ∇_l^2 is the inner Laplacian in (ρ_i, ϕ_i) coordinates accounting for the factor of ε in transforming from the outer variables to inner variables according to (3.26) and (3.27). As in Section 3.2, the Laplacian of the outer membrane h_m as found in (3.39) is $O(\varepsilon)$ and is therefore comparatively negligible in the limit of $\varepsilon \ll 1$.

Therefore, to calculate the interaction energy, we integrate (3.50) with the inner

layer shape Laplacians found in (3.67) and (3.68) to obtain:

$$V\left(R,\psi_1,\psi_2\right)=\kappa\pi\varepsilon\left[\left(\omega_1\alpha_1^{(0)}\right)^2+\left(\omega_2\alpha_2^{(0)}\right)^2\right.$$
$$+\frac{4}{R^2}\left(\omega_1\alpha_1^{(0)}\alpha_2^{(0)}\cos 2\psi_1+\omega_2\alpha_2^{(0)}\alpha_1^{(0)}\cos 2\psi_2\right)$$
$$\left.+\frac{4}{R^4}\left(\left(\alpha_1^{(0)}\right)^2+\left(\alpha_2^{(0)}\right)^2\right)\right]. \quad (3.69)$$

3.4 Remarks on the interaction laws

Some comments are in order regarding the two main results of the present work; that is, the laws describing the interactions of inclusions which break symmetry in either their contact angle (3.51) or their boundary geometry (3.69). First, upon comparison, we note that these two laws are equivalent when $\alpha_i^{(2)}=\omega_i\alpha_i^{(0)}$. The quadrupole opening angle $\alpha_i^{(2)}$ for a perfectly circular inclusion is equivalent to the coupling of the constant opening angle $\alpha_i^{(0)}$ with the parameter describing the geometry deviation of the inclusion ω_i. This result suggests that the effects of these two symmetry-breaking mechanisms are the same in the regime of deforming approximately flat fluid membranes. Second, we note that the quadrupole symmetry-breaking mode (i.e. invariant under a rotation of an individual inclusion by π) is the dominant contribution to the interaction energy. This result follows from asymptotic matching, which gives that the first Fourier mode would not contribute to the energy and the third order modes and higher would be $O\left(\varepsilon^{\frac{3}{2}}\right)$ if they were included at the same order of ε as the second Fourier mode in (3.28). Third, we note that (3.51) and (3.69) reduce to the original law describing the repulsion of two isotropic inclusions on the fourth power of the inverse separation [41, 101, 31]. This result follows for the case where there is no symmetry-breaking mechanism (i.e. $\alpha_i^{(2)}=\omega_i=0$) and by further noting that the area of a single inclusion is $\pi\varepsilon$, given that its radius is $\varepsilon^{\frac{1}{2}}$.

There are two symmetry-breaking terms in (3.51) and (3.69), one of which depends on the inverse separation between the inclusions squared and the orientation of the anisotropic deformation exerted by the inclusion on the surrounding membrane, whilst the other is a constant with respect to these variables and can therefore be rescaled out of the interaction energy. The former term implies that the symmetry-breaking of a given inclusion interacts with the isotropic opening angle imposed by the other inclusion. We further study the effects of this symmetry-breaking in the interaction between identical inclusions.

3.4.1 Two identical inclusions

Suppose that the two inclusions are identical (i.e. $\alpha_1^{(0)} = \alpha_2^{(0)} = \alpha_0$ and $\alpha_1^{(2)} = \alpha_2^{(2)} = \alpha_2$). We define a new rescaled interaction energy:

$$V_{sc} = \frac{1}{4\alpha_0\alpha_2}\left(\frac{V}{\kappa\pi\varepsilon} - 2\alpha_2^2\right), \tag{3.70}$$

so that (3.51) becomes:

$$V_{sc} = \frac{1}{R^2}\left(\cos 2\psi_1 + \cos 2\psi_2\right) + \frac{2\sigma}{R^4}, \tag{3.71}$$

where $\sigma = \alpha_0/\alpha_2$ is the ratio of isotropic to symmetry-breaking effects.

We calculate the torque τ_i exerted on the ith inclusion around the z-axis as a result of the underlying membrane curvature by taking the negative partial derivative of (3.71) with respect to ψ_i:

$$\tau_i = \frac{2\sin 2\psi_i}{R^2}. \tag{3.72}$$

We comment that the inclusions are in rotational equilibrium for $\psi_1 = n\pi/2$. However, this does not necessarily correspond to the lowest energy state. There are two possible equilibrium configurations: the higher energy state whereby $\psi_i = n\pi$ and the lower energy state where $\psi_i = \left(n + \frac{1}{2}\right)\pi$ for $n \in \mathbb{Z}$. If both inclusions have orientation angles ψ_i that satisfy this former condition, then they will repel at a longer range than the isotropic case, whilst if they both satisfy the latter condition, then the inclusions will attract. For non-circular inclusions embedded in a fluid membrane, attraction will occur when their semi-major axes are aligned in an "end-to-end" configuration. A similar result was obtained by supposing that the inclusions were rods forcing a non-zero curvature along one of its principal axes [69], and this phenomenon has also been observed in large scale molecular dynamics simulations [87].

We consider the effective force F exerted between the inclusions as a result of the underlying membrane shape. By taking the negative partial derivative of (3.71) with respect to R, we find:

$$F = \frac{2}{R^3}\left(\cos 2\psi_1 + \cos 2\psi_2\right) + \frac{8\sigma}{R^5}, \tag{3.73}$$

whilst the equilibrium distance R_{eqm} necessary for the effective force to vanish is:

$$R_{eqm} = \sqrt{\frac{-4\sigma}{\cos 2\psi_1 + \cos 2\psi_2}}. \tag{3.74}$$

Imposing that the inclusions must also be in rotational equilibrium, we note that R_{eqm} is only real if the orientation angles $\psi_1 = \psi_2 = \left(n + \frac{1}{2}\right)\pi$, which gives the lower

energy state. In this case, the symmetry-breaking attraction balances the isotropic repulsion to give a natural aggregation distance:

$$R_{eqm} = \sqrt{2\sigma}, \tag{3.75}$$

which is $O(1)$ as per our previous assumptions in Sections 3.1 and 4.1, given that $\alpha_0 = \alpha_2 = O(1)$. We comment that in the limit whereby the isotropic effects dominate the symmetry-breaking effects $\sigma \to \infty$, the aggregation distance R_{eqm} of the two inclusions goes to infinity.

3.4.2 Inclusion-generated curvature field

We continue with the electrostatics and magnetism analogy and consider the curvature-mediated interaction field generated by a symmetry-breaking inclusion. In electrostatics, one would probe the electric field generated by a charge distribution by taking a single point charge and determining the position dependent potential. For our case, we determine the curvature-mediated potential by fixing the position of the first inclusion's center to be at the origin whilst the position of the second inclusion remains free (i.e. has position at (x, y)). We further take both inclusion orientations to be fixed.

We first generalize the derived interaction laws, given that they were derived under the assumption that the inclusions were separated along the x-axis. We suppose the inclusions are separated along a line connecting the center of the first inclusion to the second which makes an angle θ_{12} with respect to the positive x-axis. We include this rotation by transforming the orientation inclusion angles $\psi_1 \to \psi_1 - \theta_{12}$ and $\psi_2 \to \psi_2 - \theta_{12}$. Without loss of generality, we take the rotated inclusion orientations to vanish $\psi_1 = \psi_2 = 0$ so that (3.71) becomes:

$$V_{sc} = \frac{2}{R^2}\left(\cos^2\theta_{12} - \sin^2\theta_{12}\right) + \frac{2\sigma}{R^4}. \tag{3.76}$$

Lastly, by noting that the separation of the inclusions' centers in the x-y plane is related to R and θ_{12} by $x = R\cos\theta_{12}$ and $y = R\sin\theta_{12}$, we obtain that the spatial interaction potential is given by:

$$V_{sc} = \frac{2\left(x^2 - y^2 + \sigma\right)}{\left(x^2 + y^2\right)^2}, \tag{3.77}$$

with associated curvature-mediated interaction field $\boldsymbol{C} = -\nabla V_{sc}$:

$$\boldsymbol{C} = \left(\frac{4x\left(x^2 - 3y^2 + 2\sigma\right)}{\left(x^2 + y^2\right)^3}, \frac{4y\left(3x^2 - y^2 + 2\sigma\right)}{\left(x^2 + y^2\right)^3}\right). \tag{3.78}$$

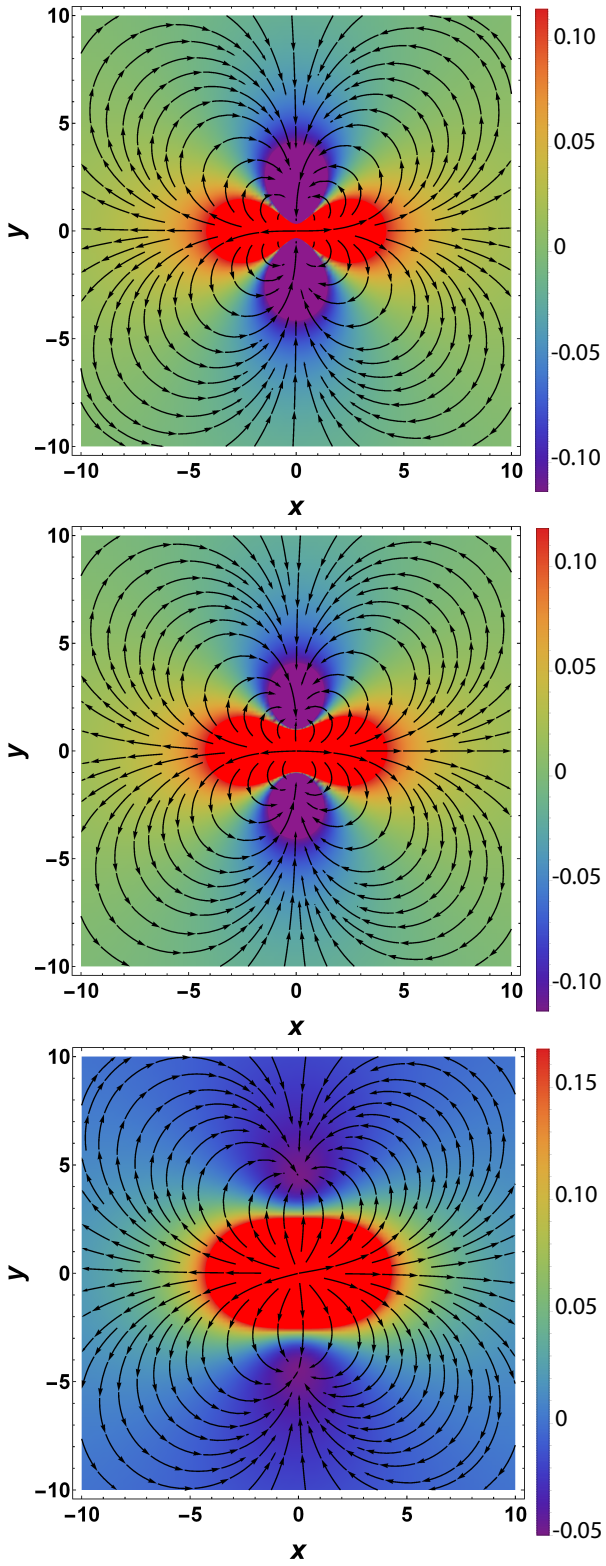

Figure 3.4: The interaction potential (3.77) (shown in color) and the curvature-mediated interaction field (3.78) (shown with black arrows) generated by an inclusion fixed at the origin with orientation angle $\psi_1 = 0$ and probe angle $\psi_2 = 0$. The ratio of isotropic to symmetry-breaking effects is top: $\sigma = 0.1$; middle: $\sigma = 1$; bottom: $\sigma = 10$.

We plot the spatial potential (3.77) and the corresponding interaction field (3.78) in Fig. 3.4 for the ratio of isotropic to symmetry-breaking effects $\sigma = \{0.1, 1, 10\}$ and make some remarks. We note that the interaction field closely resembles that of a magnetic quadrupole, with the red and purple regions corresponding to the north and south poles respectively, and with the inclusion generating the same field under a rotation of π. If the inclusion orientations were fixed and horizontal $\psi_1 = \psi_2 = 0$ and the first inclusion was fixed but the second inclusion was free to move, then the second inclusion would aggregate along the y-axis at a distance satisfying (3.75) (denoted by the purple regions of potential minima). As isotropic effects further dominate (i.e. σ increases), this aggregation distance increases and the curvature-mediated interaction field connecting the "north" and "south" poles traces out wider arcs.

3.5 Chapter summary

In the present work, we studied the curvature-mediated interactions between symmetry-breaking inclusions which were embedded on an approximately flat geometry in the regime where purely bending energies of the fluid membrane were considered. We studied two different symmetry-breaking mechanisms: one where the inclusion is perfectly circular in the plane but with a varying contact angle with the surrounding membrane, and the other where the inclusion is non-circular but imposed a constant contact angle around its boundary. In both cases, the symmetry-breaking effect was invariant under a rotation of an individual inclusion by π.

Using asymptotic analysis, we determined that these two means of symmetry-breaking resulted in equivalent interaction laws, whereby we obtained the original isotropic repulsion on the inverse separation to the fourth power as well as an additional orientation dependent interaction that varied on the inverse separation squared. We showed that the π reflection symmetry of anisotropic deformation was the dominant contribution to the interactions between inclusions and symmetry-breaking that was invariant under a rotation of 2π as well as angles smaller than π did not contribute to the leading order energy.

We studied the interaction of two identical inclusions and calculated the curvature-mediated torques around the z-axis and separation forces exerted on each inclusion. We found that there were two rotational equilibrium states: alignment of the orientation along the line of separation between the inclusions, which corresponded to the unstable high energy state, and orientations which were perpendicular to this, which corresponded to the stable low energy state. For two inclusions having the

latter orientations, curvature-mediated attraction was possible and would result in a natural equilibrium distance whereby the symmetry-breaking attraction would balance with the isotropic repulsion. This result could provide an explanation as to how membrane inclusions can globally aggregate by membrane-mediated effects to a length-scale whereby more direct interactions, such as van der Waals forces, may then take over.

We calculated the interaction potential and the corresponding curvature-mediated interaction field generated by a single inclusion. For the symmetry-breaking properties studied, we found that such inclusions resembled a quadrupole seen in electrostatics or magnetism. Given the result that membrane-mediated aggregation is possible along with the quadrupole interaction nature of the inclusions, a natural question to pursue is the types of equilibrium configurations that can form along with their stability. Furthermore, it is unclear how large numbers of inclusions will dynamically self-assemble. We study these questions more closely in Chapter 4.

Chapter 4

Self-assembled aggregates: Shapes and properties

Based on the interaction law governing the curvature-mediated interplay between symmetry-breaking inclusions and the underlying fluid membrane shape that was derived in Chapter 3, we explore the self-assembled aggregates that these inclusions form and their corresponding macroscopic properties. Chapter 4 is organized as follows: In Section 4.1, we generalize the interaction law found in Chapter 3 to consider an arbitrary number of symmetry-breaking membrane inclusions and we derive a model to describe the dynamic aggregation of these objects. In Section 4.2 and 4.3, we consider the energy and stability of simple configurations; namely, of lines and polygons. In Section 4.4, drawing on analogies to classical elastica, we analytically determine the collective elastic behavior of the aggregate both under bending and stretching deformations. Given the focus on simplified shapes, in Section 4.5, we simulate a system of 1000 inclusions with initially random positions and orientations and show some of the complex transient aggregate shapes that may assemble. We summarize and conclude our results in Section 4.6.

4.1 Preliminary framework

4.1.1 Interaction law for N inclusions

We summarize the curvature-mediated interaction law between two symmetry-breaking inclusions derived in Chapter 3 here. Suppose we have two anisotropic inclusions of radius $\sqrt{\varepsilon}$ embedded in an approximately flat fluid membrane which is parametrized by the Cartesian coordinates (x, y). Suppose that the symmetry-breaking deformations induced by a single inclusion are invariant under a rotation by π and the centers of the inclusions are separated by a distance R along the x-axis. For two inclusions which

imposed an isotropic "monopole" contact angle $\alpha_i^{(0)}$ and anisotropic "quadrupole" contact angle $\alpha_i^{(2)}$, that is dependent on an orientation angle ψ_i with respect to the positive x-axis, with the surrounding fluid membrane, the interaction energy was given by:

$$V\left(R,\psi_1,\psi_2\right)=\kappa\pi\varepsilon\left[\left(\alpha_1^{(2)}\right)^2+\left(\alpha_2^{(2)}\right)^2 + \frac{4}{R^2}\left(\alpha_1^{(2)}\alpha_2^{(0)}\cos 2\psi_1+\alpha_2^{(2)}\alpha_1^{(0)}\cos 2\psi_2\right) + \frac{4}{R^4}\left(\left(\alpha_1^{(0)}\right)^2+\left(\alpha_2^{(0)}\right)^2\right)\right]. \quad (4.1)$$

We previously found that the dominant contributions to the interaction energy between symmetry-breaking inclusions came from their respective inner layer shapes. This suggests that the interaction law is a result of local additions to the fluid membrane shape, which therefore implies that the curvature-mediated interaction of such inclusions is pairwise for the case of approximately flat geometries. As a consequence, one can extend (4.1) to study the interactions of an arbitrary number of identically sized inclusions N by adding the energy contribution of each subsequent inclusion. Doing so gives:

$$V=\kappa\pi\varepsilon\sum_{i=1}^{N}\left\{\left(\alpha_i^{(2)}\right)^2+4\sum_{j\neq i}^{N}\frac{\alpha_j^{(0)}\alpha_i^{(2)}\cos 2\psi_i}{R_{ij}^2}+\frac{\left(\alpha_j^{(0)}\right)^2}{R_{ij}^4}\right\}, \quad (4.2)$$

where R_{ij} is the separation distance between the ith and jth inclusion.

However, (4.1) was derived assuming that the inclusions were separated horizontally from each other along the x-axis. More generally, suppose there is a line from the ith inclusion to the jth inclusion which makes an angle of θ_{ij} with the positive x-axis (see Fig. 4.1). We rotate the system in the plane by an angle of θ_{ij} by transforming the symmetry-breaking orientation $\psi_i \to \psi_i - \theta_{ij}$, so that the interaction law between inclusions separated along an arbitrary orientation is given by:

$$V=\kappa\pi\varepsilon\sum_{i=1}^{N}\left\{\left(\alpha_i^{(2)}\right)^2 + 4\sum_{j\neq i}^{N}\frac{\alpha_j^{(0)}\alpha_i^{(2)}R_{ij}^2\left[2\cos^2\left(\psi_i-\theta_{ij}\right)-1\right]+\left(\alpha_j^{(0)}\right)^2}{R_{ij}^4}\right\}, \quad (4.3)$$

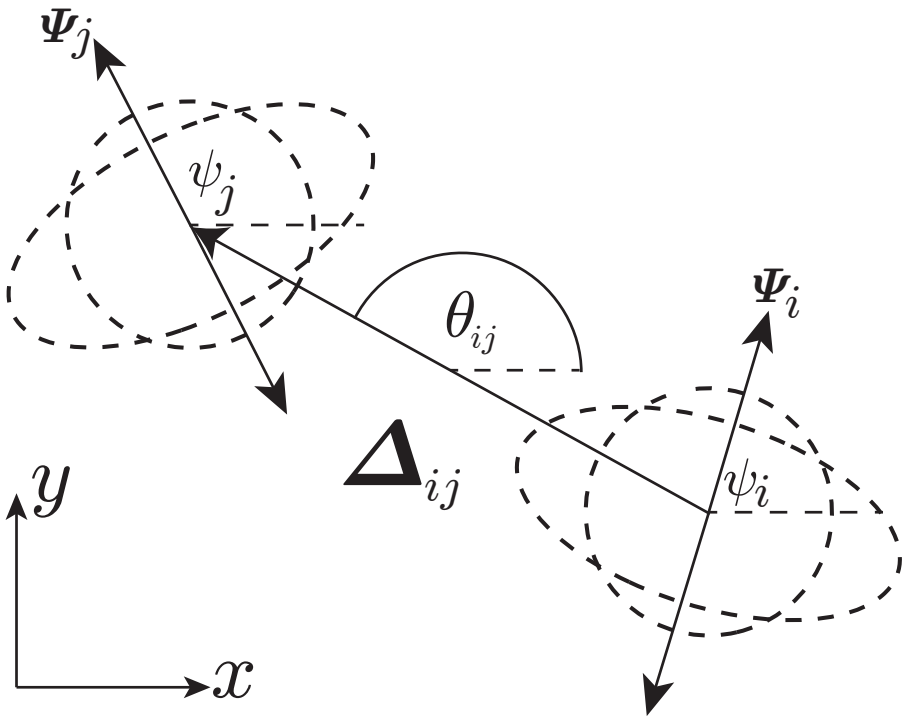

Figure 4.1: A schematic diagram showing the interaction between symmetry-breaking inclusions (shown as either the dotted circular or dotted non-circular lines respectively) which are separated by an arbitrary orientation. The vector $\boldsymbol{\Psi}_i$ (i.e (4.4)) encodes information regarding the inclusion's symmetry-breaking orientation with respect to the positive x-axis, ψ_i, whilst the separation vector from the ith inclusion to the jth inclusion $\boldsymbol{\Delta}_{ij}$ (i.e. (4.5)) includes information about the distance and the separation angle taken from the positive x-axis, θ_{ij}. Given that the deformations exerted by the inclusions are invariant under a rotation of π, the orientations are represented as double-headed arrows.

where we have used the double angle formula $\cos 2\eta = 2\cos^2\eta - 1$. We comment that the above expression is invariant if we were to instead consider a line from the jth inclusion to the ith inclusion given that $R_{ij} = R_{ji}$ and $\theta_{ij} = \theta_{ji} + \pi$.

We introduce two vectors $\mathbf{\Psi}_i$ and $\mathbf{\Delta}_{ij}$ which encode the symmetry-breaking orientation of the ith inclusion with respect to the positive x-axis and the separation vector pointing from the ith inclusion to the jth inclusion (see Fig. 4.1). We define these two vectors as:

$$\mathbf{\Psi}_i = (\cos\psi_i, \sin\psi_i)\,, \tag{4.4}$$

$$\mathbf{\Delta}_{ij} = (R_{ij}\cos\theta_{ij}, R_{ij}\sin\theta_{ij})\,, \tag{4.5}$$

which reduces the interaction energy of N inclusions to the form:

$$V = \kappa\pi \left\{ \sum_{i=1}^{N} \left(\alpha_i^{(2)}\right)^2 + 4\varepsilon \sum_{j\neq i}^{N} \frac{\alpha_j^{(0)}\alpha_i^{(2)}\left(2\left(\mathbf{\Psi}_i\cdot\mathbf{\Delta}_{ij}\right)^2 - \mathbf{\Delta}_{ij}^2\right) + \left(\alpha_j^{(0)}\right)^2}{\left|\mathbf{\Delta}_{ij}\right|^4} \right\}. \tag{4.6}$$

We note three contributions to the total energy of the system given by (4.6): First, there is a constant energy offset due to the anisotropic deformation from every inclusion which can be rescaled out of the energy. Second, for the ith inclusion, there is a sum taken over all other inclusions and how they interact with the symmetry-breaking deformation it exerts, given the explicit dependence on the magnitude of its quadrupole opening angle $\alpha_i^{(2)}$ and the ith inclusion's orientation ψ_i encoded in $\mathbf{\Psi}_i$. We further note this term has a minimum when the separation vector is perpendicular to the orientation (i.e. $\mathbf{\Psi}_i\cdot\mathbf{\Delta}_{ij} = 0$), corresponding to the attraction between inclusions on the inverse separation length squared, whilst this term attains a maximum for separations parallel to the inclusion orientation (i.e. $\mathbf{\Psi}_i\cdot\mathbf{\Delta}_{ij} = |\mathbf{\Delta}_{ij}|$), corresponding to the repulsion between inclusions on the inverse separation length squared. Lastly, there is an orientation independent repulsion term from the isotropic deformation imposed by all other inclusions $\alpha_j^{(0)}$.

We suppose that the inclusions are identical so that $\alpha_j^{(0)} = \alpha_0$ and $\alpha_j^{(2)} = \alpha_2$ for $j \in \{1, ..., N\}$. By rescaling the energy:

$$\frac{V - N\kappa\pi\alpha_2^2}{4\kappa\pi\varepsilon\alpha_0\alpha_2} \to V, \tag{4.7}$$

we find that (4.6) reduces to:

$$V = \sum_{i=1}^{N} \sum_{j \neq i}^{N} \frac{2\left(\boldsymbol{\Psi}_i \cdot \boldsymbol{\Delta}_{ij}\right)^2 - \boldsymbol{\Delta}_{ij}^2 + \sigma}{\left|\Delta_{ij}\right|^4}, \tag{4.8}$$

where $\sigma = \alpha_0/\alpha_2$ is the ratio of isotropic to anisotropic deformations exerted by the membrane inclusion.

4.1.2 Dynamic gradient-flow model

We derive a time-dependent model for the movement of inclusions embedded in a lipid bilayer. Given that movement within the membrane plane is usually described as a viscous fluid flow [78, 73], we assume the dynamics of the membrane inclusions is a dissipative process. We model this process as a gradient flow, so that the time-dependent equations describing the kth inclusion's center $\boldsymbol{r}_k = (x_k, y_k)$ and rotational motion ψ_k is:

$$b\frac{\mathrm{d}\boldsymbol{r}_k}{\mathrm{d}t} = -\frac{\partial V}{\partial \boldsymbol{r}_k}, \tag{4.9}$$

$$\rho\frac{\mathrm{d}\psi_k}{\mathrm{d}t} = -\frac{\partial V}{\partial \psi_k}, \tag{4.10}$$

where b and ρ are the phenomenological friction coefficients of translational and rotational motion.

Determining the partial derivative of (4.8) with respect to the general variable governing the motion of the kth inclusion p_k, we note that all terms in the double series would vanish except for two particular instances; namely, when $i = k$ or $j = k$. In this case, we find:

$$\frac{\partial V}{\partial p_k} = \sum_{j \neq k}^{N} \frac{\partial}{\partial p_k}\left(\frac{2\left(\boldsymbol{\Psi}_k \cdot \boldsymbol{\Delta}_{kj}\right)^2 - \boldsymbol{\Delta}_{kj}^2 + \sigma}{\left|\boldsymbol{\Delta}_{kj}\right|^4}\right) + \sum_{i \neq k}^{N} \frac{\partial}{\partial p_k}\left(\frac{2\left(\boldsymbol{\Psi}_j \cdot \boldsymbol{\Delta}_{jk}\right)^2 - \boldsymbol{\Delta}_{jk}^2 + \sigma}{\left|\boldsymbol{\Delta}_{jk}\right|^4}\right). \tag{4.11}$$

Noting that i is a summation index, one can replace this with j and add the two sums together. Furthermore, since $\boldsymbol{\Delta}_{ij} = -\boldsymbol{\Delta}_{ji}$, which follows from $R_{ij} = R_{ji}$ and $\theta_{ij} = \theta_{ji} + \pi$, we find the reduction:

$$\frac{\partial V}{\partial p_k} = 2\sum_{j \neq k}^{N} \frac{\partial}{\partial p_k}\left(\frac{\left(\boldsymbol{\Psi}_k \cdot \boldsymbol{\Delta}_{jk}\right)^2 + \left(\boldsymbol{\Psi}_j \cdot \boldsymbol{\Delta}_{jk}\right)^2 - \boldsymbol{\Delta}_{jk}^2 + \sigma}{\left|\boldsymbol{\Delta}_{jk}\right|^4}\right). \tag{4.12}$$

Therefore, by noting that $\boldsymbol{\Delta}_{ij} = \boldsymbol{r}_j - \boldsymbol{r}_i$ and its derivative with respect to the vector $\boldsymbol{r}_j$ is given by the 2×2 identity matrix, we obtain the translational equation of motion for the kth inclusion:

$$b\frac{\mathrm{d}\boldsymbol{r}_k}{\mathrm{d}t} = -4\sum_{j\neq k}^{N}\left\{\frac{\left(\boldsymbol{\Psi}_k\cdot\boldsymbol{\Delta}_{jk}\right)\boldsymbol{\Psi}_k + \left(\boldsymbol{\Psi}_j\cdot\boldsymbol{\Delta}_{jk}\right)\boldsymbol{\Psi}_j - \boldsymbol{\Delta}_{jk}}{\left|\boldsymbol{\Delta}_{jk}\right|^4} - \frac{2\left[\left(\boldsymbol{\Psi}_k\cdot\boldsymbol{\Delta}_{jk}\right)^2 + \left(\boldsymbol{\Psi}_j\cdot\boldsymbol{\Delta}_{jk}\right)^2 - \boldsymbol{\Delta}_{jk}^2 + \sigma\right]\boldsymbol{\Delta}_{jk}}{\left|\boldsymbol{\Delta}_{jk}\right|^6}\right\}, \quad (4.13)$$

and the rotational equation of motion:

$$\rho\frac{\mathrm{d}\psi_k}{\mathrm{d}t} = -4\sum_{j\neq k}^{N}\frac{\left(\boldsymbol{\Psi}_k\cdot\boldsymbol{\Delta}_{jk}\right)\left(\boldsymbol{\Psi}_k^{\perp}\cdot\boldsymbol{\Delta}_{jk}\right)}{\left|\boldsymbol{\Delta}_{jk}\right|^4}, \quad (4.14)$$

where $\boldsymbol{\Psi}_k^{\perp} = \partial\boldsymbol{\Psi}_k/\partial\psi_k = (-\sin\psi_k, \cos\psi_k)$ is a unit vector perpendicular to the orientation vector $\boldsymbol{\Psi}_k$.

4.2 Linear aggregates

4.2.1 Energy of a single infinite line

Suppose we have an infinite straight line of identical symmetry-breaking inclusions with each individual inclusion separated by a constant distance d which will be determined. Note that for a finite line, the distance between each inclusion would be different. Due to attractive curvature-mediated forces, the number of inclusions would be denser at the center of the line with the number becoming sparser at the ends. We take the infinite line to extend along the y-axis with each inclusion orientation given by $\psi_i = 0$. In this case, (4.4) and (4.5) become:

$$\boldsymbol{\Psi}_i = (1, 0)\,, \quad (4.15)$$

$$\boldsymbol{\Delta}_{ij} = (0, d\,(j-i))\,. \quad (4.16)$$

We calculate the energy contribution of a single inclusion which, without loss of generality, we choose to be the 0th inclusion, given that, in the infinite line, each inclusion would contribute the same energy. This quantity is equivalently the energy density of the line, which we denote μ_{line}. According to (4.8), this quantity is:

$$\mu_{line} = 2\sum_{j=1}^{\infty} -\frac{1}{d^2 j^2} + \frac{\sigma}{d^4 j^4}, \quad (4.17)$$

where the factor of 2 arises from noting that the total contributions above the 0th inclusion are the same as the total contributions below it.

Evaluating the infinite sum using the definition of the Riemann zeta function, we obtain:

$$\mu_{line} = -\frac{\pi^2}{3d^2} + \frac{\sigma\pi^4}{45d^4}, \tag{4.18}$$

and, furthermore, by minimizing the energy density with respect to d, we find that the equilibrium separation d_{eqm} between individual inclusions on the infinite line is:

$$d_{eqm} = \sqrt{\frac{2\sigma\pi^2}{15}}. \tag{4.19}$$

As with the previous result in Chapter 3, where it was found that the equilibrium distance between two inclusions was $\sqrt{2\sigma}$, there is no explicit dependence of the equilibrium distance on the mechanics of the underlying fluid membrane and the individual size of an inclusion. However, both equilibrium distances have a similar dependence on the ratio of isotropic to anisotropic deformations exerted by the inclusion σ, suggesting both separations will tend to infinity as the isotropic effects increasingly dominate. Furthermore, d_{eqm} is smaller than for the case of two inclusions. The physical reasoning for this is that as further inclusions are added, there are more curvature-mediated attractive forces which aggregate the inclusions closer together.

4.2.2 Stability of a single line

We numerically show the robustness of a single linear aggregate under perturbations to the positions and orientation of individual inclusions which comprise it. As a proxy to simulating an infinite line, we consider a large finite segment consisting of 200 inclusions and focus on a middle subset of this segment. This measure is taken to ensure that there are no spurious effects which may arise at the ends of the aggregate. We numerically solve (4.13) and (4.14) using the parameters $\sigma = b = \rho = 1$ which, in this case, gives that the linear aggregate has a length of approximately 230. The initial x positions of the inclusions are taken to be in the range $[-2, 2]$ whilst the y positions are governed by d_{eqm} as calculated in (4.19). The initial inclusion orientations are in the range $[-\pi/2, \pi/2]$. We plot one realization of this system in Fig. 4.2 for times $t = \{0, 1, 10, 1000\}$ and make some remarks.

Despite the system initializing with random positions and orientations, the inclusions quickly realign so that their separation vectors are perpendicular to their orientations. As a result, the linear aggregate reforms (see $t = 1$), however, due to

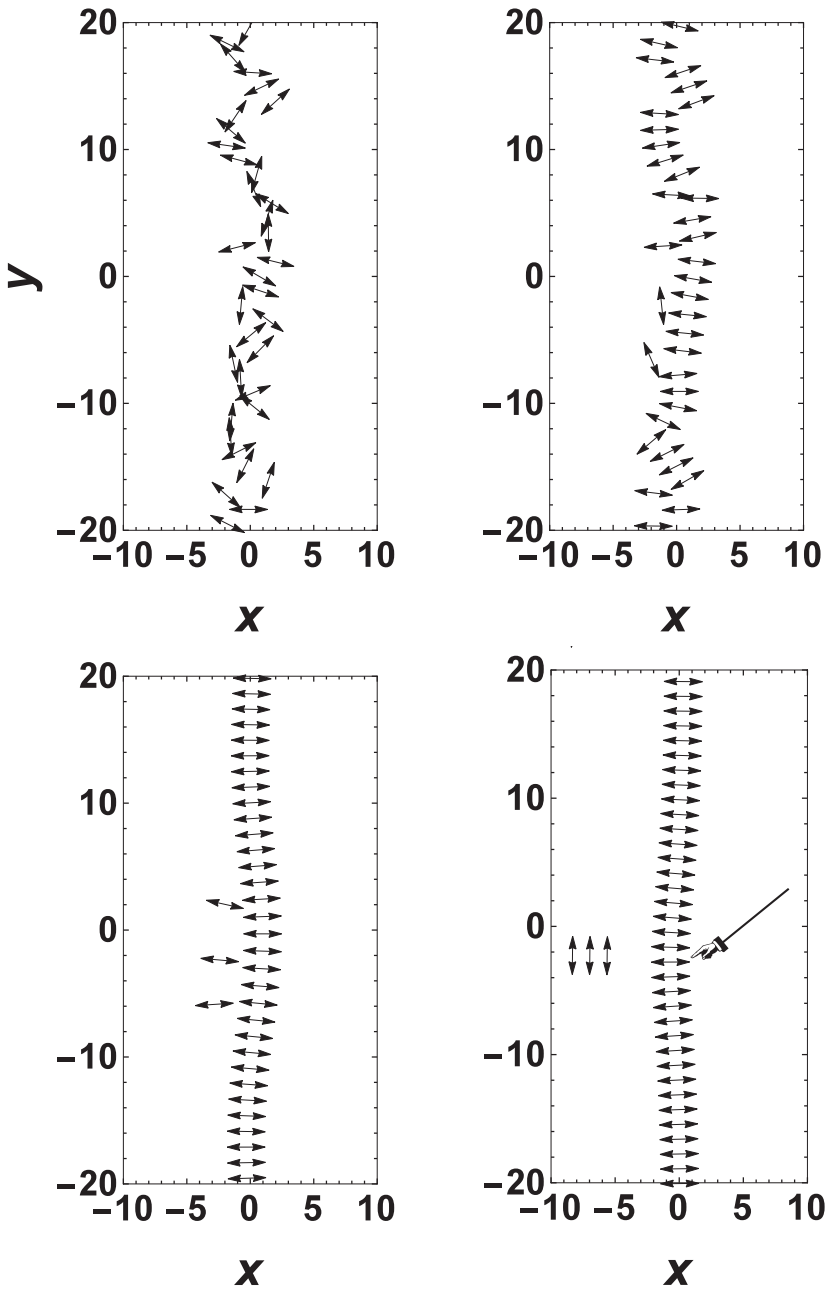

Figure 4.2: Simulation of a single perturbed line by numerically solving (4.13) and (4.14) for 200 symmetry-breaking inclusions (shown as black double-headed arrows). In particular, we show the middle subset of a large finite line to avoid additional effects from the ends of the aggregate. We use the parameters $\sigma = b = \rho = 1$ and impose the initial x-position as a random value in the range $[-2, 2]$ whilst the initial y-position is determined by d_{eqm} according to (4.19). In this case, the large line stretches from $y \in [-115, 115]$. The initial orientations of the inclusions are random values taken from $[-\pi/2, \pi/2]$. Times shown from left to right and top to bottom are $t = \{0, 1, 10, 1000\}$. Arrow shows the attracted bulge of the main line

the significant perturbation in initial position and orientation, some inclusions are ejected from the main line (see $t = 10$). These inclusions aggregate forming a smaller finite line and rotate due to a curvature-mediated torque exerted on it by the main line. After rotating, the main line appears to be attracted to the smaller finite line, resulting in the formation of a bulge towards it (see arrow). However, this bulge is counteracted by the straightening of the main line by means of the attraction between inclusions within it (see $t = 1000$). The simulation shows that linear aggregates which self-assemble as a consequence of curvature-mediated forces are stable.

4.2.3 Energy of two infinite lines

Suppose that there are now two infinite straight lines that extend along the y-axis and are separated by a distance L along the x-axis. As before, all inclusion orientations are given by $\psi_i = 0$. Similar configurations have been computationally shown for membrane shaping proteins which form spaced rings on cylindrical geometries [89] and have been further hypothesized as a mechanism for tubulation [84]. We would like to theoretically estimate the effective long range curvature-mediated repulsion between these rings.

We suppose that inclusions within a line are individually separated by d which depends on L. We calculate the energy of an individual inclusion or, equivalently, the energy density of the configuration μ_{double}. Without loss of generality, we consider the 0th inclusion in the first line, so that its separation vector between other inclusions within this same infinite line is given by (4.16), whilst the separation vector between other inclusions within the second line is given by:

$$\hat{\boldsymbol{\Delta}}_{0j} = (L, dj)\,, \tag{4.20}$$

for $j \in \mathbb{Z}$.

The energy density of the configuration includes two sums: one over the first infinite line involving the separation vector (4.16), and another over the second infinite line using the separation vector (4.20):

$$\mu_{double} = 2\sum_{j=1}^{\infty}\left[-\frac{1}{d^2j^2} + \frac{\sigma}{d^4j^4}\right] + \sum_{j=-\infty}^{\infty}\frac{L^2 - d^2j^2 + \sigma}{\left(L^2 + d^2j^2\right)^2}. \tag{4.21}$$

We remark that, with the addition of the second infinite line, there are additional energy contributions from the coupling of the orientation of the inclusion with inclusions within the opposing line.

Computing the sums, we find that:

$$\mu_{double} = -\frac{\pi^2}{3d^2} + \frac{\sigma\pi^4}{45d^4} + \frac{1}{2d^2L^3}\left(\frac{2\pi^2L^3 + \sigma\pi^2 L}{\sinh^2\left(\frac{L\pi}{d}\right)} + \frac{\sigma\pi d}{\tanh\left(\frac{L\pi}{d}\right)}\right), \tag{4.22}$$

which, in the limit of $L \ll 1$, is:

$$\mu_{double} = \frac{\sigma}{L^4} + \frac{1}{L^2} - \frac{\pi^2}{3d^2} + \frac{\sigma\pi^4}{45d^4} + \left(\frac{\pi^4}{15d^4} - \frac{4\sigma\pi^6}{945d^6}\right)L^2 + O\left(L^4\right). \tag{4.23}$$

Minimizing the energy density with respect to the separation between individual inclusions within a line, d, we find:

$$d_{eqm} = \sqrt{\frac{2\sigma\pi^2}{15}} + \sqrt{\frac{3}{245\sigma}}L^2 + O\left(L^4\right). \tag{4.24}$$

For $L \ll 1$, the two infinite lines exhibit long range repulsion on the inverse quartic of the separation according to (4.23), similar to the case of two purely isotropic inclusions [41, 101]. This curvature-mediated repulsion depends directly on the ratio between isotropic and symmetry-breaking effects exerted by the inclusion σ. The energy minimizing distance between the lines is at infinity, given that (4.22) is a monotonically decreasing function with respect to L. We also note that, with the addition of the second infinite line, the separation between individual inclusions within a line is dependent on the distance of the opposing line. Under close separations, (4.24) predicts that this equilibrium distance becomes larger, suggesting that the opposing infinite line exerts curvature-mediated forces which drive the inclusions apart.

4.2.4 Simulation of two finite lines

In the previous section, we assumed that the two linear aggregates were infinite and would not deform, thereby remaining straight during repulsion. We now suppose that the two lines are finite and simulate this scenario by numerically solving (4.13) and (4.14) to determine the shapes of the aggregate that occur and how it affects the repulsive behavior. In particular, we simulate 100 inclusions with $\sigma = 1$ and $b = \rho = 1$ and with initial positions such that there are two individual lines with 50 inclusions individually spaced by d_{eqm}, as defined in (4.19), and with the lines separated horizontally by $L = 5$. The initial orientations of all inclusions is taken to be parallel to the x-axis. We plot the results in Fig. 4.3 for simulation times $t = \{0, 40, 200, 10^{12}\}$.

We observe that the two linear aggregates repel unevenly, repelling the greatest at the ends, but also exhibiting a slight bulge in the center (see $t = 20$). As time

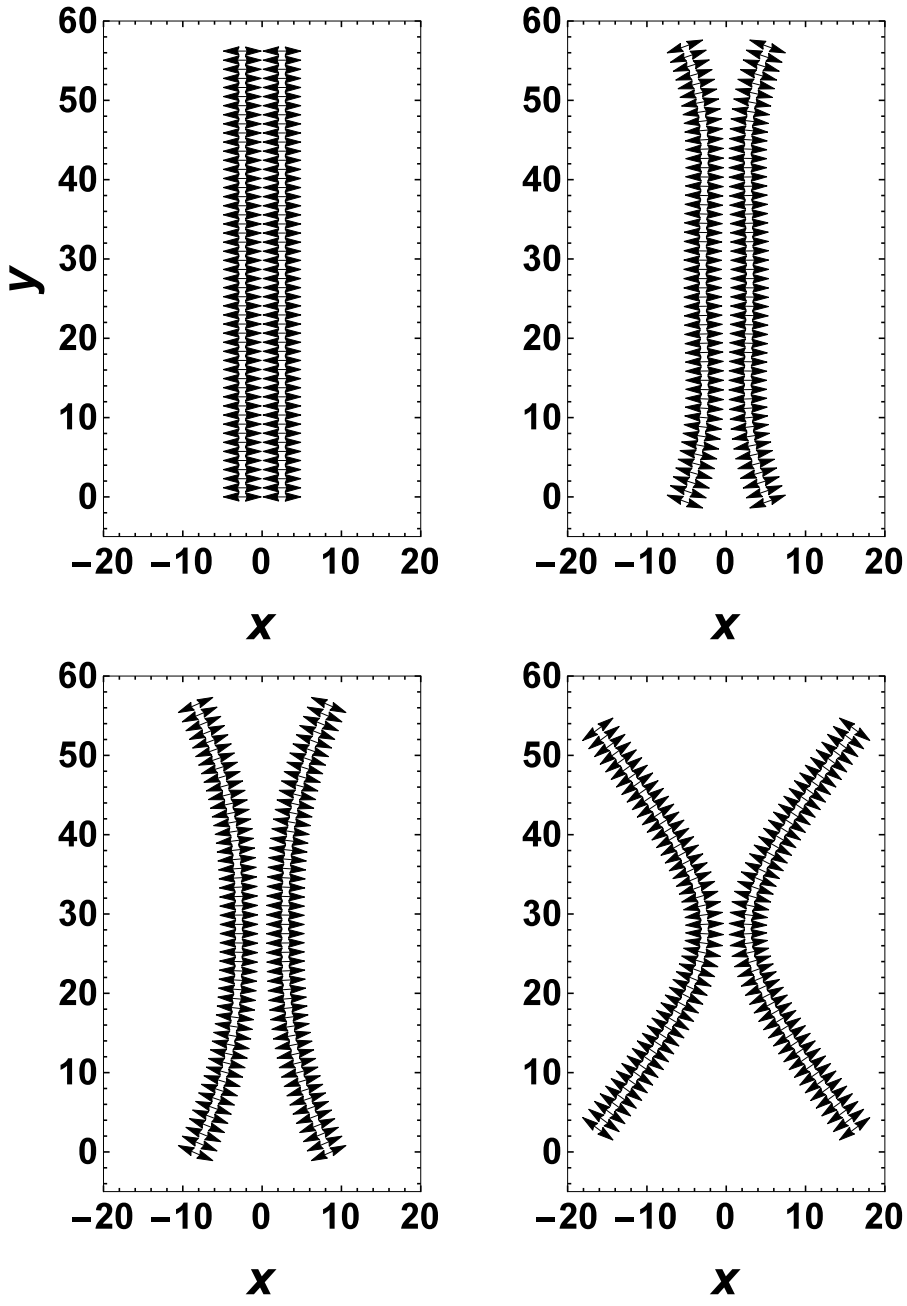

Figure 4.3: Simulation of two finite lines, containing 50 symmetry-breaking inclusions each (shown as black double-headed arrows), by numerically solving (4.13) and (4.14) with parameters $\sigma = b = \rho = 1$. The initial separation of the lines is $L = 5$ whilst the separation between individual inclusions within a line is d_{eqm} as defined in (4.19). The initial orientation of all inclusions is parallel to the x-axis. Times shown from left to right and top to bottom are $t = \{0, 40, 200, 10^{12}\}$.

evolves, the ends of the aggregate further repel leading to a hyperbolic shape, which is straight at the ends, but is curved at the center of the finite line. One would expect that repulsion between the two lines would occur, however, simulating the system for longer times (up to $t = 10^{12}$) gives the unexpected result that the two lines reach an equilibrium distance. Due to the deformation of the ends of the linear aggregates, the symmetry-breaking inclusions now exhibit an orientation which create curvature-mediated attractive forces that keep the two lines together.

4.3 Polygonal aggregates

4.3.1 Energy of a polygon

We study identical symmetry-breaking inclusions that are evenly spaced in a polygonal configuration. We suppose that there are N inclusions, with each inclusion being separated by a distance P from the center. The side lengths of the polygon, S, is related to P by [98]:

$$P = \frac{S}{2}\text{cosec}\frac{\pi}{N}. \tag{4.25}$$

The position (x_i, y_i) of each inclusion is given by:

$$x_i = P\cos\frac{2\pi i}{N}, \tag{4.26}$$

$$y_i = P\sin\frac{2\pi i}{N}, \tag{4.27}$$

whilst the orientations are taken to point in the same direction as the inclusion's separation from the center of the polygon:

$$\psi_i = \frac{2\pi i}{N}. \tag{4.28}$$

We calculate the energy density of the polygon μ_{poly} by considering the energy contribution of a single inclusion. Without loss of generality, we take this to be the Nth inclusion, given that the energy of the polygonal aggregate is invariant under a rotation of $2\pi/N$. In this case, noting that $x_N = P$ and $y_N = 0$, and using the definition Δ_{ij} as the separation between the jth and ith inclusions, we find (4.8) becomes:

$$\mu_{poly} = \sum_{j=1}^{N-1} \frac{8P^2 - 4P^2\csc^2\left(\frac{j\pi}{N}\right) + \sigma\csc^4\left(\frac{j\pi}{N}\right)}{16P^4}. \tag{4.29}$$

We compute the finite sum using the symbolic algebra program *Mathematica* to find:

$$\mu_{poly} = -\frac{(N-1)(N-5)}{12P^2} + \frac{\sigma(N^4+10N^2-11)}{720P^4}, \tag{4.30}$$

and, by minimizing this energy density with respect to the separation distance of the inclusion from the polygon's center, we obtain the equilibrium distance P_{eqm}:

$$P_{eqm} = \sqrt{\frac{\sigma\left(N^4 + 10N^2 - 11\right)}{30\left(N-1\right)\left(N-5\right)}}, \tag{4.31}$$

with corresponding equilibrium side length S_{eqm}:

$$S_{eqm} = 2\sin\left(\frac{\pi}{N}\right)\sqrt{\frac{\sigma\left(N^4 + 10N^2 - 11\right)}{30\left(N-1\right)\left(N-5\right)}}. \tag{4.32}$$

We note some interesting aspects of (4.30)-(4.32). First, for $N < 5$, we note that the denominator of (4.31) and (4.32) is imaginary, unless $\sigma < 0$. This result suggests that, for aggregates featuring 3 or 4 inclusions, the inclusions do not have orientations given by (4.28), but are a rotation by $\pi/2$ of this angle, so that:

$$\psi_i = \frac{\pi}{2} + \frac{2\pi i}{N}. \tag{4.33}$$

In this case, the orientation of the inclusions are perpendicular to their separation from the center of the polygon.

Second, we note that $P_{eqm} \to \infty$ for $N = 5$, implying that the symmetry-breaking inclusions will not form a finite pentagon aggregate. For $N > 5$, the expression in the square root of (4.31) is always positive, implying that P_{eqm} is real, leading to the result that the inclusion orientations are described by (4.28).

Lastly, we take the continuum limit $N \to \infty$ of the equilibrium polygon side length (4.32):

$$S_{eqm} = \sqrt{\frac{2\sigma\pi^2}{15}} + O\left(\frac{1}{N}\right), \tag{4.34}$$

and find that this result is the same as the separation distance between individual inclusions on a single infinite line (4.19). This is an expected result, given that the straight line is the limit of a circle with a radius going to ∞.

4.3.2 Stability of a polygon

We determine the robustness of polygonal aggregates under perturbations to the position and orientation of a single inclusion. We first determine this local stability analytically by considering perturbations to a single inclusion, which we take to be the Nth inclusion without loss of generality, given the rotational invariance of the

polygonal aggregate. We evaluate the Hessian matrix H at the inclusion position and orientation specified in (4.26)-(4.28) (or (4.33) for $N < 5$):

$$H = \begin{bmatrix} \frac{\partial^2 V}{\partial x_N^2} & \frac{\partial^2 V}{\partial x_N \partial y_N} & \frac{\partial^2 V}{\partial x_N \partial \psi_N} \\ \frac{\partial^2 V}{\partial x_N \partial y_N} & \frac{\partial^2 V}{\partial y_N^2} & \frac{\partial^2 V}{\partial y_N \partial \psi_N} \\ \frac{\partial^2 V}{\partial x_N \partial \psi_N} & \frac{\partial^2 V}{\partial y_N \partial \psi_N} & \frac{\partial^2 V}{\partial \psi_N^2} \end{bmatrix}, \tag{4.35}$$

with second derivatives of (4.8) given in Appendix A, and determine the eigenvalues of the resultant matrix to find the local stability.

For polygonal aggregates featuring $N = \{3, 4, 6\}$ inclusions, we find that the corresponding eigenvalues of the Hessian (4.35) are:

$$\lambda_3 = \left\{ \frac{1}{2\sigma^2}, \frac{1}{2\sigma^2}, \frac{1}{\sigma} \right\}, \tag{4.36}$$

$$\lambda_4 = \left\{ \frac{10}{729\sigma^2}, \frac{29 + 81\sigma \pm \sqrt{841 + 81\sigma\,(104 + 81\sigma)}}{729\sigma^2} \right\}, \tag{4.37}$$

and

$$\lambda_6 = \left\{ -\frac{2484950}{35611289\sigma^2}, \right. \\ \left. 25 \left[\frac{(13589 - 108241\sigma)}{35611289\sigma^2} \right. \right. \\ \left. \left. \pm \frac{\sqrt{184660921 + 108241\sigma\,(826648 + 108241\sigma)}}{35611289\sigma^2} \right] \right\}, \tag{4.38}$$

respectively.

We comment on (4.36)-(4.38). We note for the triangle (4.36) that the eigenvalues are all positive, provided that $\sigma > 0$ and we use the inclusion orientation (4.33). This result implies that the triangular aggregate is locally stable under perturbations in the position and orientation of a single inclusion. However, both (4.37) and (4.38) feature a single eigenvalue (i.e. the negative root) which monotonically increases to $-2/9\sigma$, for the case of the square aggregate, and $-50/329\sigma$, for the case of the hexagonal aggregate, as $\sigma \to \infty$, thereby leading to the result that this eigenvalue is negative for all values of $\sigma > 0$. Therefore, local stability analysis shows that both polygonal aggregates with 4 or 6 inclusions are unstable to perturbations.

However, as was noted in Section 4.3.1, the polygon tended to the infinite line in the continuum limit $N \to \infty$. This result further suggests that past a critical number of inclusions in the aggregate, the polygon should be stable to perturbations as the infinite line was shown to be in Section 4.2.2. We verify this hypothesis by calculating

the minimum eigenvalue of the Hessian (4.35) evaluated at the inclusion positions and orientation (4.26)-(4.28) with $\sigma = \{10^{-3}, 1, 10^{3}\}$ for polygons featuring $N = \{6, 7, ..., 15\}$ inclusions in Fig. 4.4. As conjectured, the local stability of the polygon changes from unstable to stable with the addition of more inclusions. Furthermore, we obtain the surprising result that the critical number of inclusions whereby the aggregate is stable appears to be the same regardless of the value of σ; that is, 11 inclusions. For polygons with 11 inclusions and higher, the minimum eigenvalue is positive, implying that the configuration is locally energy minimizing. However, we note that the magnitude of the minimum eigenvalue increases with increasing number of aggregate inclusions, leading to the result that the polygon configuration becomes more stable as it approaches the infinite line regime of $N \to \infty$.

We study the behavior of polygonal aggregates under larger perturbations and the configurations they form when they break apart. We simulate polygons featuring $N = 25$ and $N = 50$ inclusions, with the initial position of all inclusions specified by (4.26) and (4.27), with P_{eqm} given by (4.31), and the initial orientation of the inclusions satisfying (4.28), except for the Nth inclusion which has an orientation of $\pi/2$. We solve (4.13) and (4.14) for the parameters $\sigma = b = \rho = 1$ and plot the results in Fig. 4.5. We remark on some aspects of the simulation. For the polygonal aggregate comprised of 25 inclusions (left column of Fig. 4.5), we note that a significant perturbation to the orientation of the 25th inclusion results in curvature-mediated repulsion which breaks open the polygon and expels the perturbed inclusion (i.e. $t = 50$). The broken polygonal aggregate straightens to form the energy minimizing finite line whilst the single expelled inclusion settles an equilibrium distance away from the main line (i.e. $t = 10^{12}$). Curvature-mediated attraction from the ends of the linear aggregate balances with the repulsion from the center to give this equilibrium distance.

On the other hand, perturbing the polygonal aggregate with 50 inclusions (right column of Fig. 4.5) results in a similar expulsion of the perturbed inclusion, but also the reforming of the polygon (i.e. $t = 3$). The polygon configuration appears to be more robust to perturbations, coinciding with our previous analysis of the Hessian spectrum in Fig. 4.4. Furthermore, the expelled inclusion has a significantly smaller equilibrium separation from the main aggregate compared to the simulation featuring $N = 25$ inclusions. The complete polygon appears to exert greater curvature-mediated attraction and less repulsion than the straight line (i.e. $t = 10^{12}$). The simulation shows that polygons which break apart under perturbations will reconfig-

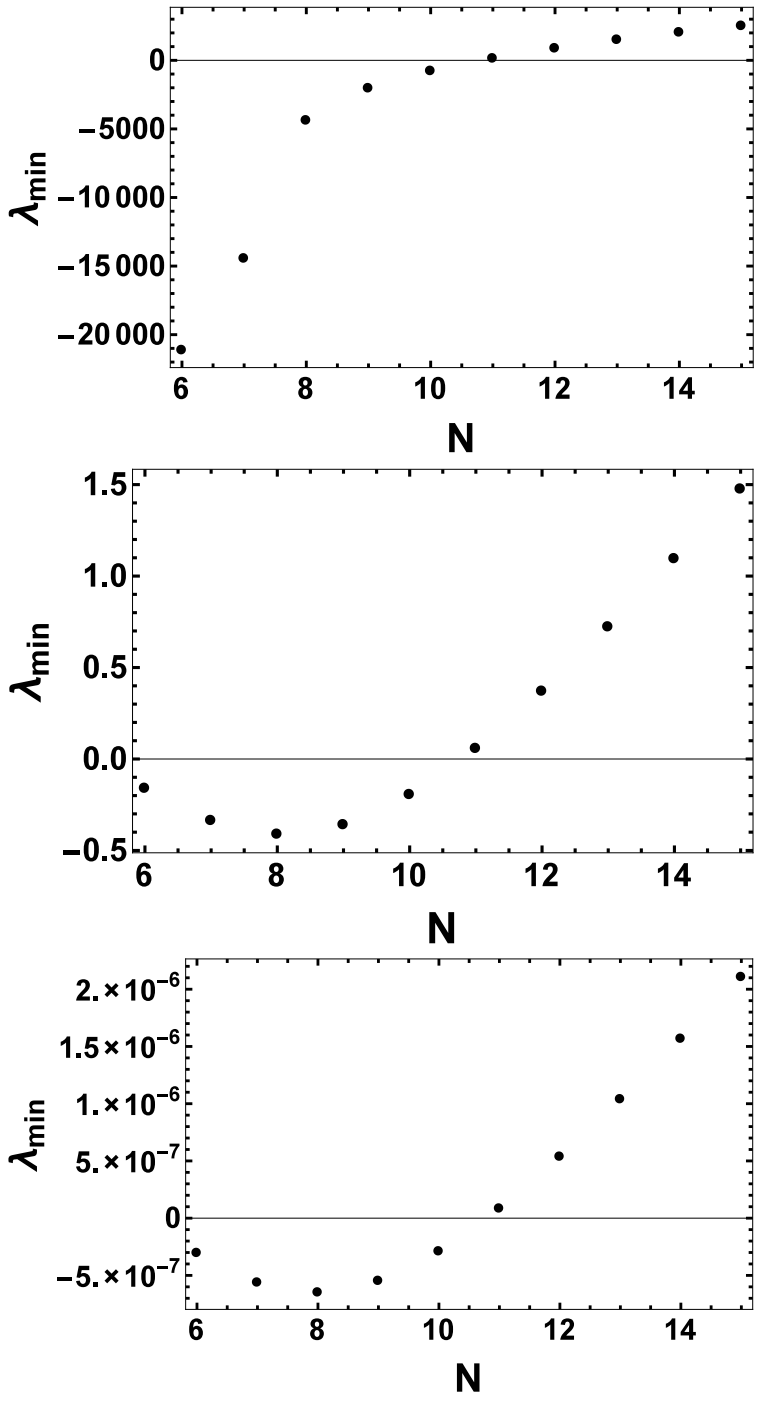

Figure 4.4: The minimum eigenvalue λ_{min} of the Hessian (4.35) evaluated at the inclusion positions and orientation (4.26)-(4.28) for polygonal aggregates comprised of $N = \{6, 7, ..., 15\}$ inclusions. From top to bottom, the value for σ is $\{10^{-3}, 1, 10^3\}$.

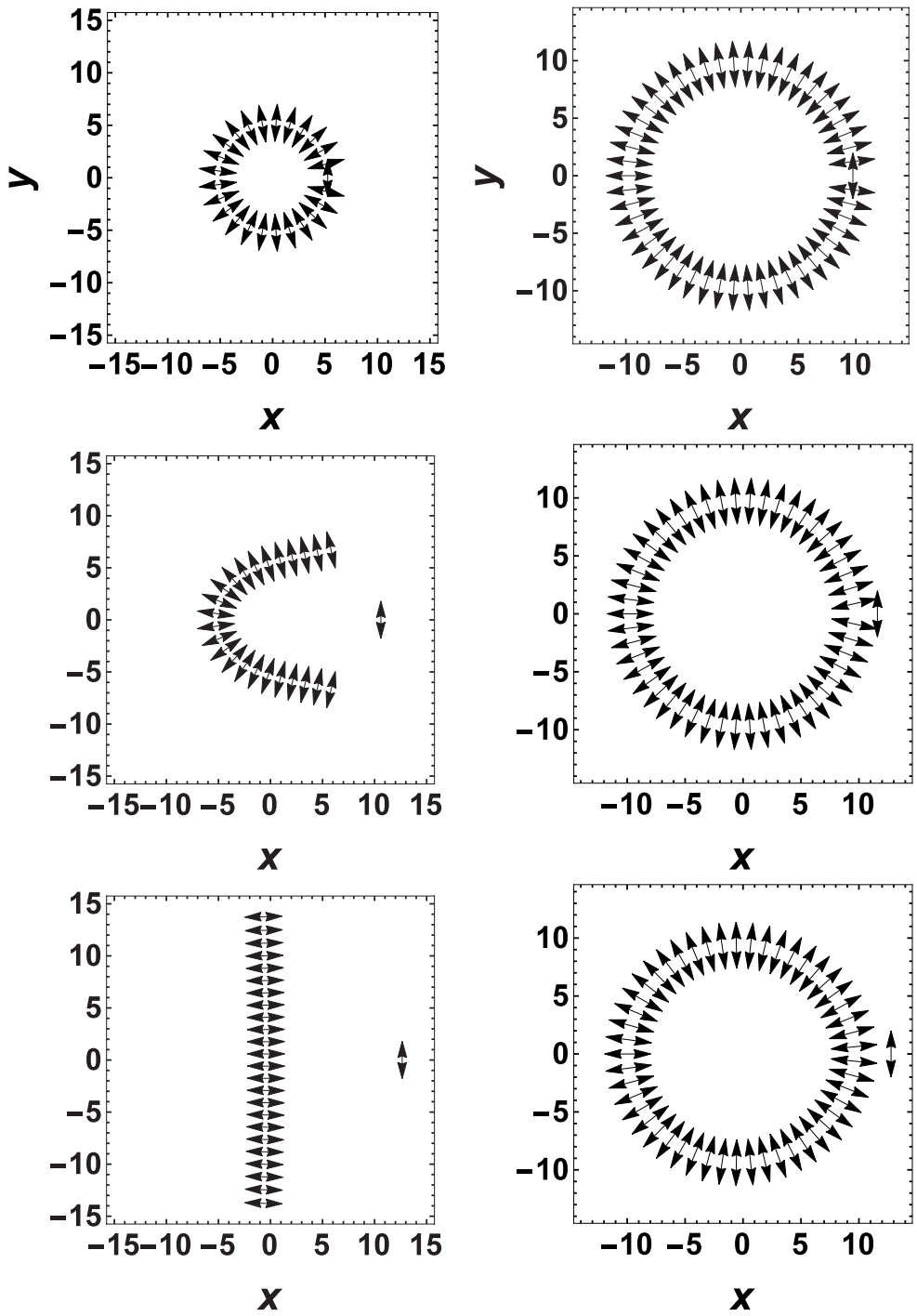

Figure 4.5: Simulation of a polygonal aggregate by numerically solving (4.13) and (4.14) for $N = 25$ (left column) and $N = 50$ (right column) symmetry-breaking inclusions (shown as black double-headed arrows). Both simulations are solved with the parameters $\sigma = b = \rho = 1$. The initial positions of all inclusions are given by (4.26) and (4.27) with P_{eqm} given by (4.31), whilst the initial orientations for all inclusions is (4.28), except for the Nth inclusion which has an orientation of $\pi/2$. Times for the left column shown from top to bottom are $t = \{0, 50, 10^{12}\}$, whilst times for the right column are $t = \{0, 3, 10^{12}\}$.

ure themselves to form linear aggregates, whilst polygons which are comprised of a sufficiently large number of inclusions will reform the polygonal aggregate.

4.4 Collective elastic properties

We study the macroscopic elastic properties of the aggregate formed by the symmetry-breaking inclusions. Compared to previous work involving the deformations of a self-assembled chain of magnetic spheres [42, 98, 80], the aggregate is not only flexible but also extensible. Therefore, we draw analogies to classical elastica to determine the behavior of the aggregate under bending and stretching deformations.

4.4.1 Bending deformations

Suppose we take a sub-aggregate of N inclusions out of the infinite linear aggregate studied in Section 4.2.1, with individual separation distance between inclusions given by (4.19), and bend this aggregate into a polygon of constant curvature. Note that the side of the polygon is also given by (4.19) because we only want to probe the effects of bending, and not stretching, the aggregate. The difference of energy between the two aggregate configurations ΔE_b in the continuum limit $N \to \infty$ is given by:

$$\Delta E_b = 4\kappa\pi\varepsilon\alpha_0\alpha_2 N\left(\mu_{poly} - \mu_{line}\right) = 60\kappa\pi\varepsilon\alpha_2^2 + O\left(\frac{1}{N}\right), \tag{4.39}$$

where we have transformed the energy densities μ_{poly}, defined in (4.30), and μ_{line}, defined in (4.18), into the rescaled energy by multiplying by N and have introduced the original scaling for the energy as defined in (4.7) along with the definition that $\sigma = \alpha_0/\alpha_2$. We note that the aggregate under bending deformations is energetically unfavorable compared to the straight line in the continuum limit, given that $\Delta E_b > 0$.

We suppose that the aggregate has a bending energy E_{bend} given by:

$$E_{bend} = \int_0^{Nd_{eqm}} \frac{D}{|P_{bend}|}\mathrm{d}s, \tag{4.40}$$

where D is a constant parameter related to the resistance of the aggregate to bending deformations, $P_{bend} = d_{eqm}/\left(2\sin\left(\pi/N\right)\right)$, and s is an arclength coordinate taken over the entire length of the aggregate Nd_{eqm}.

Given that we are considering a polygon which has a constant radius of curvature, we find the bending energy:

$$E_{bend} = \frac{DL}{|P|} = D\pi + O\left(\frac{1}{N^2}\right). \tag{4.41}$$

Upon demanding that (4.39) and (4.41) are equivalent, we find that the bending resistance of the aggregate is given by:

$$D = 60\kappa\varepsilon\alpha_2^2 + O\left(\frac{1}{N}\right). \tag{4.42}$$

The aggregate formed by the symmetry-breaking inclusions on the approximately flat membrane is unlike the classical elastica, given its dependence on the inverse radius of curvature P^{-1} in (4.41), rather than the inverse squared P^{-2} typically seen with elastica. This, along with the bending resistance D being constant according to (4.42), shows that the aggregate behaves as a strain-stiffening material; bending the aggregate requires more force the further the aggregate is bent. Furthermore, the aggregate becomes more resistant to bending if the underlying lipid bilayer is stiffer, the radius of the inclusion is larger, or the anistropic deformation imposed by the inclusion on the membrane is larger (see (4.42)). The latter is a result of the aggregate preferring to unravel and form the linear aggregate, such as in Fig. 4.5, given that this is the energy-minimizing configuration according to (4.39).

4.4.2 Stretching deformations

We now consider the energy necessary to stretch a sub-aggregate of N inclusions from the infinite linear aggregate, with undeformed adjacent separation d_{eqm} as defined in (4.19), to a new deformed distance given by d_{def}. The stretching energy E_s is determined by finding the energy difference between the deformed and undeformed states; that is the difference between (4.18) evaluated at $d = d_{def}$ and $d = d_{eqm}$:

$$E_s = 4\kappa\pi\varepsilon\alpha_0\alpha_2 N\left[-\frac{\pi^2}{3}\left(\frac{1}{d_{def}^2} - \frac{1}{d_{eqm}^2}\right) + \frac{\alpha_0\pi^4}{45\alpha_2}\left(\frac{1}{d_{def}^4} - \frac{1}{d_{eqm}^4}\right)\right], \tag{4.43}$$

where we have multiplied through by N and have used the scaling defined in (4.7) to obtain the interaction energy, together with $\sigma = \alpha_0/\alpha_2$.

There are two interesting aspects of (4.43) to comment on. First, there exists a single stable equilibrium separation, which is $d_{def} = d_{eqm}$. Any deformation of the adjacent distance between inclusions will result in this separation relaxing to d_{eqm}. Second, it takes an infinite amount of energy to compress the aggregate so that $d_{def} \to 0^+$, according to (4.43), given the isotropic repulsion. In contrast, there is only a finite energy cost to stretch the distance to infinity. For $d_{def} \to \infty$, we find that the stretching energy required is:

$$E_s = 5\kappa\pi\varepsilon\alpha_2^2 N + O\left(\frac{1}{d_{def}^2}\right). \tag{4.44}$$

The energy necessary to pull the linear aggregate apart increases with the stiffness of the membrane, the radius of an individual inclusion, and the magnitude of the anisotropic deformation. The symmetry-breaking imposed by the inclusion is a measure of the attraction between inclusions, therefore one would expect that the energy required to pull apart the aggregate increases with increasing symmetry-breaking deformation.

4.5 Dynamic aggregation simulation

As a final example, we simulate a large number of inclusions which initially have random positions and orientations to show some of the aggregate configurations that are possible. We numerically solve (4.13) and (4.14) for 1000 inclusions with $\sigma = b = \rho = 1$ and with initial positions in the range of $[-50, 50]$ and orientations in $[0, 2\pi]$. We plot a realization of this simulation for times $t = \{0, 10^3, 10^4, 2.5 \times 10^4, 10^5, 10^6\}$ in Fig. 4.6 and make some comments.

Immediately after the simulation starts, the inclusions align and attract forming a network of multiple linear aggregates ($t = 10^3$), similar to molecular dynamics simulations confining a large number of membrane-shaping proteins on a sphere [85]. However, due to curvature-mediated repulsion both as a result of isotropic and anisotropic deformation imposed by the membrane inclusion, the network of aggregates "unzip" to form larger closed loops within it and to form larger linear aggregates at its ends ($t = 10^4$). During the process of aggregate unzipping, some inclusions are expelled, similar to the simulations involving the perturbed line seen in Section 4.2.2. If these inclusions are outside the closed loops, they will be attracted to the ends of the network, whilst inclusions within the closed loops appear to be attracted to the junctions where linear aggregates meet. Furthermore, some linear aggregates form energetically unfavorable angles with lines (see arrows at $t = 2.5 \times 10^4$) resulting in the breaking apart of the network to form straight lines (see arrows at $t = 10^5$). The mesh of aggregates straighten to form the large lines at the ends, and the closed loops resemble large polygons (see $t = 10^6$).

4.6 Chapter summary

In the present work, we applied the curvature-mediated interaction law between symmetry-breaking inclusions derived in Chapter 3 to study aggregate shapes and their corresponding properties. To assist in this study, we generalized the previous

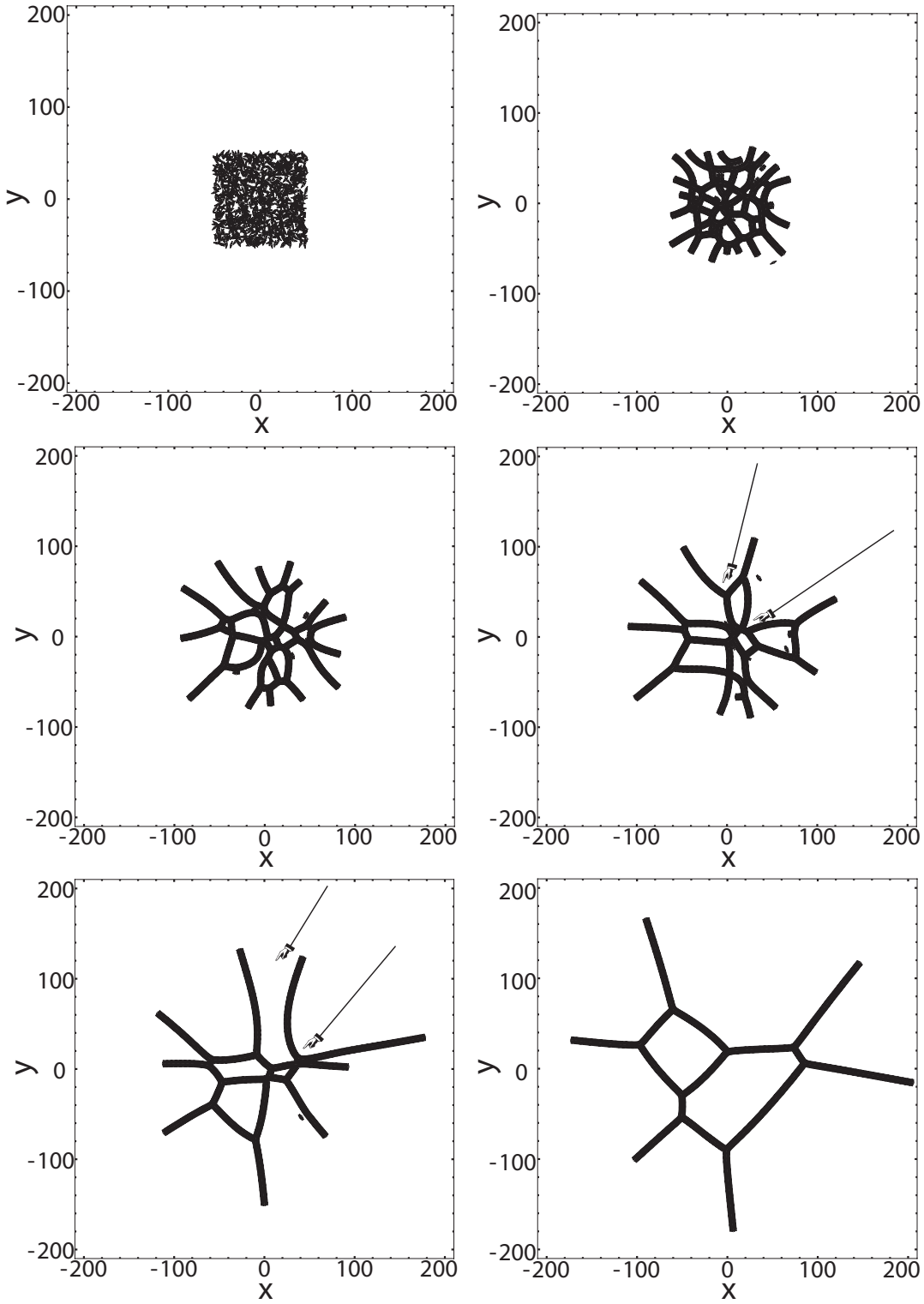

Figure 4.6: Simulation of 1000 symmetry-breaking inclusions (shown as black double-headed arrows) by numerically solving (4.13) and (4.14) with $\sigma = b = \rho = 1$. The initial positions of all inclusions are in the range $[-50, 50]$ whilst the initial orientations are in $[0, 2\pi]$. Times shown from left to right and top to bottom are $t = \{0, 10^3, 10^4, 2.5 \times 10^4, 10^5, 10^6\}$.

interaction law to consider the configuration energy of an arbitrary number of such inclusions and further derived equations of motion to model the dynamical process of the inclusions aggregating.

We considered simplified shapes, the first of these being an infinite straight line with the orientation of the inclusions being perpendicular to the aggregate. We analytically determined the energy density of a single infinite linear aggregate and found the equilibrium separation between individual inclusions on the line. This equilibrium distance was shorter than the result found in for the case of two inclusions due to additional curvature-mediated attractive forces between inclusions within the aggregate. By numerically solving the earlier derived equations of motion, we also determined that the single linear aggregate was robust to large perturbations in the position and orientation of inclusions within it. Though the perturbations resulted in the expulsion of some inclusions from the main aggregate, the infinite linear aggregate reestablished its shape whilst the expelled inclusions aggregated to form a smaller line.

Motivated by the interactions of protein rings on cylindrical geometries, we then considered how two parallel infinite lines would interact, assuming that they would not deform. We found the equilibrium separation between the two infinite lines was at infinity and, in the regime of small separations, the infinite lines would repel on the quartic inverse of the separation length, similar to the repulsion seen for two isotropic inclusions. Furthermore, under this same separation regime, we found that repulsion from the opposing linear aggregate resulted in the equilibrium distance between inclusions within a line to be larger than for the single infinite line. We numerically simulated two finite linear aggregates to determine how they would deform as a result of curvature-mediated interaction and whether this deformation would result in the same repulsion seen for the infinite case. We found that two linear aggregates would bend to create attractive curvature-mediated forces which resulted in a finite equilibrium distance being reached between the two lines.

We then studied polygonal aggregates and determined its energy density and equilibrium side length. We found two different regimes of polygons: For polygons with fewer than 5 inclusions, the orientations of individual inclusions were perpendicular to their separation from the polygon center, whilst for polygonal aggregates with more than 5 inclusions, the orientations of inclusions were such that they were parallel to this separation from the center. Finite pentagonal aggregates were not found to exist. Furthermore, we found that, in the limit of the number of inclusions approaching infinity, the equilibrium side length reduced to the result found for the single infinite line. We then analytically found the local stability of polygons featuring 3, 4,

and 6, to perturbations of a single inclusion's position and orientation. We found that the former was stable, whilst the latter two polygonal aggregates were unstable. However, by calculating the minimum eigenvalue of the Hessian for polygons featuring $\{6, 7, ..., 15\}$ inclusions, we found that aggregates comprised of 11 or more inclusions were locally stable, regardless of the individual inclusion's ratio of isotropic to anisotropic contact angle. Furthermore, the stability of the polygonal aggregate increased with increasing number of inclusions. To determine the configurations formed by polygonal aggregates under large perturbations, we simulated polygons with 25 and 50 inclusions and found that the former broke apart and straightened to form a line whilst the latter reformed the polygonal aggregate, coinciding with previous results on the spectral analysis of the Hessian.

Drawing analogies to classical elastica, we determined the macroscopic elastic properties of the aggregate, given that it was found to be both flexible and extensible. We found that the bending energy of the aggregate resembled that of a strain-stiffening material, whereby further bending of the aggregate resulted in a greater bending resistance. Probing the stretching properties of the aggregate, we found that there existed only a single equilibrium separation distance between inclusions. Furthermore, we found that curvature-mediated repulsion resulted in infinite energy being required to push the separation distance between inclusions to 0, whilst only finite energy was necessary to pull the inclusion separation to infinity.

Given that we only studied simplified shapes, we concluded with a simulation showing 1000 inclusions which initially had random positions and random orientations to show some of the transient aggregate shapes that could exist. We found that the inclusions would immediately self-assemble into a network of linear aggregates that would feature "unzipping" to create larger closed loops within the network and larger linear aggregates at its ends. We observed that, if lines met at energetically unfavorable angles, they would break apart and reorganize to create larger linear aggregates.

Curvature-mediated interactions of symmetry-breaking inclusions embedded in lipid bilayers result in a large family of aggregate shapes with unusual collective properties that are significantly different from other similar physical systems, such as the assembly of magnetic spheres and particles on fluid surfaces. The present work has highlighted only some of these simplified shapes, but has also shown that, even with simple configurations, the interactions between inclusions and aggregates are non-intuitive and warrant further investigation.

Appendix A: Construction of Hessian

We explicitly state the second derivatives necessary to construct the Hessian of the polygonal aggregate (4.35). By taking the first derivatives of the energy with respect to the position vector $\boldsymbol{r}_k$ and orientation ψ_k of the kth inclusion, used in the equations of translational and rotational motion (4.13) and (4.14), we find:

$$\begin{aligned}\frac{\partial^2 V}{\partial \boldsymbol{r}_k^2} = 4\sum_{j\neq k}^{N}\Bigg[&\frac{\boldsymbol{\Psi}_k\otimes\boldsymbol{\Psi}_k+\boldsymbol{\Psi}_j\otimes\boldsymbol{\Psi}_j+\mathbb{I}_2}{|\boldsymbol{\Delta}_{jk}|^4}\\ &-\frac{2}{|\boldsymbol{\Delta}_{jk}|^6}\left[4\left(\boldsymbol{\Psi}_k\cdot\boldsymbol{\Delta}_{jk}\right)\boldsymbol{\Psi}_k\otimes\boldsymbol{\Delta}_{jk}+4\left(\boldsymbol{\Psi}_j\cdot\boldsymbol{\Delta}_{jk}\right)\boldsymbol{\Psi}_j\otimes\boldsymbol{\Delta}_{jk}\right.\\ &\qquad\left.+2\boldsymbol{\Delta}_{jk}\otimes\boldsymbol{\Delta}_{jk}+\left(\sigma+\left(\boldsymbol{\Psi}_k\cdot\boldsymbol{\Delta}_{jk}\right)^2\right)\mathbb{I}_2\right]\\ &\qquad+\frac{12}{|\boldsymbol{\Delta}_{jk}|^8}\left(\left(\boldsymbol{\Psi}_k\cdot\boldsymbol{\Delta}_{jk}\right)^2+\left(\boldsymbol{\Psi}_j\cdot\boldsymbol{\Delta}_{jk}\right)^2+\sigma\right)\boldsymbol{\Delta}_{jk}\otimes\boldsymbol{\Delta}_{jk}\Bigg],\end{aligned}\tag{4.45}$$

$$\begin{aligned}\frac{\partial^2 V}{\partial \boldsymbol{r}_k\partial\psi_k} = 4\sum_{j\neq k}^{N}\Bigg\{&\frac{\left(\boldsymbol{\Psi}_k^{\perp}\cdot\boldsymbol{\Delta}_{jk}\right)\boldsymbol{\Psi}_k+\left(\boldsymbol{\Psi}_k\cdot\boldsymbol{\Delta}_{jk}\right)\boldsymbol{\Psi}_k^{\perp}}{|\boldsymbol{\Delta}_{jk}|^4}\\ &-\frac{4\left(\boldsymbol{\Psi}_k\cdot\boldsymbol{\Delta}_{jk}\right)\left(\boldsymbol{\Psi}_k^{\perp}\cdot\boldsymbol{\Delta}_{jk}\right)\boldsymbol{\Delta}_{jk}}{|\boldsymbol{\Delta}_{jk}|^6}\Bigg\},\end{aligned}\tag{4.46}$$

and

$$\frac{\partial^2 V}{\partial \psi_k^2} = 4\sum_{j\neq k}^{N}\frac{\left(\boldsymbol{\Psi}_k^{\perp}\cdot\boldsymbol{\Delta}_{jk}\right)^2-\left(\boldsymbol{\Psi}_k\cdot\boldsymbol{\Delta}_{jk}\right)^2}{|\boldsymbol{\Delta}_{jk}|^4}\tag{4.47}$$

where $\otimes$ is the outer product and $\mathbb{I}_2$ is the 2×2 identity matrix.

Chapter 5

Curvature-mediated interactions on periodic membranes

As eluded to in Chapter 4, symmetry-breaking inclusions on a cylinder have been computationally shown [89] to exhibit a preferred orientation and will subsequently form rings to stabilize the cylindrical geometry [84]. We investigate one of the mechanisms by which this alignment could occur: periodicity in the boundary conditions. We organize this chapter as follows: In Section 5.1, we extend the formalism introduced in Chapter 3 to consider the problem of two symmetry-breaking inclusions on an approximately flat fluid membrane which exhibits periodic boundary conditions along one direction. In Section 5.2, we determine the outer membrane shape due to the images of the membrane inclusions which are a result of the periodic boundary conditions, whilst in Section 5.3, we determine corrections to the shape in the local region of the inclusion as a result of these images by means of asymptotic matching. We calculate the final interaction energy as a consequence of the periodic boundary conditions and remark on the result derived in light of curvature-mediated protein alignment observed in molecular dynamics simulations. In Section 5.5, we follow Chapter 4 to extend the periodic interaction energy derived to model the curvature-mediation of an arbitrary number of inclusions and develop equations of motion which are subsequently numerically solved for 100 inclusions. We summarize our results in Section 5.6.

5.1 Set-up of problem

We study a similar problem as per Section 3.2; namely, considering the interactions between two inclusions which are perfectly circular but break symmetry in the contact angle that they impose on the approximately flat fluid membrane which is taken

to not exhibit larger than logarithmic growth. However, in this case, we suppose that the outer membrane is periodic along one direction. In this case, the energy and the corresponding shape equation of the membrane is given by (3.12) and (3.13) respectively. We take the inclusions to be of radius $\varepsilon^{1/2}$ and suppose that the position of their centers are $x_1 = y_1 = 0$ and $x_2 = R_x$ and $y_2 = R_y$ such that $R_x = R_y = O(1)$ and we suppose that the inclusions impose anistropic deformation at an orientation given by the angle ψ_i with respect to the x-axis. Furthermore, we allow the membrane to extend to $\pm\infty$ along the x direction, whilst in the y direction, the membrane has periodic boundaries at $y = \{-L, L\}$. The addition of the periodic boundary creates infinitely many images of the first inclusion with centers at $x_1 = 0$ and $y_1 = 2Lq$, for $q \in \mathbb{Z}$, whilst the position of the second inclusion's center is $x_2 = R_x$ and $y_2 = 2Lq + R_y$ (see Fig. 5.1). We aim to determine the effect of these inclusion images on the resulting interaction of the real inclusions within $y \in [-L, L]$.

Given that we are solving the same local problem as in Section 3.2, the conditions at the inclusion boundary are (3.29)-(3.33) and the local shapes around the first and second inclusion are generally given by (3.37) and (3.38). We determine corrections to b_8, b_{82}, $\hat{b_8}$, and $\hat{b_{82}}$, which contribute to the interaction between the inclusions, from the periodic outer membrane. Note that b_{82} and $\hat{b_{82}}$ is $O\left(\varepsilon^{3/2}\right)$ only if $R_y = 0$ because the membrane remains invariant under the reflection $y \to -y$.

5.2 Periodic outer membrane solution

We note that, given the leading order local shape of the membrane inclusion is logarithmic, the outer membrane is similarly logarithmic. However, these logarithmic contributions originate not only from the real inclusions within $y \in [-L, L]$, but also their respective images with positions at $x_1 = 0$ and $y_1 = 2Lq$ and $x_2 = R_x$ and $y_2 = 2Lq + R_y$ for the first and second inclusion respectively, for $q \in \mathbb{Z}$. Therefore, the leading order periodic outer membrane solution which satisfies (3.13) is a linear superposition of these contributions:

$$h_m = c_0 + \sum_{q=-\infty}^{\infty} \left[\frac{\alpha_1^{(0)}}{2} \ln\left(x^2 + (y - 2qL)^2\right) + \frac{\alpha_2^{(0)}}{2} \ln\left((x - R_x)^2 + (y - R_y - 2qL)^2\right) \right]. \tag{5.1}$$

We similarly note, as with Section 3.2.3, that the higher order corrections to the outer membrane shape are $O(\varepsilon)$ and therefore do not contribute to the final interaction energy.

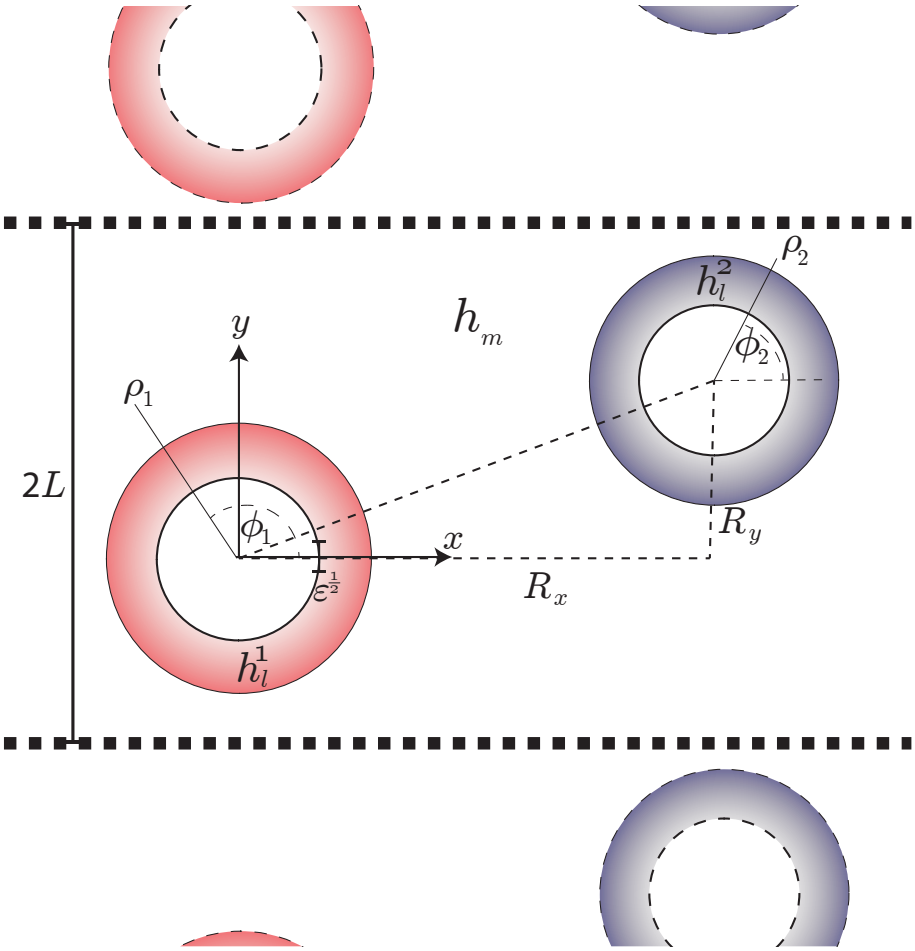

Figure 5.1: A schematic diagram of the interaction of two identical symmetry-breaking inclusions of radius $\varepsilon^{\frac{1}{2}}$ with $\varepsilon \ll 1$ on an approximately flat membrane which is periodic and of length $2L$ in the y direction (denoted by thick dashed line). The inclusions are taken to have perfectly circular boundaries with centers separated by a distance $R_x = O(1)$ and $R_y = O(1)$ along the x and y axes respectively. In all, there are three regions in which the membrane shape must be determined by (3.13): The inner layer regions around the inclusions h_l^1 and h_l^2 which are parametrized by local radial-angle coordinates (ρ_i, ϕ_i) (denoted by red and blue regions respectively), and the outer membrane region h_m in the coordinates (x, y) (denoted by the white region). Due to the periodic nature of the boundaries, each real inclusion has images (denoted by the red and blue dashed circles) which will contribute to the interaction energy.

5.3 Asymptotic matching

We match the periodic outer membrane shape with the local shape of the first real inclusion. We transform (5.1) into the local polar variables by $x = \varepsilon^{1/2}\rho_1 \cos\phi_1$ and $y = \varepsilon^{1/2}\rho_1 \sin\phi_1$ and expand in the limit of $\varepsilon \ll 1$ to find:

$$\begin{aligned} h_m = c_0 + \alpha_1^{(0)} \ln\varepsilon + \alpha_1^{(0)} \ln\rho_1 \\ + \sum_{\substack{q=-\infty \\ q\neq 0}}^{\infty} \left[\alpha_1^{(0)} \ln 2qL - \frac{\varepsilon^{\frac{1}{2}} \alpha_1^{(0)} \rho_1 \sin\phi_1}{2Lq} + \frac{\varepsilon \alpha_1^{(0)} \rho_1^2 \cos 2\phi_1}{8L^2 q^2} \right] \\ + \sum_{q=-\infty}^{\infty} \left[\frac{1}{2}\alpha_2^{(0)} \ln\left(R_x^2 + (R_y + 2Lq)^2\right) - \frac{\varepsilon^{\frac{1}{2}} \alpha_2^{(0)} \rho_1 \left(R_x \cos\phi_1 + (2Lq + R_y)\sin\phi_1\right)}{R_x^2 + (2Lq + R_y)^2} \right. \\ \left. + \frac{\varepsilon \alpha_2^{(0)} \rho_1^2 \left(2Lq - R_x - R_y\right)\left(2Lq + R_x - R_y\right)\cos 2\phi_1}{2\left(R_x^2 + (2Lq + R_y)^2\right)^2} + \frac{\varepsilon \alpha_2^{(0)} \rho_1^2 R_x \left(2Lq - R_y\right)\sin 2\phi_1}{\left(R_x^2 + (2Lq + R_y)^2\right)^2} \right] \\ + O\left(\varepsilon^{\frac{3}{2}}\right). \quad (5.2) \end{aligned}$$

Comparing with the local shape of the first real inclusion (3.37), we match $\rho_1^2 \cos 2\phi_1$ and $\rho_1^2 \sin 2\phi 1$ terms to obtain:

$$b_8 = \sum_{\substack{q=-\infty \\ q\neq 0}}^{\infty} \frac{\varepsilon \alpha_1^{(0)}}{8L^2 q^2} + \sum_{q=-\infty}^{\infty} \frac{\varepsilon \alpha_2^{(0)} \left(2Lq - R_x - R_y\right)\left(2Lq + R_x - R_y\right)}{2\left(R_x^2 + (2Lq + R_y)^2\right)^2}, \quad (5.3)$$

$$b_{82} = \sum_{q=-\infty}^{\infty} \frac{c_1^{\hat{(q)}(0)} R_x \left(2Lq - R_y\right)}{\left(R_x^2 + (2Lq + R_y)^2\right)^2}. \quad (5.4)$$

where we have only considered terms necessary in calculating the interaction energy. We further note that b_8 depends on $\alpha_2^{(0)}$ and also $\alpha_1^{(0)}$ according to (5.3). The first inclusion interacts with the deformation imposed by the second inclusion, as previously seen in Section 3.2, however, with periodic boundary conditions on the outer membrane, the first inclusion further interacts with its own images, as well as the images of the second inclusion.

We determine the effective contribution of the images by evaluating the infinite sums using the symbolic algebra program *Mathematica* to find:

$$\begin{aligned} b_8 = \frac{\varepsilon\pi^2}{48L^2\left(\cos\left(\frac{\pi R_y}{L}\right) - \cosh\left(\frac{\pi R_x}{L}\right)\right)^2} \left[2\alpha_1^{(0)} + 12\alpha_2^{(0)} + \alpha_1^{(0)} \cos\left(\frac{2\pi R_y}{L}\right) \right. \\ \left. -4\left(\alpha_1^{(0)} + 3\alpha_2^{(0)}\right)\cos\left(\frac{\pi R_y}{L}\right)\cosh\left(\frac{\pi R_x}{L}\right) + \alpha_1^{(0)} \cosh\left(\frac{2\pi R_x}{L}\right) \right], \quad (5.5) \end{aligned}$$

and:

$$b_{82} = -\frac{\varepsilon\pi^2\alpha_2^{(0)}\sin\left(\frac{\pi R_y}{L}\right)\sinh\left(\frac{\pi R_x}{L}\right)}{4L^2\left(\cos\left(\frac{\pi R_y}{L}\right)-\cosh\left(\frac{\pi R_x}{L}\right)\right)^2}. \tag{5.6}$$

We comment that $b_{82} = O\left(\varepsilon^{3/2}\right)$ for $R_y = 0$, as posited previously. Furthermore, we note that both (5.5) and (5.6) are periodic in R_y, as would be expected given the periodic nature of the membrane.

We match the periodic outer membrane with the second real inclusion. We express (5.1) in terms of local polar variables (ρ_2, ϕ_2) according to $x - R_x = \varepsilon^{1/2}\rho_2\cos\phi_2$ and $y - R_y = \varepsilon^{1/2}\rho_2\sin\phi_2$ to obtain:

$$\begin{aligned} h_m = {} & c_0 + \alpha_2^{(0)}\ln\varepsilon + \alpha_2^{(0)}\ln\rho_1 \\ & + \sum_{\substack{q=-\infty \\ q\neq 0}}^{\infty}\left[\alpha_2^{(0)}\ln 2qL - \frac{\varepsilon^{\frac{1}{2}}\alpha_2^{(0)}\rho_2\sin\phi_2}{2Lq} + \frac{\varepsilon\alpha_2^{(0)}\rho_2^2\cos 2\phi_2}{8L^2q^2}\right] \\ & + \sum_{q=-\infty}^{\infty}\left[\frac{1}{2}\alpha_1^{(0)}\ln\left(R_x^2+(R_y-2Lq)^2\right) + \frac{\varepsilon^{\frac{1}{2}}\alpha_1^{(0)}\rho_2\left(R_x\cos\phi_2+(R_y-2Lq)\sin\phi_2\right)}{R_x^2+(R_y-2Lq)^2}\right. \\ & \left. + \frac{\varepsilon\alpha_1^{(0)}\rho_2^2\left(R_y-2Lq-R_x\right)\left(R_y-2Lq+R_x\right)\cos 2\phi_2}{2\left(R_x^2+(R_y-2Lq)^2\right)^2} + \frac{\varepsilon\alpha_1^{(0)}\rho_2^2R_x\left(2Lq-R_y\right)\sin 2\phi_2}{\left(R_x^2+(R_y-2Lq)^2\right)^2}\right] \\ & + O\left(\varepsilon^{\frac{3}{2}}\right). \end{aligned} \tag{5.7}$$

Comparing with the local shape of the second real inclusion (3.38), we obtain the result:

$$\hat{b_8} = \sum_{\substack{q=-\infty \\ q\neq 0}}^{\infty}\frac{\varepsilon\alpha_2^{(0)}}{8L^2q^2} + \sum_{q=-\infty}^{\infty}\frac{\varepsilon\alpha_1^{(0)}\left(R_y-2Lq-R_x\right)\left(R_y-2Lq+R_x\right)}{2\left(R_x^2+(R_y-2Lq)^2\right)^2}, \tag{5.8}$$

$$\hat{b_{82}} = \sum_{q=-\infty}^{\infty}\frac{\varepsilon\alpha_1^{(0)}R_x\left(2Lq-R_y\right)}{\left(R_x^2+(R_y-2Lq)^2\right)^2}. \tag{5.9}$$

Similarly, $\hat{b_8}$ is now dependent on $\alpha_2^{(0)}$; the second inclusion interacts with the deformations imposed by the first inclusion and its copies as well as the second inclusion's own images.

We evaluate the infinite sums in (5.8) and (5.9) by means of *Mathematica* to find:

$$\hat{b_8} = \frac{\varepsilon\pi^2}{48L^2\left(\cos\left(\frac{\pi R_y}{L}\right)-\cosh\left(\frac{\pi R_x}{L}\right)\right)^2}\left[2\alpha_2^{(0)}+12\alpha_1^{(0)}+\alpha_2^{(0)}\cos\left(\frac{2\pi R_y}{L}\right)\right]$$
$$-4\left(\alpha_2^{(0)}+3\alpha_1^{(0)}\right)\cos\left(\frac{\pi R_y}{L}\right)\cosh\left(\frac{\pi R_x}{L}\right)+\alpha_2^{(0)}\cosh\left(\frac{2\pi R_x}{L}\right), \quad (5.10)$$

and:

$$\hat{b_{82}} = -\frac{\varepsilon\pi^2\alpha_1^{(0)}\sin\left(\frac{\pi R_y}{L}\right)\sinh\left(\frac{\pi R_x}{L}\right)}{4L^2\left(\cos\left(\frac{\pi R_y}{L}\right)-\cosh\left(\frac{\pi R_x}{L}\right)\right)^2}. \quad (5.11)$$

We similarly note the vanishing of $\hat{b_{82}}$ for $R_y = 0$, and the periodicity in R_y in both (5.10) and (5.11).

5.4 Calculation of interaction energy

We have sufficient energy to determine the interaction of two symmetry-breaking inclusions on a periodic flat membrane. We follow the same procedure as in Section 3.2.4 and determine the inner Laplacians of the first and second inclusions' local shapes:

$$\nabla^2 h_l^1 = \frac{2}{\varepsilon\rho_1^2}\left(4b_8\cos 2\phi_1 + 4b_{82}\sin 2\phi_1 - \alpha_1^{(2)}\cos\left(2\phi_1-2\psi_1\right)\right)+O\left(1\right), \quad (5.12)$$

$$\nabla^2 h_l^2 = \frac{2}{\varepsilon\rho_2^2}\left(4\hat{b_8}\cos 2\phi_2 + 4\hat{b_{82}}\sin 2\phi_2 - \alpha_2^{(2)}\cos\left(2\phi_2-2\psi_2\right)\right)+O\left(1\right), \quad (5.13)$$

where b_8, b_{82}, $\hat{b_8}$, and $\hat{b_{82}}$ are given by (5.5), (5.6), (5.10), and (5.11) respectively, and where we have the multiplicative factor of ε^{-1} due to transforming between the outer membrane coordinates (x, y) and the local polar variables (ρ_i, ϕ_i).

We note that the Laplacian of the periodic outer membrane (5.1) vanishes so that the interaction energy is dominated by the local contributions of the inclusions, as per Section 3.2.4. Therefore, the interaction energy, according to (3.12), is given by:

$$V = \kappa\pi\varepsilon\left\{\left(\alpha_1^{(2)}\right)^2+\left(\alpha_2^{(2)}\right)^2-8\alpha_1^{(2)}\left(b_8\cos 2\psi_1+b_{82}\sin 2\psi_1\right)\right.$$
$$+8\alpha_2^{(2)}\left(\hat{b_8}\cos 2\psi_2+\hat{b_{82}}\sin 2\psi_2\right)+8\alpha_2^{(2)}\left(\hat{b_8}\cos 2\psi_2+\hat{b_{82}}\sin 2\psi_2\right)$$
$$\left.+16\left[b_8^2+b_{82}^2+\hat{b_8}^2+\hat{b_{82}}^2\right]\right\}. \quad (5.14)$$

We remark on (5.14). We note that if $R_x = R$ and $R_y = 0$, then, in the limit of the periodic domain length $L \to \infty$, we obtain (3.51) to leading order, given that the

outer membrane now becomes the infinite flat membrane originally studied in Section 3.2. However, in the absence of a second inclusion (i.e. $\alpha_2^{(0)} = \alpha_2^{(2)} = 0$), we find that (5.14) reduces to:

$$V(\psi_1, L) = \kappa\pi\varepsilon \left[\left(\alpha_1^{(2)}\right)^2 + \frac{\pi^4 \left(\alpha_1^{(0)}\right)^2}{36L^4} - \frac{\pi^2 \alpha_1^{(0)} \alpha_1^{(2)}}{3L^2} \cos 2\psi_1 \right]. \tag{5.15}$$

The energy is dependent on the orientation of the single inclusion ψ_1 implying that periodicity of the membrane boundary results in a preferred alignment.

We calculate the corresponding curvature-mediated torque exerted on the single inclusion due to the deformations imposed by its images:

$$\tau = -\frac{\partial V}{\partial \psi_1} = -\frac{2\kappa\pi^3\varepsilon\alpha_1^{(0)}\alpha_1^{(2)}}{3L^2} \sin 2\psi_1. \tag{5.16}$$

We note that the anisotropic inclusion is in rotational equilibrium for $\psi_1 = n\pi/2$, for $n \in \mathbb{Z}$, with the unstable equilibrium, corresponding to the higher energy state in (5.15), for $\psi_1 = n\pi$, and stable equlibrium, corresponding to the lower energy state, for $\psi_1 = \left(n + \frac{1}{2}\right)\pi$. The preferred alignment of the inclusion is parallel to the periodic membrane boundary. The physical reasoning is that the images of the inclusion exert a curvature-mediated torque on the real inclusion so that it aligns into a configuration whereby curvature-mediated attraction with these images occurs. The separation vector always points along the y-axis, which results in the energy minimizing orientation being along the x-axis. The rotational effect increases as the length of the periodic boundary L decreases, given that the images of the inclusion would move closer to the real inclusion. We note that the magnitude of the torque (5.16) depends on the coupling of the anistropic and isotropic deformations imposed by the single inclusion as the symmetry-breaking of the real inclusion interacts with the isotropy of all its images. Note that the real inclusion would not exhibit translational motion regardless of the length of the periodic boundary. The inclusion's images would exert curvature-mediated attractive forces which would be equal, but opposite in direction so that they would cancel out. Therefore, periodic membrane boundaries only have a rotational effect on the membrane inclusion.

5.5 Numerical simulation

We study the effects of periodic boundaries on the assembly of large numbers of inclusions by means of numerical simulation. We generalize the periodic interaction

law (5.14) to consider an arbitrary number, N, of inclusions by noting, as per Section 4.1.1, that contributions to the interaction energy are dominated by local contributions to the fluid membrane shape. Therefore, the total interaction energy is a summation over all N inclusions:

$$V = \kappa\pi\varepsilon \sum_{i=1}^{N} \left\{ \left(\alpha_i^{(2)}\right)^2 - 8 \sum_{j\neq i}^{N} \left[\alpha_i^{(2)} \left(b_8^{ij} \cos 2\psi_i + b_{82}^{ij} \sin 2\psi_i \right) - 2 \left(\left(b_8^{ij}\right)^2 + \left(b_{82}^{ij}\right)^2 \right) \right] \right\}, \tag{5.17}$$

where b_8^{ij} and b_{82}^{ij} are given by (5.10) and (5.6) respectively, with the transformation $R_x \to R_x^{ij}$ and $R_y \to R_y^{ij}$, where $R_x^{ij} = x_j - x_i$ and $R_y^{ij} = y_j - y_i$ are the separations between the jth and the ith membrane inclusion's center in the x and y directions respectively.

The corresponding phenomenological dynamic model is obtained by taking the partial derivatives of (5.17) with respect to the position vector of the membrane inclusion $\boldsymbol{r}_k = (x_k, y_k)$ and the orientation with respect to the positive x-axis ψ_k, according to (4.9) and (4.10). We numerically solve the resulting equations of motion for the 100 identical inclusions with parameters given by $b = \rho = \alpha_i^{(0)} = \alpha_i^{(2)} = 1$ for all $i = \{1, ..., 100\}$, $\varepsilon = 0.1$ and $L = 5$, whilst the initial x and y positions of the inclusions are a random number in the range $[-1, 1]$ and $[-L, L]$ respectively with a random initial orientation ψ in the range $[0, 2\pi]$. We plot a realization for times $t = \{0, 0.005, 0.05, 1, 10, 100\}$ in Fig. 5.2.

We observe from the initial configuration that the periodic boundaries results in a preferential alignment parallel to this boundary (note $t = 0.005$ and $t = 0.05$). This result is in contrast with Fig. 4.6 which simulated the interactions of inclusions on an infinite flat membrane. In that case, the membrane was isotropic therefore resulting in no preferential alignment of the inclusion. Given that the inclusions orient themselves parallel to the periodic boundary due to the effects of the inclusions' images, there is curvature mediated repulsion, resulting in the formation of a hexagonal configuration (note $t = 1$) which spreads out (note $t = 10$). For longer simulation times, the hexagonal configuration breaks apart resulting in linear aggregates (note $t = 100$) which repel each other, similar to the repulsion of the infinite lines studied in Section 4.2.3. Periodicity appears to be a viable mechanism by which membrane inclusion alignment occurs.

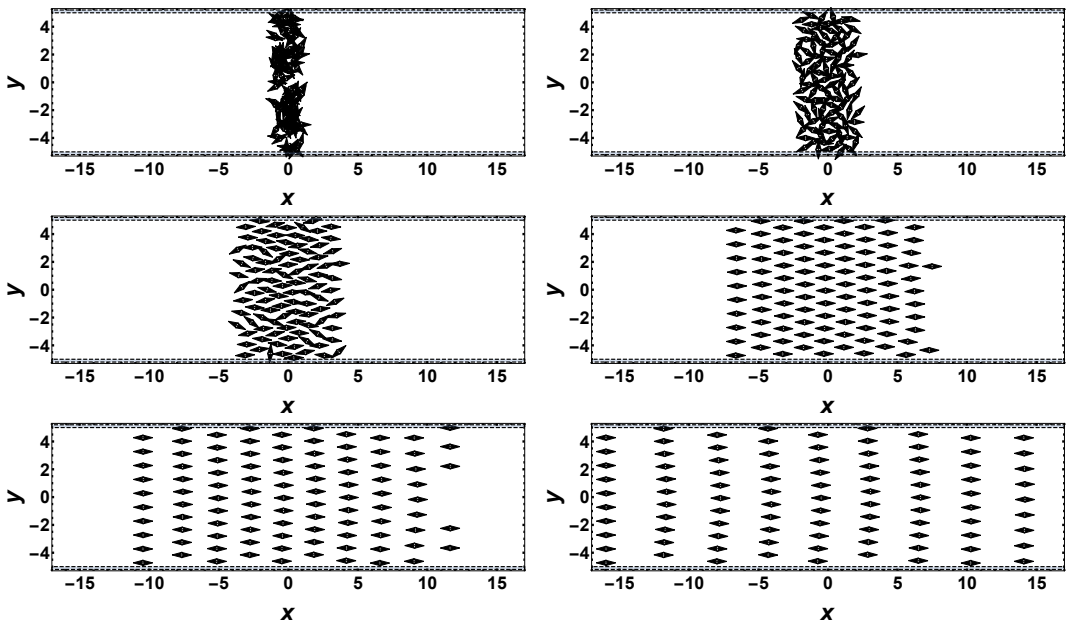

Figure 5.2: Simulation of 100 symmetry-breaking inclusions (shown as black double-headed arrows) by numerically solving (4.9) and (4.10) with the interaction energy (5.17) on a periodic domain in the y direction (the limits of which are denoted by the black dashed lines) with the parameters $b = \rho = \alpha_i^{(0)} = \alpha_i^{(2)} = 1$, for all $i = \{1, ..., 100\}$, $\varepsilon = 0.1$, and $L = 5$. The initial x and y positions of all inclusions are in the range $[-1, 1]$ and $[-L, L]$ respectively with a random initial orientation ψ in the range $[0, 2\pi]$. Times shown from left to right and top to bottom are $t = \{0, 0.005, 0.05, 1, 10, 100\}$.

5.6 Chapter summary

We investigated the result of periodic boundaries on the curvature-mediated interaction between rigid symmetry-breaking inclusions. Though the local shape around both inclusions was generally the same as the shapes found in Section 3.2.2, the periodicity resulted in an infinite sum of logarithmic contributions in the outer membrane shape; namely, from the deformations imposed on the membrane by the images of both real inclusions. We asymptotically matched the outer solution with the layer solutions of the inclusion and evaluated the sums to determine the total effective correction to the local shape. We found that, as a result of periodicity imposed on the membrane, this shape correction was no longer vanishing in the absence of a second inclusion; the single inclusion interacted with the deformations imposed by its own images. Determining the interaction energy, we found that the inclusion images imposed a curvature-mediated torque so that the preferred alignment of the real inclusion was such that its orientation was parallel to the periodic boundary. Furthermore, the magnitude of this torque increased with decreasing periodic domain length, as this corresponded to the inclusion images moving closer to the real inclusion, along with the magnitude of the isotropic and anisotropic contact angles imposed by the inclusion.

Given that the interaction energy was dominated by local contributions to the membrane shape, we extended the derived law to consider an arbitrary number of inclusions on a periodic domain and developed equations of motion. With this framework, we numerically simulated 100 inclusions confined to a periodic domain. We observed that the inclusions would preferentially align and, given that inclusions with orientations that are parallel to their separations result in curvature-mediated repulsion, the inclusions spread out along the membrane. To minimize the energy of the system the inclusions adopted a hexagonal configuration. For longer simulation times, the inclusions formed linear aggregates, similar to the infinite lines studied in Section 4.2.3, which repelled along the membrane.

The analytical and numerical results derived coincide with the observations of preferred protein orientation made in molecular dynamics simulation of cylindrical geometries. Therefore, periodicity appears to be a viable mechanism for protein alignment without the need for an underlying non-zero principal curvature.

Chapter 6

Conclusion

We reiterate the important results of chapters 2 to 5 of the dissertation before concluding with a discussion on future research directions in light of biologically inspired mechanically-mediated interactions on lipid bilayers. In particular, we highlight some of the geometric and mechanical properties of the lipid bilayer which have recently been shown to play non-trivial roles in the deformation of the membrane as well as in the self-assembling aggregation of embedded proteins.

6.1 Summary of thesis

6.1.1 Chapter 2

We began our investigation by considering the shaping of a filament in the plane under the effects of attaching curvature-inducing proteins which acted analogous to mechanical scaffolds. We took this model to be a proxy for the shaping of a membrane cross-section in a bath of such proteins, the latter of which were modeled as elastic filaments that were allowed to move by means of diffusion and drift for the purpose of minimizing the protein's individual bending energy. By using Kirchhoff rod formalism and thermodynamic arguments, we developed a system of equations which described the time-dependent shaping of the filament and the concentration distribution of attached proteins, which contrasted with previous work that only considered equilibrium configurations.

Our analysis focused primarily on constant curvature solutions of the filament and spatially uniform protein concentrations. We determined the curvature of the filament as a function of the protein concentration surrounding the filament, the equilibrium constant of the adhesion reaction, and the persistence length of the protein, being a measure of the protein's bending stiffness with respect to the temperature of the

system. For small protein persistence lengths, there was a single stable constant curvature solution, however, past a critical persistence length, stable high and low curvature solutions together with an unstable curvature existed in a bistable regime. Using weakly nonlinear analysis, we determined that, near the unstable constant curvature solution, the self-assembling protein adhesion equations reduced to a Cahn-Hilliard system. Under these circumstances, the curvature-inducing proteins would attach onto the filament forming regions of locally stable high and low curvatures which, due to a combination of protein movement and adhesion kinetics, would phase-coarsen to form a spatially uniform stable solution.

We extended the formalism used to derive the self-assembling filament equations to consider multiple species of proteins which could attach onto both sides of the filament. Due to the more complicated adhesion processes at play, the constant curvature equilibrium solutions could be found by solving a system of simultaneous equations. Furthermore, using linear stability analysis, we found that, for protein species which had similar chemical and diffusion characteristics, the local stabilities of these solutions were determined by adhesion competition between proteins attaching on opposing sides of the filament.

Despite acting as a first step to understanding the interplay between protein concentration and the underlying membrane geometry, we noted two criticisms of the self-assembling filament model: The absence of extensibility in the filament and global interactions between embedded proteins. Whilst the former could be modeled with an additional constitutive equation describing the evolution of the filament's tangent vector, we found that the filament model with free-ends boundary conditions was inadequate in describing the long-range interactions between proteins seen in experiment and simulation.

6.1.2 Chapter 3

Noting the inadequacies of the previously derived filament model, we investigated the self-assembly of proteins already embedded on a fluid membrane that arose as a result of indirect and long-range curvature-mediated interactions. We considered the deformation energy of an infinitesimally thin fluid membrane that was approximately flat and extended to infinity and determined its corresponding equilibrium shape equation. We then considered two rigid inclusions which were embedded in this membrane and the corresponding boundary conditions on the height of the membrane fluctuations, the normal derivative of the fluctuations with respect to the inclusion boundary, and the balance of vertical force and moments.

We then calculated the deformation energy of the fluid membrane due to two inclusions, which broke symmetry either in the contact angle that they imposed on the surrounding membrane or their boundary geometry, as a function of their separation and the orientation of their anisotropic deformations. In particular, we studied inclusions which were invariant under a rotation of π as this was the dominant symmetry-breaking mode in the interaction energy. We generically determined the local shapes around the inclusion and the shape of the membrane sufficiently far away from the two inclusions and, using asymptotic matching, we found the corrections in the inclusions' local shapes necessary to determine the curvature-mediated interaction energy. We found that the interaction laws for both instances of symmetry-breaking were equivalent and featured isotropic repulsion on the inverse quartic of the separation, consistent with previous theoretical work, and an orientation dependent term which could result in both curvature-mediated attraction or repulsion on the inverse separation squared.

We studied the interactions of two inclusions which were identical and found that attraction occurred when their separation was perpendicular to the orientation governing their anisotropy either in the contact angle or the inclusion's boundary geometry. In this case, the attraction that arose from symmetry-breaking balanced with the isotropic repulsion to give a natural equilibrium distance between the two inclusions. This curvature-mediated self-assembly between the inclusions was a consequence of minimizing the deformation energy of the fluid membrane.

6.1.3 Chapter 4

Given the previous result whereby symmetry-breaking inclusions would naturally self-assemble to a finite separation, we next studied the energy and stability of simple aggregate shapes and their associated collective properties. To do so, noting that the interaction energy was dominated by local contributions to the membrane shape, we extended the interaction law derived in Chapter 3 to model an arbitrary number of symmetry-breaking inclusions and derived a gradient flow model, given that the movement within the fluid membrane plane was a dissipative process, to simulate their corresponding movement under curvature-mediated forces and torques.

We first studied the properties of linear aggregates. We calculated the energy density of an infinite line and determined that the equilibrium separation was shorter than for the two inclusion case due to the additional curvature-mediated attraction from all inclusions within the aggregate. We numerically showed that the linear

aggregate was robust to perturbations in the positions and orientation of the inclusions which comprise it, given that the inclusions aligned and reformed the line. Inspired by numerical observations that curvature-inducing proteins form ring aggregates which repel on cylindrical membranes, we considered the interaction energy of two infinite linear aggregates which were not allowed to bend. We found that the two linear aggregates in close proximity would repel on the inverse quartic separation, similar to the case with two isotropic inclusions, however, the extent of the separation depended directly on the isotropic and anisotropic deformation exerted by the symmetry-breaking inclusion. Furthermore, the presence of the second linear aggregate increased the equilibrium separation between inclusions within in an aggregate due to curvature-mediated forces. Given the infinite length of the aggregates which prevented bending deformations, we numerically simulated two finite lines. We observed that the two linear aggregates would bend to attract inclusions within opposing aggregates, leading to a finite equilibrium separation between the two aggregates.

We next studied inclusions in polygonal formations. We found the energy density of a polygon comprised of an arbitrary number of symmetry-breaking inclusions and determined the equilibrium separation of the inclusion from the center as well as the polygon's side-length. We found that two types of polygons could form: For polygons with 3 or 4 inclusions, the inclusion orientations would point perpendicular to their separation from the polygon center, whilst for 6 or more inclusions, the orientation and this separation would be parallel. The symmetry-breaking inclusions would not form finite polygons with 5 inclusions. We furthermore found that the side length of the polygon reduced to the equilibrium separation of the infinite line for the number of inclusions within the aggregate approaching infinity. We then analytically determined the local stability of polygons featuring 3, 4, and 6 inclusions and found that only the triangle was stable. However, noting the previous results that the polygon reduced to the infinite line in the limit of a large number of inclusions and that the infinite line was robust to perturbations, we hypothesized that past a critical number of inclusions in the polygon, its local stability would switch from unstable to stable. We verified this claim by analyzing the spectrum of the Hessian and found that, provided there were 11 or more inclusions in the polygon, the aggregate was locally stable, regardless of the magnitude of symmetry-breaking effects imposed by the inclusion.

Given our previous results regarding the energies of lines and polygons, we determined the collective elastic properties of an aggregate, given that it was both flexible and extensible. We found that, under bending deformations, the aggregate behaved as

a strain-stiffening material, whilst under stretching deformations, the aggregate featured an asymmetry whereby it took infinite energy to compress it to zero separation, but only finite energy to stretch it to infinity.

We concluded our study of self-assembled aggregates under curvature-mediated interactions by numerically simulating 1000 inclusions which were initially randomly positioned and orientated. We observed that the inclusions would form a close-knit network of linear aggregates which would unzip to form larger linear aggregates and larger loops within the network.

6.1.4 Chapter 5

Inspired by the analysis on the repulsion of two infinite linear aggregates, which were motivated by the observation of proteins forming rings on cylindrical geometries, we investigated one of the mechanisms under which curvature-mediated protein alignment, necessary for the assembling of ring aggregates, could occur; namely, by periodicity in the membrane boundary.

We determined the interaction energy between two symmetry-breaking inclusions on an approximately flat membrane which was infinite along one direction, but periodic in the other orthogonal direction. To do so, we followed the formalism described in Chapter 3 by solving for shapes in the local region around the inclusions and the shape of the outer membrane. We noted that, due to the periodic boundary conditions, there would not only be contributions to the outer membrane shape from the real inclusions, but also from their corresponding infinite images. By asymptotic matching, we found that the local shape corrections necessary to determine the interaction energy depended on the deformation properties of both inclusions, whereas for the non-periodic case, they depended on the opposite inclusion. With the introduction of periodic boundary conditions, we found that a single inclusion would interact with its images by means of curvature-mediation; namely, by exerting a torque so that it aligns parallel to the periodic boundary. This alignment orients the inclusion so that it is in an attracting configuration with its images.

Noting again that the interaction energy was dominated by contributions from the local membrane around the inclusion, we extended the interaction law to consider an arbitrary number of inclusions on a periodic membrane and derived corresponding equations of motion. We solved the resulting system numerically for 100 inclusions and observed that periodicity resulted in the preferential alignment of the inclusions. However, given that this would cause curvature-mediated repulsion, the real inclusions formed hexagonal configurations to minimize the energy and continued to spread out.

For longer simulation times, the inclusions formed linear aggregates, analogous to the aggregates of infinite size considered in Chapter 4, which repelled, coinciding with the repulsion of protein rings on the cylindrical geometry. These results suggested that periodicity in the membrane was a viable mechanism for curvature-mediated protein alignment.

6.2 Future directions

We discuss some open questions in the self-assembly of proteins due to the geometric and mechanical properties of the underlying fluid membrane that warrant further investigation.

6.2.1 Underlying membrane geometry

In Chapter 5, we found that periodicity of the geometry was a viable mechanism by which protein alignment, observed on cylindrical geometries [89], occurs. However, curvature-inducing proteins from the BAR and ENTH families have been observed to be curvature-sensing [12, 72]; the underlying geometry of the lipid bilayer plays an important role in the arrangement and assembly of the proteins. A natural question arises: If the membrane was bent such that it had a single non-zero principal curvature, would an embedded protein exhibit preferred alignment with respect to this axis of curvature without the need for periodic boundary conditions?

A means of investigating the effect of membrane curvature would be to consider small undulations around an unperturbed radius, R. One could then follow the derivation, as per Section 3.1.1, to obtain a new equilibrium shape equation from the Helfrich Hamiltonian for radial fluctuations around a cylindrical membrane. In the limit of $R \to \infty$, the shape equation derived should reduce to the biharmonic equation seen for approximately flat geometries. The process to determine the corresponding interaction energy of a protein embedded on a cylindrical patch of membrane would be an extension of the formalism presented in Chapter 3; namely, deriving the boundary conditions of an inclusion embedded on a cylinder, determining the shapes in the local region of the inclusion and the outer membrane far away from the inclusion, and asymptotic matching between these two regions to obtain the corrections necessary to calculate the interaction energy from the functional describing the radial deformations to the unperturbed cylinder. We would expect that the final result would be similar to that found for the single inclusion on a periodic membrane (i.e. (5.15)); namely, that

there should only be a rotational effect on the inclusion as a result of the underlying membrane curvature, with the effect increasing for decreasing R.

6.2.2 Surface tension

In Chapter 3, we supposed that the only contribution to the deformation energy of the fluid membrane was from bending contributions. However, there are numerous other mechanical properties of the lipid bilayer which play a non-trivial role in deformation, such as the surface tension which penalizes local area dilation of the membrane. A tense membrane resists deformation, so one would expect that surface tension affects membrane remodeling and, by extension, the membrane-mediated interactions of embedded proteins. Biological work has shown that cells under tension exhibit decreased rate of endocytosis [17] and can further alter the arrangement of membrane-remodeling events [9, 46]. There has been recent molecular dynamics simulation which has shown that surface tension directly inhibits protein self-assembly. As a result, similar networks of linear aggregates, as seen in Fig. 4.6, have been observed to break apart [88].

One could model the effects of surface tension by including additional terms in the Helfrich Hamiltonian which penalize dilation of area elements in the fluid membrane. Two parameters would now govern the deformation of the fluid membrane: the bending stiffness and the resistance to local area dilation, which would be related to the surface tension of the membrane. By following the formalism described in Chapter 3, one would derive a new energy that depends on these two parameters, with the results of Chapter 3 obtained in the limit whereby bending deformations dominate the interaction energy between inclusions, and a new regime where surface tension would dominate.

6.2.3 Membrane thickness and lipid properties

In using the Helfrich Hamiltonian, the implicit assumption is made that the lipid bilayer is infinitesimally thin. However, the thickness of the membrane, which is related to the deformations of individual lipid molecules that comprise it, play non-trivial roles in its mechanical properties. Lipid molecules have different phases which describe whether their long molecular chains are ordered or disordered and, depending on the phase composition of the membrane, the deformation behavior of the lipid bilayer can substantially vary. As an example, recent computational work has shown that membranes which are homogeneously comprised of gel-phase lipids, whereby

the in-plane mobility is vanishingly small and can no longer be considered fluid, do not behave like Euler elastica and are therefore not accurately modeled by the quadratic Helfrich energy [26]. A further contribution to the deformation energy of the membrane has been shown to be the lipid tilt, or the angle that the individual lipid molecules make with the mid-plane of the bilayer [99, 100].

Recent work in elasticity has developed a new free energy for biomembranes which is dependent on its lipid phase composition and deformation under bending [23]. In the presented methodology, the membrane is treated as a quasi-two dimensional object, with constitutive assumptions imposed at the three-dimensional level, before a reduction of dimension under a quasi-compressibility assumption. The calculated energy functional features local and non-local contributions which model the interplay between the membrane shape, its chemical composition, and its associated thickness. The implications of this free energy include non-intuitive results, such as being able to describe the shape and the lipid order of the lipid bilayer by knowledge of the in-plane membrane stretching elasticity [24]. An avenue of investigation worth pursuing would be to derive an elasticity-consistent model for the interaction of membrane inclusions, either directly from the free energy derived in [23], or by following a similar derivation; namely, by supposing that the inclusions and the lipid bilayer are three-dimensional, imposing material properties, and then reducing the system to two dimensions. The result would be an interaction energy that would provide a theoretical framework under which the interplay between membrane curvature, surface tension, lipid composition and inclusion self-assembly could be studied.

Bibliography

[1] Himani Agrawal, Liping Liu, and Pradeep Sharma. Revisiting the curvature-mediated interactions between proteins in biological membranes. *Soft matter*, 12(43):8907–8918, 2016.

[2] S. S. Antman. *Nonlinear Problems of Elasticity*. Springer, New York, 2nd edition, 2005.

[3] H. Aranda-Espinoza, A. Berman, N. Dan, P. Pincus, and S. Safran. Interaction between inclusions embedded in membranes. *Biophysical journal*, 71(2):648–656, 1996.

[4] A. Arkhipov, Y. Yin, and K. Schulten. Four-scale description of membrane sculpting by BAR domains. *Biophysical Journal*, 95(6):2806–2821, September 2008.

[5] A. Arkhipov, Y. Yin, and K. Schulten. Membrane-bending mechanism of amphiphysin N-BAR domains. *Biophysical Journal*, 97(10):2727–2735, November 2009.

[6] G. S. Ayton, E. Lyman, and G. A. Voth. Hierarchical coarse-graining strategy for protein-membrane systems to access mesoscopic scales. *Faraday discussions*, 144:347–481, 2010.

[7] Thomas F. Banchoff and Stephen T. Lovett. *Differential geometry of curves and surfaces*. CRC Press, 2016.

[8] Lorenzo Botto, Eric P. Lewandowski, Marcello Cavallaro, and Kathleen J. Stebe. Capillary interactions between anisotropic particles. *Soft Matter*, 8(39):9957–9971, 2012.

[9] Steeve Boulant, Comert Kural, Jean-Christophe Zeeh, Florent Ubelmann, and Tomas Kirchhausen. Actin dynamics counteract membrane tension during clathrin-mediated endocytosis. *Nature cell biology*, 13(9):1124, 2011.

[10] Michael F. Brown. Soft matter in lipid–protein interactions. *Annual review of biophysics*, 46:379–410, 2017.

[11] F. Campelo, H. T. McMahon, and M. M. Kozlov. The hydrophobic insertion mechanism of membrane curvature generation by proteins. *Biophysical Journal*, 95(5):2325–2339, September 2008.

[12] B. R. Capraro, Y. Yoon, W. Cho, and T. Baumgart. Curvature sensing by the Epsin N-Terminal Homology domain measured on cylindrical lipid membrane tethers. *Journal of the American Chemical Society*, 132(4):1200–1201, February 2010.

[13] Marcello Cavallaro, Lorenzo Botto, Eric P. Lewandowski, Marisa Wang, and Kathleen J. Stebe. Curvature-driven capillary migration and assembly of rod-like particles. *Proceedings of the National Academy of Sciences*, 108(52):20923–20928, 2011.

[14] B. D. Coleman, E. H. Dill, M. Lembo, Z. Lu, and I. Tobias. On the dynamics of rods in the theory of Kirchhoff and Clebsch. *Archive for Rational Mechanics and Analysis*, 121(4):339–359, 1993.

[15] M. C. Cross and P. C. Hohenberg. Pattern formation outside of equilibrium. *Rev. Mod. Phys.*, 65:851–1112, July 1993.

[16] H. Cui, E. Lyman, and G. A. Voth. Mechanism of membrane curvature sensing by amphipathic helix containing proteins. *Biophysical Journal*, 100(5):1271–1279, March 2011.

[17] J. Dai and M. P. Sheetz. Regulation of endocytosis, exocytosis, and shape by membrane tension. In *Cold Spring Harbor symposia on quantitative biology*, volume 60, pages 567–571. Cold Spring Harbor Laboratory Press, 1995.

[18] N. Dan, P. Pincus, and S. A. Safran. Membrane-induced interactions between inclusions. *Langmuir*, 9(11):2768–2771, 1993.

[19] Gary B. Davies, Timm Krüger, Peter V. Coveney, Jens Harting, and Fernando Bresme. Assembling ellipsoidal particles at fluid interfaces using switchable dipolar capillary interactions. *Advanced materials*, 26(39):6715–6719, 2014.

[20] G. de Vaucouleurs. The case for a hierarchical cosmology. *Science*, 167(3922):1203–1213, February 1970.

[21] David S. Dean, V. Adrian Parsegian, and Rudolf Podgornika. Fluctuation mediated interactions due to rigidity mismatch and their effect on miscibility of lipid mixtures in multicomponent membranes. *Journal of Physics: Condensed Matter*, 27(21):214004, 2015.

[22] M. Dembo, D. C. Torney, K. Saxman, and D. Hammer. The reaction-limited kinetics of membrane-to-surface adhesion and detachment. *Proceedings of the Royal Society of London. Series B, Biological Sciences*, 234(1274):55–83, 1988.

[23] Luca Deseri, Mario D. Piccioni, and Giuseppe Zurlo. Derivation of a new free energy for biological membranes. *Continuum Mechanics and Thermodynamics*, 20(5):255, 2008.

[24] Luca Deseri and Giuseppe Zurlo. The stretching elasticity of biomembranes determines their line tension and bending rigidity. *Biomechanics and modeling in mechanobiology*, 12(6):1233–1242, 2013.

[25] M. Deserno. Fluid lipid membranes - a primer. 2007.

[26] Patrick Diggins IV, Zachary A. McDargh, and Markus Deserno. Curvature softening and negative compressibility of gel-phase lipid membranes. *Journal of the American Chemical Society*, 137(40):12752–12755, 2015.

[27] P. G. Dommersnes and J-B Fournier. Casimir and mean-field interactions between membrane inclusions subject to external torques. *EPL (Europhysics Letters)*, 46(2):256, 1999.

[28] P. G. Dommersnes and J-B Fournier. N-body study of anisotropic membrane inclusions: Membrane mediated interactions and ordered aggregation. *The European Physical Journal B-Condensed Matter and Complex Systems*, 12(1):9–12, 1999.

[29] Paul G. Dommersnes and Jean-Baptiste Fournier. The many-body problem for anisotropic membrane inclusions and the self-assembly of saddle defects into an egg carton. *Biophysical journal*, 83(6):2898–2905, 2002.

[30] A. R. Evans, M. S. Turner, and P. Sens. Interactions between proteins bound to biomembranes. *Physical Review E*, 67(4):041907, 2003.

[31] J. B. Fournier and P. G. Dommersnes. Comment on" long-range forces in heterogeneous fluid membranes. *EPL (Europhysics Letters)*, 39(6):681, 1997.

[32] Jean-Baptiste Fournier and Paolo Galatola. High-order power series expansion of the elastic interaction between conical membrane inclusions. *The European Physical Journal E*, 38(8):86, 2015.

[33] A. Frost, R. Perera, A. Roux, K. Spasov, O. Destaing, E. H. Egelman, P. De Camilli, and V. M. Unger. Structural basis of membrane invagination by F-BAR domains. *Cell*, 132(5):807–817, March 2008.

[34] A. Frost, V. M. Unger, and P. D. Camilli. The BAR domain superfamily: Membrane-molding macromolecules. *Cell*, 137(2):191–196, April 2009.

[35] J. Gerhart and M. Kirschner. *Cells, Embryos and Evolution.* Wiley-Blackwell, 1st edition, 1997.

[36] N. Ghoniem and D. Walgraef. *Instabilities and Self-Organization in Materials: Volume II: Applications in Materials Design and Nanotechnology.* Oxford University Press, 2008.

[37] F. Gittes, B. Mickey, J. Nettleton, and J. Howard. Flexural rigidity of microtubules and actin filaments measured from thermal fluctuations in shape. *The Journal of Cell Biology*, 120(4):923–934, February 1993.

[38] R. E. Goldstein and S. A. Langer. Nonlinear dynamics of stiff polymers. *Phys. Rev. Lett.*, 75(6):1094–1097, August 1995.

[39] Ramin Golestanian, Mark Goulian, and Mehran Kardar. Fluctuation-induced interactions between rods on a membrane. *Physical Review E*, 54(6):6725, 1996.

[40] Ramin Golestanian, Mark Goulian, and Mehran Kardar. Fluctuation-induced interactions between rods on membranes and interfaces. *EPL (Europhysics Letters)*, 33(3):241, 1996.

[41] M Goulian, R Bruinsma, and P Pincus. Long-range forces in heterogeneous fluid membranes. *EPL (Europhysics Letters)*, 22(2):145, 1993.

[42] Cameron L. Hall, Dominic Vella, and Alain Goriely. The mechanics of a chain or ring of spherical magnets. *SIAM Journal on Applied Mathematics*, 73(6):2029–2054, 2013.

[43] J. D. Halley and D. A. Winkler. Consistent concepts of self-organization and self-assembly. *Complexity*, 14(2):10–17, November 2008.

[44] M. C. Heinrich, B. R. Capraro, A. Tian, J. M. Isas, R. Langen, and T. Baumgart. Quantifying membrane curvature generation of Drosophila Amphiphysin N-BAR domains. *Journal of Physical Chemistry Letters*, 1:3401–3406, November 2010.

[45] W. Helfrich. Elastic properties of lipid bilayers: Theory and possible experiments. *Zeitschrift für Naturforschung, C: Journal of Biosciences*, 28(11-12):693–703, December 1973.

[46] Andrew R. Houk, Alexandra Jilkine, Cecile O. Mejean, Rostislav Boltyanskiy, Eric R. Dufresne, Sigurd B. Angenent, Steven J. Altschuler, Lani F. Wu, and Orion D. Weiner. Membrane tension maintains cell polarity by confining signals to the leading edge during neutrophil migration. *Cell*, 148(1-2):175–188, 2012.

[47] John David Jackson. *Classical electrodynamics*. AAPT, 1999.

[48] U. Jelerčič and N. S. Gov. Pearling instability of membrane tubes driven by curved proteins and actin polymerization. *Physical Biology*, 12(6):066022–, 2015.

[49] Ludger Johannes, Weria Pezeshkian, John H Ipsen, and Julian C Shillcock. Clustering on membranes: Fluctuations and more. *Trends in Cell Biology*, 2018.

[50] D. Kabaso, N. Bobrovska, W. Góźdź, N. Gov, V. Kralj-Iglič, P. Veranič, and A. Iglič. On the role of membrane anisotropy and BAR proteins in the stability of tubular membrane structures. *Journal of Biomechanics*, 45(2):231–238, January 2012.

[51] D. Kabaso, E. Gongadze, P. Elter, U. van Rienen, J. Gimsa, V. Kralj-Igliç, and A. Igliç. Attachment of rod-like (BAR) proteins and membrane shape. *Mini-Reviews in Medicinal Chemistry*, 11(4):272–282, 2011.

[52] A. Y. Kasumov, D. V. Klinov, P. E. Roche, S. Guéron, and H. Bouchiat. Thickness and low-temperature conductivity of DNA molecules. *Applied Physics Letters*, 84(6):1007–1009, 2004.

[53] J. B. Keller and S. I. Rubinow. Slender-body theory for slow viscous flow. *Journal of Fluid Mechanics*, 75:705–714, June 1976.

[54] Bahareh Kiani, Damien Faivre, and Stefan Klumpp. Elastic properties of magnetosome chains. *New Journal of Physics*, 17(4):043007, 2015.

[55] Don Koks. *Explorations in mathematical physics: the concepts behind an elegant language*. Springer Science & Business Media, 2006.

[56] Goce Koleski and Jean-Baptiste Fournier. Linear response approximation in effective field theory for the calculation of elastically mediated interactions in one dimension. *Physical Review E*, 93(5):052128, 2016.

[57] James Kwiecinski, S. Jonathan Chapman, and Alain Goriely. Self-assembly of a filament by curvature-inducing proteins. *Physica D: Nonlinear Phenomena*, 344:68–80, 2017.

[58] James A. Kwiecinski, S. Jon Chapman, and Alain Goriely. Symmetry-breaking membrane inclusions - part i: Curvature-mediated interactions on flat geometries. *Soft Matter preprint*, 2018.

[59] H. Lehle, E. Noruzifar, and M. Oettel. Ellipsoidal particles at fluid interfaces. *The European Physical Journal E*, 26(1-2):151–160, 2008.

[60] Eric P. Lewandowski, Marcello Cavallaro Jr, Lorenzo Botto, Jorge C. Bernate, Valeria Garbin, and Kathleen J Stebe. Orientation and self-assembly of cylindrical particles by anisotropic capillary interactions. *Langmuir*, 26(19):15142–15154, 2010.

[61] Hsiang-Ku Lin, Roya Zandi, Umar Mohideen, and Leonid P Pryadko. Fluctuation-induced forces between inclusions in a fluid membrane under tension. *Physical review letters*, 107(22):228104, 2011.

[62] R. Lipowsky. The conformation of membranes. *Nature*, 349:475–481, February 1991.

[63] Jean-Christophe Loudet and Bernard Pouligny. Self-assembled capillary arrows. *EPL (Europhysics Letters)*, 85(2):28003, 2009.

[64] Jean-Christophe Loudet, Arjun G Yodh, and Bernard Pouligny. Wetting and contact lines of micrometer-sized ellipsoids. *Physical review letters*, 97(1):018304, 2006.

[65] J. L. McWhirter, G. Ayton, and G. A. Voth. Coupling field theory with mesoscopic dynamical simulations of multicomponent lipid bilayers. *Biophysical Journal*, 87(5):3242–3263, November 2004.

[66] C. Mim, H. Cui, J. A. Gawronski-Salerno, A. Frost, E. Lyman, G. A. Voth, and V. M. Unger. Structural basis of membrane bending by the N-BAR protein endophilin. *Cell*, 149(1):137–145, March 2012.

[67] S. Morlot and A. Roux. Mechanics of dynamin-mediated membrane fission. *Annu. Rev. Biophys.*, 42(1):629–649, May 2013.

[68] D. E. Moulton, T. Lessinnes, and A. Goriely. Morphoelastic rods. Part I: A single growing elastic rod. *Journal of the Mechanics and Physics of Solids*, 61(2):398–427, February 2013.

[69] Hiroshi Noguchi and Jean-Baptiste Fournier. Membrane structure formation induced by two types of banana-shaped proteins. *Soft matter*, 13(22):4099–4111, 2017.

[70] Jeong-Man Park and TC Lubensky. Interactions between membrane inclusions on fluctuating membranes. *Journal de Physique I*, 6(9):1217–1235, 1996.

[71] B. Peleg, A. Disanza, G. Scita, and N. Gov. Propagating cell-membrane waves driven by curved activators of actin polymerization. *PLoS One*, 6(4):1–11, April 2011.

[72] B. J. Peter, H. M. Kent, I. G. Mills, Y. Vallis, P. J. G. Butler, P. R. Evans, and H. T. McMahon. BAR domains as sensors of membrane curvature: The amphiphysin BAR structure. *Science*, 303(5657):495–499, January 2004.

[73] Eugene P. Petrov and Petra Schwille. Translational diffusion in lipid membranes beyond the saffman-delbrück approximation. *Biophysical journal*, 94(5):L41–L43, 2008.

[74] W. A. Prinz and J. E. Hinshaw. Membrane-bending proteins. *Critical reviews in biochemistry and molecular biology*, 44(5):278–291, 2009.

[75] W. Rawicz, K. C. Olbrich, T. McIntosh, D. Needham, and E. Evans. Effect of chain length and unsaturation on elasticity of lipid bilayers. *Biophysical Journal*, 79(1):328–339, July 2000.

[76] Benedict J. Reynwar and Markus Deserno. Membrane-mediated interactions between circular particles in the strongly curved regime. *Soft Matter*, 7(18):8567–8575, 2011.

[77] P. W. K. Rothemund. Folding DNA to create nanoscale shapes and patterns. *Nature*, 440:297–302, March 2006.

[78] P. G. Saffman and M. Delbrück. Brownian motion in biological membranes. *Proceedings of the National Academy of Sciences*, 72(8):3111–3113, 1975.

[79] Kayla Sapp and Lutz Maibaum. Suppressing membrane height fluctuations leads to a membrane-mediated interaction among proteins. *Physical Review E*, 94(5):052414, 2016.

[80] Johannes Schönke and Eliot Fried. Stability of vertical magnetic chains. *Proc. R. Soc. A*, 473(2198):20160703, 2017.

[81] A. B. Sendova-Franks and N. R. Franks. Self-assembly, self-organization and division of labour. *Philosophical Transactions of the Royal Society of London B*, 354(1388):1395–1405, August 1999.

[82] Z. Shi and T. Baumgart. Dynamics and instabilities of lipid bilayer membrane shapes. *Advances in Colloid and Interface Science*, 208:76–88, June 2014.

[83] Y. Shibata, J. Hu, M. M. Kozlov, and T. A. Rapoport. Mechanisms shaping the membranes of cellular organelles. *Annual Review of Cell and Developmental Biology*, 25:329–354, November 2009.

[84] M. Simunovic and P. Bassereau. Reshaping biological membranes in endocytosis: crossing the configurational space of membrane-protein interactions. *Biological Chemistry.*, 395(3):275–283, March 2014.

[85] M. Simunovic, C. Mim, T. C. Marlovits, G. Resch, V. M. Unger, and G. A. Voth. Protein-mediated transformation of lipid vesicles into tubular networks. *Biophysical Journal*, 105(3):711–719, August 2013.

[86] M. Simunovic, A. Srivastava, and G. A. Voth. Linear aggregation of proteins on the membrane as a prelude to membrane remodeling. *Proceedings of the National Academy of Sciences*, 110(51):20396–20401, December 2013.

[87] Mijo Simunovic, Anđela Šarić, J Michael Henderson, Ka Yee C. Lee, and Gregory A Voth. Long-range organization of membrane-curving proteins. *ACS central science*, 3(12):1246–1253, 2017.

[88] Mijo Simunovic and Gregory A. Voth. Membrane tension controls the assembly of curvature-generating proteins. *Nature Communications*, 6:7219, May 2015.

[89] Mijo Simunovic, Gregory A Voth, Andrew Callan-Jones, and Patricia Bassereau. When physics takes over: Bar proteins and membrane curvature. *Trends in cell biology*, 25(12):780–792, 2015.

[90] B. Sorre, A. Callan-Jones, J. Manzi, B. Goud, J. Prost, P. Bassereau, and A. Roux. Nature of curvature coupling of amphiphysin with membranes depends on its bound density. *Proceedings of the National academy of Sciences of the United States of America*, 109(1):173–178, January 2012.

[91] A. Srivastava and G. A. Voth. Hybrid approach for highly coarse-grained lipid bilayer models. *J. Chem. Theory Comput.*, 9(1):750–765, January 2013.

[92] Dimitris Stamou, Claus Duschl, and Diethelm Johannsmann. Long-range attraction between colloidal spheres at the air-water interface: The consequence of an irregular meniscus. *Physical Review E*, 62(4):5263, 2000.

[93] S. Suetsugu, S. Kurisu, and T. Takenawa. Dynamic shaping of cellular membranes by phospholipids and membrane-deforming proteins. *Physiological Reviews*, 94(4):1219–1248, October 2014.

[94] Stephen P. Timoshenko and Sergius Woinowsky-Krieger. *Theory of plates and shells*. McGraw-hill, 1959.

[95] M. J. Tindall, P. K. Maini, S. L. Porter, and J. P. Armitage. Overview of mathematical approaches used to model bacterial chemotaxis II: Bacterial populations. *Bulletin of Mathematical Biology*, 70(6):1570–1607, 2008.

[96] Casper Van Der Wel, Afshin Vahid, Anđela Šarić, Timon Idema, Doris Heinrich, and Daniela J Kraft. Lipid membrane-mediated attraction between curvature inducing objects. *Scientific reports*, 6:32825, 2016.

[97] D. Vella and L. Mahadevan. The cheerios effect. *American Journal of Physics*, 73(9):817–825, 2005.

[98] Dominic Vella, Emmanuel du Pontavice, Cameron L Hall, and Alain Goriely. The magneto-elastica: from self-buckling to self-assembly. *Proc. R. Soc. A*, 470(2162):20130609, 2014.

[99] Xin Wang and Markus Deserno. Determining the pivotal plane of fluid lipid membranes in simulations. *The Journal of chemical physics*, 143(16):164109, 2015.

[100] Xin Wang and Markus Deserno. Determining the lipid tilt modulus by simulating membrane buckles. *The Journal of Physical Chemistry B*, 120(26):6061–6073, 2016.

[101] T. R. Weikl, M. M. Kozlov, and W. Helfrich. Interaction of conical membrane inclusions: Effect of lateral tension. *Physical Review E*, 57(6):6988, 1998.

[102] K. Weiß, A. Neef, Q. Van, S. Kramer, I. Gregor, and J. Enderlein. Quantifying the diffusion of membrane proteins and peptides in black lipid membranes with 2-focus fluorescence correlation spectroscopy. *Biophysical Journal*, 105(2):455–462, July 2013.

[103] Y. Yin, A. Arkhipov, and K. Schulten. Simulations of membrane tubulation by lattices of amphiphysin N-BAR domains. *Structure*, 17(6):882–892, June 2009.

[104] Cem Yolcu and Markus Deserno. Membrane-mediated interactions between rigid inclusions: an effective field theory. *Physical Review E*, 86(3):031906, 2012.

[105] Cem Yolcu, Robert C Haussman, and Markus Deserno. The effective field theory approach towards membrane-mediated interactions between particles. *Advances in colloid and interface science*, 208:89–109, 2014.

[106] Zhenkun Zhang, Patrick Pfleiderer, Andrew B Schofield, Christian Clasen, and Jan Vermant. Synthesis and directed self-assembly of patterned anisometric polymeric particles. *Journal of the American Chemical Society*, 133(3):392–395, 2010.

[107] Q. Zheng and G. W. Wei. Poisson-Boltzmann-Nernst-Planck model. *The Journal of Chemical Physics*, 134(19):194101–, March 2011.

[108] J. Zimmerberg and M. M. Kozlov. How proteins produce cellular membrane curvature. *Nature Reviews. Molecular Cell Biology*, 7(1):9–19, January 2006.